A Convectively-Coupled Framework for Understanding Hurricane Azimuthal Asymmetries and Secondary Eyewall Formation

Thesis advisor: Professor Zhiming Kuang Jiahua Guo

A Convectively-Coupled Framework for Understanding Hurricane Azimuthal Asymmetries and Secondary Eyewall Formation

Abstract

Tropical cyclones (TCs) or hurricanes are among the most devastating natural disasters. Improvement of intensity forecasts of hurricanes is not yet satisfactory. Among all the factors that can influence the intensity of a hurricane, the structure is crucial for accurate intensity and track forecasts. Important structural features include asymmetric features such as spiral rainbands and axisymmetric features such as secondary eyewall formation. Throughout this dissertation, we are going to investigate the potential mechanisms associated with these features from a convectively coupled perspective.

In Chapter 2, we applied space-time spectral analysis to study the asymmetric perturbations in a hurricane and found two distinct power peaks in most of the variables. We obtained the structure of each mode by regressing each field onto a window-filtered index. We found that the structure of the fast-propagating wave is similar to that of the unstable mixed vortex-Rossby-inertia-gravity wave. The slow-propagating wave has a retrograde intrinsic propagating speed and a vertical structure that resembles that of convectively coupled waves.

Inspired by the findings from Chapter 2, we then developed a convectively coupled eigenfrequency model to investigate the linear instability of TC-like vortices in Chapter 3. We confirmed that

the instability of the mixed vortex-Rossby-inertia-gravity wave is consistent with the fast-propagating signal observed in the WRF simulations. With convectively coupled dynamics, a branch of the nearly stationary wave becomes unstable.

To more accurately constrain the convective parameterization used in Chapter 3, we adopted the methodology developed by Kuang [2018] in Chapter 4. We first constructed several sets of linear response functions along the radius of the hurricane. We then derived the parameters in the convective parameterization from these linear response functions through model order reductions. The framework helps to estimate the parameters with more quantitative accuracy.

In Chapter 5, we introduced an axisymmetric framework that can potentially be applied to study the mechanisms behind secondary eyewall formation (SEF). The axisymmetric framework consists of a dry axisymmetric dynamic model that simulates hurricane-scale circulation and a cloud-resolving model that resolves local convection. Potentially, this framework allows more flexibility to investigate various hypotheses of SEF.

Contents

In Memory of Katherine Martin Widmer.

Acknowledgments

This work would not have been possible without the endless love, support, and kindness of many people.

I would like to express my deep gratitude to Professor Zhiming Kuang, my research advisor and mentor, for his continuous support of my study and research throughout the past several years. His patient guidance and insightful advice have been guiding me through and always keeping me motivated. His enthusiasm for science and encouraging attitude will continue to lead my way and help me to become a better one. My grateful thanks are also extended to my committee members, Professor Marianna Linz, Professor Brian Farrell and Professor Eli Tziperman for taking their precious time to discuss my research with me and providing valuable comments for writing the thesis.

I would like to thank Dr. Ji Nie, Dr. Giuseppe Torri, Dr. Lei Wang, Dr. Ding Ma, Dr. Yang Tian and Dr. Mary Moore for their enormous support and encouragement, and for sharing their valuable experience about research and teaching. I would also like to extend my thanks to my fellow graduate students, Marena Lin, Leah Birch, Jessica Kunke, Wangying Kang, Packard Chan, Duo Chan, David Wei, Xiaoting Yang, Minmin Fu, Ned Kleiner, Zeyuan Hu and Nathanael Wong for the friendship and their unconditional support.

I am also deeply grateful to Milena Perez, Sarah Colgan, Maryorie Grande and Aimee Smith for their wholehearted support. My life as a student, researcher and person here could not have been

easier with them.

My appreciation also goes to my friends in the Boston area, Jing Wang, Zheng Li, Zhicheng Yang, Feng Long, Xinmei Niu, Yinan Wang, Quntao Zhuang, Yichen Zhang and Chao Lang, who made my life here a beautiful and unforgettable experience.

I would like to express my very great appreciation to Katherine Martin Widmer and the painting school she created more than 40 years ago. The painting school has been a great relief during my leisure time. I am particularly grateful to become part of the community. I would like to extend my special thanks to all the beautiful minds I met at the painting school, Amy Ward, Rob Parker, Stephanie Campbell, Sarah Weddle, Rebecca Carpenter, Natasha Erdman, Charles Marchany and Caitlin Cooper.

Finally, nobody has been more important to me in the pursuit of this doctorate than the members of my family. My parents have always been loving me through their endless support and encouragement. I would like to extend my grateful thanks to my grandparents, my aunt, my cousin, and my nephew and niece, for always standing by me and be my source of strength since birth. My special thanks should be given to my loving and supportive Husband, Chuteng Zhou. Thank you for loving me no matter what.

1

Introduction

1.1 Motivation

Tropical cyclones (TCs), also known as hurricanes in North America or typhoons in East Asia, are among the most devastating natural disasters. In the US, tropical cyclones are responsible for the highest number of deaths (6,507) since 1980. They have caused the most significant economic losses ($954.4 billion, CPI-adjusted) over the past 40 years, and they also have the highest average cost per

event ($22.1 billion) among all weather and climate disasters [NOAA, 2019]. In terms of a single event, both the most lethal and the most expansive natural disasters in US history were tropical cyclones: The Galveston Hurricane of 1900 killed about 6000 to 8000 people, and Hurricane Katrina of 2005 caused more than $150 billion in damage [Emanuel, 2003]. Globally, tropical cyclones, together with other storms, cost more than 59% of total reported climate-related losses and ranked the second most fatal natural disasters (following earthquakes) over 1998-2017, with tropical cyclones being a major contributor [CRED et al., 2018]. With a warming climate, climate models project some increases in the intensities of tropical cyclones and their rainfall rates, increased frequency of intense tropical cyclones, increased storm surge risk with sea-level rise, and exacerbated disaster risk [Knutson et al., 2010, Walsh et al., 2016, Emanuel, 2005, Webster et al., 2005, Peduzzi et al., 2012]. Therefore, it becomes increasingly important to have more accurate forecasts and a better understanding of tropical cyclones to mitigate the damage.

With the implementation of advanced statistical prediction models and operational hurricane models (such as the GFDL model [Bender et al., 1993]), we have seen statistically significant improvement in the intensity and track forecasts of hurricanes since mid-1980s [McAdie & Lawrence, 2000, DeMaria et al., 2007]. However, compared to the track forecasts, the improvement of the intensity forecasts was almost an order of magnitude slower over 1985 - 2005. The improvement rates of the best available guidance have only been about one-third to one-half those of the track model improvements over the last 24 years [DeMaria et al., 2014]. The reason why the intensity forecasts are less skillful than the track forecasts is that a much more extensive range of processes are involved and must be accurately modeled to be able to predict the intensity accurately. Such processes include

the large-scale environment, the air-sea interaction, convection, microphysical processes, and many others.

Among all the factors that can influence the intensity and track of a hurricane, understanding the structure of a hurricane is crucial for accurate intensity and track forecasts [Wang & Wu, 2004]. Significant structural features include both asymmetric features, such as deformation of eyewalls and spiral rainbands, and symmetric features, such as concentric eyewalls. Studies [Schubert et al., 1999, Kossin & Schubert, 2001, Hendricks et al., 2009, Hendricks & Schubert, 2010, Naylor & Schecter, 2014] have shown that the deformation of eyewalls, such as elliptical or polygonal eyewalls can influence the structure and intensity of a hurricane through vorticity rearrangement. These studies suggest that a hurricane-like vortex ring usually undergoes inner-core vorticity mixing and mesovortices merging processes that lead to a decrease in center pressure and maximum tangential wind. With the contribution of convection near the eyewall, Naylor & Schecter [2014] found that the vorticity ring can be supported by the convection, and the maximum azimuthal wind tends to recover to its original magnitude. Nolan et al. [2001] have also shown that the wavenumber-one instability of the eyewall is associated with a displacement of the vortex center and thus leads to the persistent, small-amplitude trochoidal wobble often observed in hurricane tracks. Outside the eyewalls, spiral rainbands are another organized asymmetric feature, which is associated with intense precipitation and also has an impact on the size and intensity of a hurricane through both dynamic and thermodynamic processes [Montgomery & Kallenbach, 1997, Wang, 2009]. Montgomery & Kallenbach [1997] proposed that the vortex-Rossby wave traveling radially outwards would intensify the mean tangential winds outside the wave-excitation region. From the perspective of hydrostatic adjustment,

Wang [2009] showed that enhanced convective cooling (or weakened convective heating) in the outer spiral rainbands maintains both the intensity of a tropical cyclone and its inner-core compactness. In contrast, the opposite tends to weaken the intensity and to increase the size of a tropical cyclone.

The most remarkable symmetric feature related to hurricane intensities is concentric (or secondary) eyewall formations and eyewall replacement cycles [Willoughby et al., 1982]. The secondary eyewall usually forms from organized convection at several times the radius of the primary eyewall and coincides with a secondary tangential wind maximum. As the secondary eyewall contracts and amplifies, the inner eyewall weakens and is eventually replaced by the outer eyewall. The eyewall replacement cycle is often associated with a temporary weakening and then an intensification of the hurricane, and followed by an increase in the area covered by strong winds and consequent damages [Sitkowski et al., 2011]. Therefore it is believed to be responsible for large fluctuations in hurricane intensity [Houze et al., 2007]. On the other hand, observations in Western North Pacific [Kuo et al., 2009] suggest that the concentric eyewall formation appears to help maintain a high intensity of a hurricane for a longer duration, rather than rapidly varying the intensity of a hurricane.

1.2 Classification of asymmetries in tropical cyclones

Asymmetries of hurricanes can be roughly classified into deformations of the eyewall and different types of spiral rainbands, depending on the distance of the asymmetries from the center of the hurricanes. Deformations of the eyewall, such as elliptical or polygonal eyewalls or mesovortices, are

viewed as vortex-Rossby waves [Kuo et al., 1999, Reasor et al., 2000] and are considered to be a result of barotropic instability [Schubert et al., 1999], as they occur in the inner core region where the background vorticity is strong, and its radial-gradient reverses the sign.

Spiral rainbands are a broad concept of convection organized in a banded spiral structure and can be classified by its rotating speed or location. Based on their motions, there are stationary bands and moving bands. According to their relative distance from the center of a tropical cyclone, spiral rainbands are usually classified as inner and distant rainbands. Rainbands that are immediately outside the eyewall are identified as inner rainbands, whereas rainbands that are far from the vortex are considered distant rainbands. Different types of spiral rainbands may be considered as different types of waves and could be associated with different instability mechanisms [Houze, 2010].

Principal rainbands, which are a type of inner rainband, tend to be stationary relative to the storm center. They usually have a strong azimuthal wavenumber-1 signature. At the upwind end of the inner rainband, the clouds and precipitation tend to be less affected by the inner-core vortex and more convectively driven. In contrast, at its downwind end where it is attached to or in the vicinity of the eyewall, the principal rainband is more stratiform [Barnes et al., 1983, Powell, 1990a,b, Hence & Houze Jr, 2008]. The formation mechanism associated with the principal rainband has not been firmly established.

Another type of inner rainband is called secondary rainbands, which are transient and smaller in size than the principal rainbands. They are often located in the inner-core region, radially inside principal rainbands. They propagate rapidly in both radial and azimuthal directions, but slightly slower relative to the background tangential wind. Montgomery & Kallenbach [1997] suggested

that these bands are packets of vortex Rossby waves, whose dispersion is similar to planetary Rossby waves, with the planetary beta parameter generalized to the radial gradient of azimuthally mean vorticity. In a full physics hurricane simulation, Chen & Yau [2001] showed that the cloud bands are strongly coupled with potential vorticity bands, whose propagation properties are consistent with predictions of vortex Rossby wave theory.

Distant (or outer) rainbands are located far enough from the inner vortex that they are less affected by the dynamics of the vortex. Bogner et al. [2000] found that distant rainbands mainly occur at the radius where CAPE is significant; therefore distant rainbands are thought to be more convectively driven than the inner rainbands. As a result, strong updrafts and downdrafts are a notable feature in outer rainbands.

One of the questions that remains unclear is what mechanisms lead to the formation of the organized, banded and spiral structure of rainbands. Previous studies [Reasor et al., 2000, Wang, 2001, Chen & Yau, 2001, Wang, 2002, Corbosiero et al., 2006] have investigated the characteristics of spiral rainbands from either observations or full physics simulations and tried to associate them with various wave dynamics, such as vortex-Rossby waves or gravity waves. However, a systematic approach of identifying the wave features of spiral rainbands and investigate their instability mechanisms is still lacking. Therefore, in Chapter 2, we are going to dive into the frequency and wavenumber space and classify the asymmetries based on their dominant dispersion relations. Once different types of asymmetries are identified, we will continue to study their instability mechanisms in Chapter 3 and Chapter 4, mainly from a convectively coupled perspective.

1.3 Current understanding of asymmetries in TCs and their limitations

Spiral rainbands are generally viewed as either inertia-gravity waves [Abdullah, 1966, Kurihara, 1976, Willoughby, 1978, Diercks & Anthes, 1976, Willoughby et al., 1984] or vortex-Rossby waves [Macdonald, 1968, Guinn & Schubert, 1993, Montgomery & Kallenbach, 1997, Reasor et al., 2000, Chen & Yau, 2001, Wang, 2002, Corbosiero et al., 2006]. Since these two types of waves are both marginally stable by themselves, they require either some sort of instability mechanisms or external forcing to sustain. Such instability mechanisms include the barotropic instability [Montgomery & Shapiro, 1995] and the mixed vortex-Rossby-inertia-gravity wave instability [Ford, 1994a, Schecter & Montgomery, 2004, Menelaou et al., 2016], both of which have been extensively studied, especially within the dry dynamics framework.

However, the story will not be complete without taking convection into account. Many studies [Chen & Yau, 2001, Wang, 2002] have suggested that vortex-Rossby waves and the convective asymmetries are a highly coupled system, yet the convectively coupled aspect of wave dynamics and instability mechanisms in tropical cyclones are not extensively explored. Convection is essential in tropical cyclones because it not only affects the cyclone-scale circulation through diabatic forcing but itself is also modified by the cyclone-scale circulation through large-scale convergence or moisture advection. Therefore, it is crucial to incorporate the feedback of convection with the dry dynamics of the tropical cyclones.

Diercks & Anthes [1976] first attempted to include the effect of convection. They incorporated a one-layer parameterized convective heating with a two-layer linearized dynamic model to study

the instability of barotropic vortices, and they found that internal inertia-gravity waves are the only possible unstable modes in the system when unstable static stability is applied.

On top of the mixed vortex-Rossby-inertia-gravity wave instability, efforts have been made to include the effect of convection. Schecter & Montgomery [2007] studied the effect of non-precipitating clouds on such linear instability in TC-like vortices, and they found that the locally reduced stratification due to convection weakened the barotropic instability near the eyewall. Due to enhanced critical layer damping, it also damped the discrete vortex Rossby waves that would have grown by radiating spiral inertia-gravity waves.

Lahaye & Zeitlin [2016] studied the saturation of instabilities of TC-like vortices using a non-linear, shallow-water model, including the effects of moist convection. In their convective parameterization, they assumed precipitation to be proportional to convergence, whereas the surface evaporation is proportional to the magnitude of velocity. Compared to the dry simulations, they confirmed that the moist simulations exhibit a net increase of winds, even at the radius of maximum wind. In terms of the azimuthally asymmetric component, they found that the amplitude of inertia-gravity wave emission is substantially higher and lasts for a much longer time compared to the dry case and the simulation without evaporation, due to a strong convergence zone outside of the vortex.

The studies that incorporated the effect of convection showed some encouraging results, but convection can have a much more complicated effect on the dynamics than simply reducing the stratification. Therefore, in Chapter 3, we are going to investigate the effect of convection on the linear instability of TC-like vortices and its potential connections to spiral rainbands, with a more

sophisticated convective parameterization.

1.4 Current understanding of secondary eyewall formation and their limitations

Over the years, many hypotheses on SEF have been proposed, and they can roughly be grouped into two categories based on their mechanisms: the dynamic adjustment to latent heating outside the primary eyewall [Shapiro & Willoughby, 1982, Schubert & Hack, 1982, Hack & Schubert, 1986, Moon & Nolan, 2010, Rozoff et al., 2012], and the unbalanced boundary layer dynamics [Smith et al., 2009, Huang et al., 2012, Kepert, 2013, Abarca & Montgomery, 2013]. The hypothesis based on dynamic adjustment mechanism suggests that the latent heating outside the primary eyewall is a precursor to SEF and whether SEF can successfully emerge depends on the strength of the latent heating and the efficiency of latent heating warming the troposphere and enhancing the local tangential wind [Rozoff et al., 2012, Zhu & Zhu, 2014]. On the other hand, several studies [Smith et al., 2009, Huang et al., 2012, Kepert, 2013] argue that the unbalanced boundary layer is essential in initiating or assisting the SEF and the eyewall replacement cycle, through the supergradient tangential wind, the over-shooting radial inflow, and a resulting convergence region in the boundary layer.

Numerical experiments have been designed to test the relative importance of the dynamical adjustment and the unbalanced boundary layer processes. Rozoff et al. [2012] found that the response to diabatic forcing dominates the response to frictional forcing, and Menelaou et al. [2014] argued that the secondary wind maxima could be generated even without boundary layer physics. However,

a convincing mechanism of SEF is still lacking, and there are limitations in both of the arguments. The studies that focused on the dynamical adjustment to convective heating did not take into account how the convective heating responded to the dynamics. In contrast, the studies that argued the importance of boundary layer dynamics assumed a fixed free-troposphere vortex structure and did not allow the vortex to evolve. One caveat of using a comprehensive full-physics model is that all the processes are entangled with each other, and it is not easy to depict a clear conclusion of the causality. Therefore, we attempt to build a simple framework that will allow us to have better control of the feedback processes, and we will introduce this framework and some simple experiments in Chapter 5.

1.5 Outline of the thesis

In this dissertation, the focus will primarily be on understanding the formations of spiral rainbands and secondary eyewall. In Chapter 2, we will introduce the dominant asymmetric modes that we identify from an ensemble of WRF simulations and classify them to different types of waves based on their dispersion relations. We will mainly focus on the convective perspective of these modes, In Chapter 3, we will further investigate the effect of convection on the unstable mixed vortex-Rossby-inertia-gravity waves, and to see whether convection can trigger other types of instability. We incorporate a two-baroclinic-mode convective parameterization with a linearized dynamic model to account for the effect of convection. To refine the parameters in the convective parameterization, we will build linear response matrices and derive a reduced-order model from the matrices in Chapter 4.

In Chapter 5, we will focus more on SEF and introduce a novel framework that couples an axisymmetric hurricane-scale dynamics model and a cloud-resolving model. This framework can help us have better control of the feedback processes and potentially a better understanding of the feedback mechanisms. We will discuss several experiments with this new framework to demonstrate the application of this model. Finally, we will conclude this thesis work with key findings and future research directions in Chapter 6.

2

Spatial and temporal characteristics of asymmetries in tropical cyclones

2.1 Introduction

To the zeroth order, a hurricane can be idealized as an azimuthally symmetric vortex in gradient wind balance above the boundary layer. On top of this azimuthally-symmetric background vor-

tex, there could be smaller amplitude perturbations, due to synoptic-scale forcing, turbulence and convection. Some of these perturbations are organized at a scale that is large enough to influence the hurricane scale dynamics. Examples include elliptical or polygonal eyewalls [Kuo et al., 1999, Schubert et al., 1999, Reasor et al., 2000], which have an influence on the track [Nolan et al., 2001], structure, and intensity [Schubert et al., 1999, Kossin & Schubert, 2001, Hendricks et al., 2009, Hendricks & Schubert, 2010, Naylor & Schecter, 2014] of a hurricane, and spiral rainbands, which are associated with intense precipitation and may also have an impact on a hurricane's size and intensity [Montgomery & Kallenbach, 1997, Wang, 2009]. Therefore, it is of importance to better understand these organized asymmetries. Although this study will not directly tackle the problem of how asymmetries modulate the intensity or track of a hurricane, the results from this study can provide insights to future works that study the effect of asymmetries.

Asymmetries of hurricanes are roughly classified into deformations of eyewall, inner rainbands and outer rainbands based on their distance from the center of the hurricanes [Wang, 2009, Houze, 2010, Moon & Nolan, 2015], and different asymmetries may be associated with different dynamics. However, the classification based on distance is somewhat subjective, and the connection between asymmetries at different radii may possibly be ignored. Previous studies [Reasor et al., 2000, Wang, 2001, Chen & Yau, 2001, Wang, 2002, Corbosiero et al., 2006] usually focus on a limited region of radius and study the characteristics of asymmetries from either Hovmöller diagrams or a series of snapshot structures. However, without diving into the frequency and wavenumber space, it is hard to properly disentangle different wave signals. Therefore, one of our goals is to systematically classify the asymmetries based on their dominant dispersion relations examined both near and beyond the

eyewall. Once different types of asymmetries are identified, we can then shed light onto the mechanisms that give rise to the asymmetries.

Earlier studies [Abdullah, 1966, Kurihara, 1976, Willoughby, 1978, Diercks & Anthes, 1976, Willoughby et al., 1984] mainly view the spiral rainbands as inertia-gravity waves, while Macdonald [1968] first suggests the existence of Rossby-like waves based on the observations from satellite and radar, and near-surface wind. For the asymmetries adjacent to or close to the inner core region, Guinn & Schubert [1993] and Montgomery & Kallenbach [1997] develop the theory of vortex-Rossby waves, and view those inner rainbands as packets of vortex-Rossby waves. Simulations [Chen & Yau, 2001, Wang, 2002] and observations [Reasor et al., 2000, Corbosiero et al., 2006] further confirm the existence of cloud bands and vorticity bands, whose propagation properties are consistent with the prediction of vortex-Rossby wave theory. However, both vortex-Rossby waves and inertia-gravity waves are marginally stable by themselves, so they require either external forcing to excite and maintain them, or coupling mechanisms for them to be linearly unstable. Possible instability mechanisms include barotropic instability that originates from two phase-locked counterpropagating vortex Rossby waves on each side of the potential vorticity (PV) peak [Montgomery & Shapiro, 1995]. Such instability has been used to explain the features such as polygonal eye structure and mesovortices in real world TCs [Reasor et al., 2000, Kossin & Schubert, 2004]. In addition to the barotropic instability, studies [Ford, 1993, 1994a, Schecter & Montgomery, 2004, Menelaou et al., 2016] suggest another instability mechanism where a vortex-Rossby wave can grow by emitting a frequency-matched outward-propagating inertia-gravity wave. Chow et al. [2002] finds that the radial structure of large-scale moving spirals from an idealized full-physics simulation

are similar to the analytical solution of inertia-gravity waves radiated by vorticity fluctuations from the inner vortex. Menelaou et al. [2016] also explores the situation where both barotropic instability and vortex Rossby inertia-gravity wave instability coexist. Instead of vortex-Rossby waves and inertia-gravity waves, Moon & Nolan [2015] suggests that the inner rainbands in their simulation are simply convection being advected and deformed by the strong shear of the mean-vortex.

Although some studies [Chen & Yau, 2001, Wang, 2002] suggest that vortex Rossby waves and the convective asymmetries are a highly coupled system, the convectively coupled aspects are not extensively studied by the aforementioned papers. Some recent studies [Schecter & Montgomery, 2007, Menelaou et al., 2016, Lahaye & Zeitlin, 2016]) have included convective coupling into their framework, and addressed the effect of convection on the instability mechanisms. In their coupled model, the convective heating is simply parameterized to be proportional to low level horizontal convergence, thus only the effect of reduced stratification due to convection is included. However, the effect of convection could be much more complicated than that. Yet, a systematic study of the convectively coupled aspect of the azimuthal asymmetries in hurricanes is still lacking. It is not yet clear whether there exist any dominant modes in the full physics simulations of hurricanes, what their preferred azimuthal wavenumbers and rotating frequencies are, and how their structures look like.

To summarize, the goal of this study is to systematically document the asymmetric characteristics of an idealized simulation of hurricanes, i.e. their preferred frequencies and azimuthal wavenumber, and their structures, to classify the asymmetries based on the dispersion relation near and beyond the eyewall, and to connect the dominant asymmetries to plausible instability mechanisms. In addi-

tion, we will focus on the convectively coupled nature of these asymmetries. We will introduce our model configurations and simulations in section 2.2, and describe the statistical methodology being used in section 2.3. In section 2.4, we will discuss the results from the space-time spectral analysis and the structure of the dominant modes. Section 2.5 will highlight the main conclusions and discuss potential directions for future works.

2.2 Model configuration and initial condition

In order to conduct meaningful space-time spectral analysis and compare with dispersion relationship of different types of waves, we require output with high spatiotemporal resolution [Reasor et al., 2000]. Therefore, the Weather Research and Forecasting (WRF) model is used in this study to generate a 10-member ensemble simulation of an idealized tropical cyclone. The model configuration is similar to those used in a previous idealized hurricane study [Zhu & Zhu, 2014]. The model surface is set to be sea surface with homogenous surface temperature of 29°C. All simulations are performed on an f-plane with a constant Coriolis parameter equivalent to that at 20°N. Simulations are done over three two-way nested domains with a horizontal resolution of 2km, 6km, and 18km and domain size of 600km×600km, 1080km×1080km and 5400km×5400km. Doubly-periodic lateral boundary conditions are applied to the outermost lateral boundaries. The outermost domain is large enough to prevent the interaction among hurricanes across the lateral boundaries. There are 47 levels in the vertical with a model top at approximately 20hPa. Rayleigh damping is applied to the top 5 km of the domain. Each simulation is run for 10 days, which allows the vortex to reach a

sufficiently long steady state for further analysis, and the output of the first two days is discarded as spin-up. History snapshots are output every 10 minutes.

We use the Mellor-Yamada-Janjic (MYJ) scheme [Janjić, 1996, 2001] for the subgrid-scale (SGS) vertical turbulent mixing, and the 2-D Smagorinsky [1963] turbulence scheme for horizontal diffusion. The Charnok formula [Charnock, 1955], used in the MYJ surface scheme to determine surface roughness, is replaced by the formula proposed by Davis et al. [2008] to reflect the observed variation of drag coefficient in the high wind regime [Donelan et al., 2004]. We choose the Thompson scheme [Thompson et al., 2004, 2008] for microphysics, and the Kain-Fritsch scheme [Kain, 2004] as the cumulus parameterization for the outermost domain. No cumulus parameterization is used in the two inner domains. For longwave radiation, we use the Rapid Radiative Transfer Model radiation (RRTM) scheme [Mlawer et al., 1997]. Different from Zhu & Zhu [2014], incoming shortwave radiation is set to zero to prevent any periodic external forcing. Since this idealized study focuses on internally-generated asymmetries in TCs, vertical wind shear and other environmental forcing are not imposed in the simulations. Such simplification allows us to connect the asymmetries found in this study to previous theoretical studies [Montgomery & Shapiro, 1995, Ford, 1993, 1994a, Schecter & Montgomery, 2004, Menelaou et al., 2016].

The ensemble simulations are initialized with an idealized category-1 hurricane vortex, and the temperature and the pressure fields are in hydrostatic balance and gradient wind balance with the vortex wind. The radial profile of the tangential wind is determined based on Wood & White [2011]'s formula, and the vertical extension is based on an analytical function proposed by Nolan & Montgomery [2002]. The initial far-field temperature and humidity profiles are specified by the non-

Saharan air layer sounding of Dunion & Marron [2008], which is a modified and extrapolated version of Jordan [1958]. Each ensemble member is initialized with the same initial vortex and initial sounding, but with random perturbations of 0.1K in temperature below 800m, which is different from Zhu & Zhu [2014] where no random noise is applied.

2.3 Data and methodology

The data in the innermost domain from the WRF simulations is used for further analysis. The data is mapped from the Cartesian coordinate onto a polar coordinate (r, φ) with coarsened azimuthal resolution, where r is the radial coordinate, and φ is the azimuthal angle. The resolution is 2km in r and $\pi/16$ in φ, whose azimuthal resolution is effectively 15km at a radius of 80km. The mapping is done by averaging all the available grid points within a single arc-shaped area $dr \times d\varphi$ around each (r_0, φ_0). All the fields, except for convective heating, are obtained by this mapping method. For convective heating, we need to include the contribution from scales smaller than that of the coarsened polar coordinate resolution in addition to diabatic heating, although diabatic heating is a major component of convective heating. Therefore, the convective heating is calculated as the diabatic heating plus the eddy contribution

$$\bar{J}_{conv} = \bar{\dot{\vartheta}} + \frac{\partial \overline{u'\vartheta'}}{\partial r} + \frac{1}{r}\frac{\partial \overline{v'\vartheta'}}{\partial \varphi} + \frac{1}{\overline{M}}\frac{\partial \overline{\omega'\vartheta'}}{\partial \eta}, \tag{2.1}$$

where $\dot{\vartheta}$ is the diabatic heating, u', v', ω' and ϑ' are the perturbation radial velocity, azimuthal velocity, pressure vertical velocity and potential temperature, and $\overline{M}$ is the column mass in pressure

units. The overbar is used as for most radii, the mapping into polar coordinate with 32 points in the azimuthal represents an average.

In order to find the preferred azimuthal wavenumber and frequency of the azimuthal asymmetries, a power spectrum is obtained for each field at a specific radius by a 2-D spectral analysis in time and azimuthal angle. For a 3-D field, such as temperature and specific humidity, its power spectrum is based on its lower-level (about 800hPa) field. Each field has a dimension of 1152 in time (8 days for each simulation with 10-minute sampling frequency, after discarding the first 2 days as spin-up) and 32 in the azimuthal direction. For each simulation, the power spectrum is obtained and averaged over successive 3-day segments with 2-day overlapping. Within each segment, the original data is linearly de-trended. Both ends of each segment are then tapered to zero by multiplying by the Hann window function. The time-averaged component is then added back to the time series to retain zero-frequency power. Finally, the power spectrum is obtained by averaging over 10 radii (or 20km) near the specified radius, and over the 10 ensemble simulations to increase its signal-to-noise ratio.

Both the vertical and horizontal structures of a distinct mode are obtained through linear regression of a filtered field against a filtered time-series index. To obtain the filtered time-series index, a given variable at a specific radius (and a specific height for 3-D variables) is filtered by a pre-defined frequency-wavenumber window based on the power spectrum analysis. Then we choose the filtered variable at any azimuthal angle to be the time-series index. Due to the symmetry of the variability of the given variable along the azimuthal direction, the choice of azimuthal location of the filtered index does not make much difference to the resulting structure, except for a phase shift. Other fields filtered by the same frequency-wavenumber window are then linearly regressed against the filtered

time-series index. The structures are constructed using simulations from day 3 to day 10, and are scaled to correspond to 2-σ of the filtered index.

One drawback of the methodology discussed above is that the selection of the frequency-wavenumber windows for filtering can be somewhat subjective. Therefore, in addition to the regression method, we applied EOF analysis on the combined field of temperature, vertical velocity and specific humidity, to see if the fast and the slow waves can be extracted objectively. The perturbation temperature, specific humidity and pressure vertical velocity at a given radius are detrended and normalized so that their magnitudes are comparable and can be concatenated into a single field for the EOF analysis.

2.4 Results

2.4.1 Mean state

Before we discuss the asymmetric variability of the hurricanes, we first show the azimuthal mean structure of the ensemble simulations, because any asymmetric variabilities are subject to the azimuthal-averaged background structure. Figure 2.1 shows the ensemble-averaged time-averaged (48h to 144h) azimuthal mean structure of azimuthal velocity, radial velocity, vertical velocity and potential vorticity. The maximum azimuthal mean azimuthal velocity reaches 100m/s at around 25km to 30km in radius. Its maximum is tilted outward with increasing height. Strong upward motion is co-located with the maximum of azimuthal velocity. Outside the eyewall, between 50km to 150km, the azimuthal mean vertical velocity is weakly descending. The radial velocity has a strong inflow within

the boundary layer below 800 hPa, and an outflow layer above 200 hPa. Potential vorticity (PV) is stronger in the lower troposphere, and peaks around a radius of 20km.

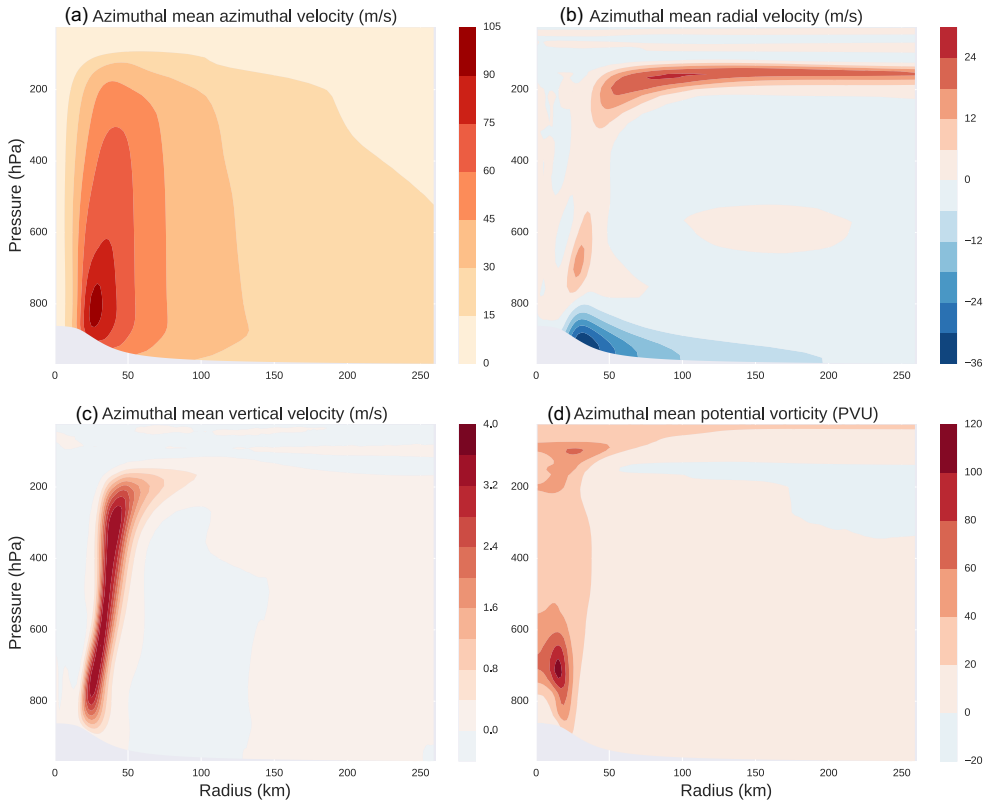

Figure 2.1: Ensemble-averaged time-averaged (48h-144h) azimuthal mean structure of (a) tangential wind speed (m/s), (b) radial wind speed (m/s), (c) vertical wind speed (m/s), and (d) potential vorticity (PVU)

Figure 2.2 shows the time series of the maximum azimuthal wind speed at the surface and its corresponding radius, for each ensemble member and for their average. It indicates that the simulated hurricanes undergo substantial intensification during the first day, and transition to a slow intensification period from day 2 to day 4, and finally develop into a steady stage after day 4. With the first two days discarded as spin-up, the spectral analysis can be meaningfully done over the remaining

days, and as we will see in section 2.4.2 the results are not sensitive to whether the slow intensication period is included or not.

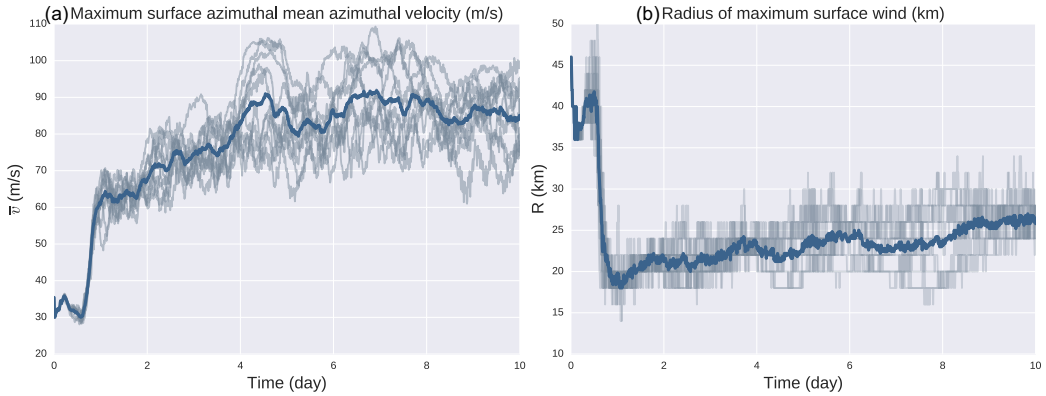

Figure 2.2: Time series of (a) maximum azimuthal mean tangential wind speed at surface (m/s), and (b) the corresponding radius of the maximum surface azimuthal wind (km), of each ensemble member (in light grey) and the ensemble average (in thick blue).

2.4.2 Power spectrum

In this section, we will conduct space-time spectral analysis near and beyond the eyewall to determine whether there are distinctive power peaks, and to identify the dispersion relationship they follow. We choose the radius of 30km and 80km to be the areas around which the power spectral analysis will be conducted, because the azimuthal variance of temperature and moisture peaks around these two radii as shown in Figure 2.3.

Figure 2.4 shows the ensemble-averaged power spectrum of lower level (1.5km) simulated radar reflectivity around 30km and 80km. The black line indicates the local background rotation speed. The red boxes indicate the frequency and wavenumber window that will be used to filter the fast wave

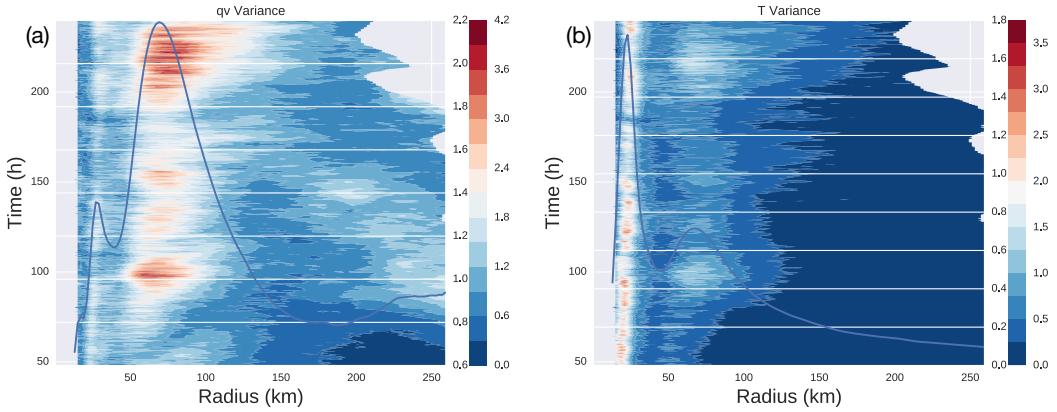

Figure 2.3: Ensemble-averaged total azimuthal variance of lower-level (a) specific humidity ($(g/kg)^2$) and (b) temperature (K^2) as a function of radius and time. The blue lines indicate the time-mean variance.

and the slow wave respectively. Both of the power spectra have two distinctive peaks, one nearly stationary (hereafter slow wave), and the other one (hereafter fast wave) that has a frequency which is slower than the local rotation rate at 30km, but faster than the rotation at 80km. Note that here the slow or the fast wave is defined in the absolute reference frame, while previous studies usually define a "slow" or "fast" regime relative to the local background rotation. The reason why we don't follow this convention here is because the background rotation varies a lot with radius, and a different reference frame would be needed when we discuss asymmetries at different radii. So we think it is less confusing to use an absolute reference frame. Figure 2.5 shows the power spectrum of radar reflectivity at 80km based on simulations from day 4 to day 10 and from day 5 to day 10. The similarity between Figures 2.5 and 2.4(b) indicates that the results are not sensitive to whether the slow intensification period is included or not.

The slow wave is nearly stationary and retro-propagating relative to the background rotation near and beyond the eyewall. Its phase speed is about 75m/s relative to the eyewall rotation, and about

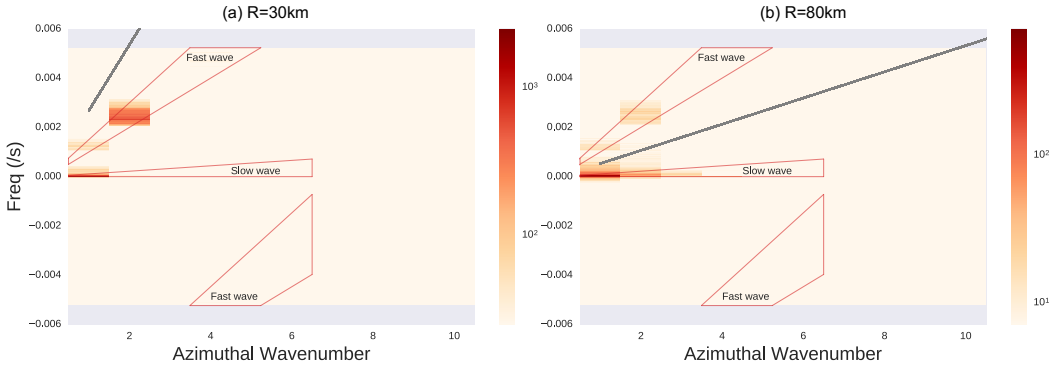

Figure 2.4: Ensemble-averaged power spectrum of lower-level radar reflectivity averaged over radius from (a) 20km to 40km, and (b) 70km to 90km. The black line indicates the background rotation speed, and the red boxes indicate the frequency and wavenumber window that will be used to filter the fast wave and the slow wave respectively.

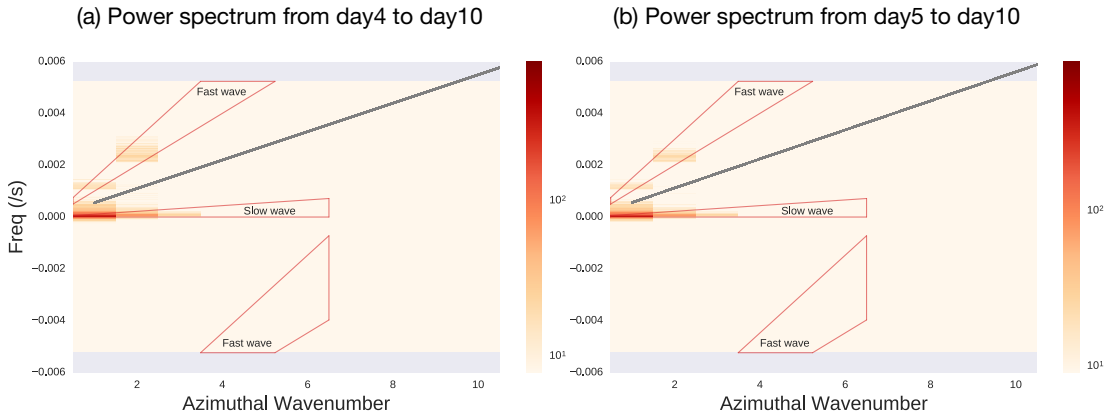

Figure 2.5: Ensemble-averaged power spectrum of lower-level radar reflectivity (dBz) averaged over radius from 70km to 90km, based on simulations from (a) day 4 to day 10, and (b) day 5 to day 10. The black line indicates the background rotation speed

40m/s relative to the background rotation at 80km. The slow wave is unlikely to be a vortex-Rossby wave, because its relative phase speed near the eyewall is too fast to be compatible with the vortex-Rossby wave dispersion relationship [Montgomery & Kallenbach, 1997, Möller & Montgomery, 2000], although the background PV gradient is large near the eyewall. Beyond the eyewall, the background PV gradient is too weak to support a vortex-Rossby wave with 40m/s retro-propagating phase speed.

The fast wave is dominated by a wavenumber-two feature near the eyewall and beyond the eyewall. The phase speed of the fast wave (roughly about 40m/s) is about half of the local rotation rate near the eyewall (about 80m/s), which is consistent with the phase speed of a wavenumber-two vortex-Rossby edge wave propagating on the vorticity discontinuity of a Rankine vortex [Lamb, 1932]. Beyond the eyewall around 80km, the frequency of the fast wave becomes faster than the local rotation rate, therefore it is no longer possible for the fast wave to be a vortex-Rossby wave there. As we will see in section 2.4.3, it resembles more characteristics of an inertial-gravity wave. The frequency of the fast wave suggests that it is very likely to be a mixed vortex-Rossby-inertial-gravity wave [Montgomery & Lu, 1997, Zhong et al., 2009].

To see if the two peaks in the power spectrum of radar reflectivity are a consistent feature among other variables, power spectra of lower-level temperature, specific humidity, vertical velocity, convective heating, outgoing longwave radiation (OLR) and precipitation around 80km are shown in Figure 2.6. For 3-D variables, the power spectra are taken at a lower level, around 800 hPa. Power spectra of some other fields are also calculated, but not shown here, as they are largely redundant to the ones shown.

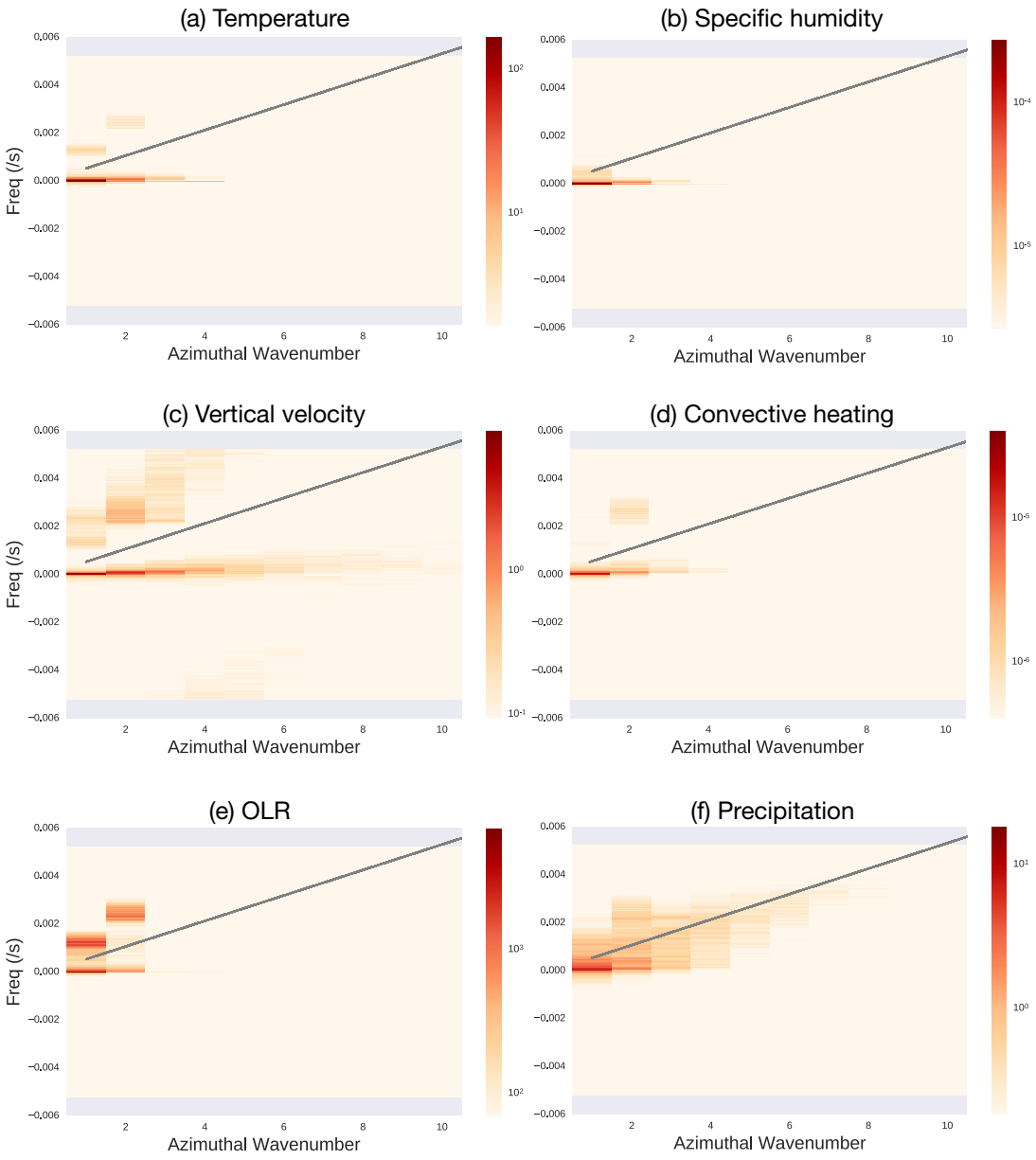

Figure 2.6: Ensemble-averaged power spectrum of (a) lower-level temperature (K), (b) specific humidity (kg/kg), (c) vertical velocity (m/s), (d) convective heating (K/s), (e) OLR (W/m^2) and (f) precipitation (mm/10min) averaged over radius from 70km to 90km. The black line indicates the background rotation speed.

Despite the similarity among power spectra of different variables, there are certain differences across them. First, the power spectrum of vertical velocity (Figure 2.6(c)) is more spread into higher azimuthal wave numbers and a wider frequency range, because the vertical velocity is noisier and smaller in scale. In addition, the specific humidity has little power for the fast wave which is consistent with the difference in magnitude of its vertical structures (Figures 2.8(d) and 2.10(d)). Third, the power spectrum of OLR has stronger power for the fast wave, whereas other variables have their power mainly concentrated in the nearly stationary wave. This is because OLR could be greatly affected by high clouds and upper-level temperature, while other power spectra are based on lower-level (around 800hPa) fields.This height dependence can be more clearly seen from the vertical structure of temperature (Figure 2.10(b)) of the fast wave. Lastly, unlike other fields, the power spectrum of the precipitation rate (Figure 2.6(f)) does not have two distinctive peaks, but rather merge in the middle. This is because the rain rate is not linearly related with other fields, and it has very a skewed distribution and long tail of positive anomaly (not shown). If we simply convert the radar reflectivity into rainfall rate by an exponential relationship, we will be able to reconstruct the power spectrum of precipitation rate (not shown).

2.4.3 Structure of the dominant modes

Given the similarity of space-time spectrum across different fields and our main focus on convectively coupled waves, we choose low-level radar reflectivity, whose horizontal structure of the slow and the fast waves are shown in Figures 2.7(a) and 2.9(a), to construct the window-filtered index to further obtain the vertical and horizontal structure of the dominant perturbation. Based on the

methodology described in section 2.3, the structures are obtained by first taking the regression of each filtered field against the filtered radar reflectivity, and then plugging in 2 standard deviations of the index to the linear regression model.

Figures 2.7 and 2.8 show the horizontal and vertical structure of the slow wave respectively. The slow-propagating wave shows a predominant wavenumber-one feature. Because the frequency of the slow wave is slower than the local background rotation, the wave pattern should propagate anti-cyclonically (or leftward in the vertical structure plot) relative to the mean flow. At 8okm, the positive temperature perturbation lags the descending vertical velocity by $\pi/2$ toward the right, indicating that a descending vertical motion is followed by a positive temperature anomaly. Such behavior is consistent with a gravity wave propagating anti-cyclonically. The temperature perturbation features a structure of the second baroclinic vertical mode above the boundary layer inflow (8oohPa) and below the upper outflow layer (2oohPa), while the vertical velocity and convective heating fields feature a stronger first baroclinic vertical mode component, and a weak second baroclinic mode that tilts the fields toward right with increasing height. The strongest humidity perturbation is capped under 6oohPa, and the perturbation is slanted vertically against the direction of wave propagation.

The vertical structure of both thermodynamic and dynamic fields are similar to the structure of convectively coupled waves found in Haertel & Kiladis [2004], Kiladis et al. [2009], suggesting a convectively coupled origin of this wave. The coexistence of the first and the second baroclinic structures also suggest the important role that the interaction between vertical modes plays in the slow wave.

The horizontal structures of temperature and humidity of the slow wave show a clear wavenumber-

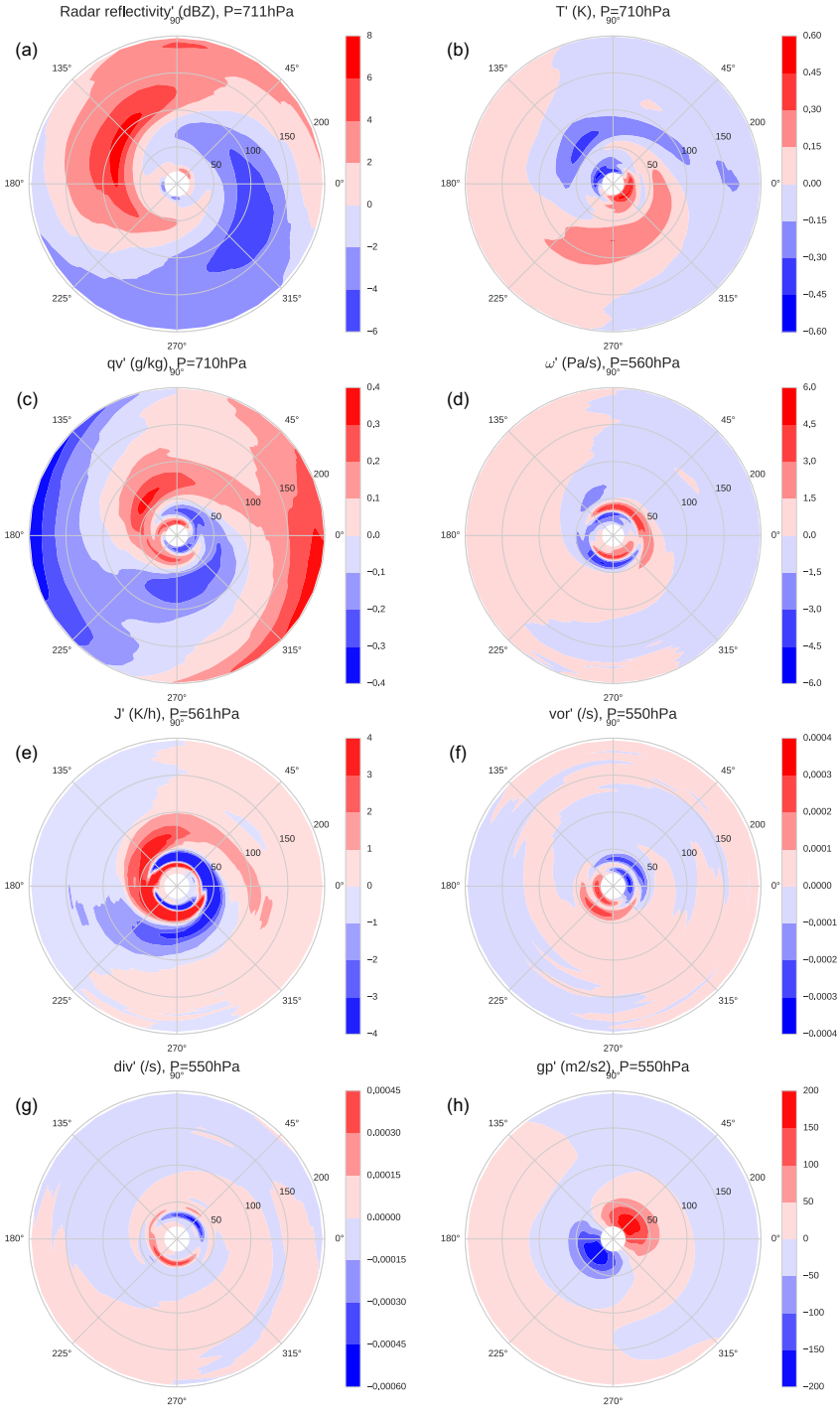

Figure 2.7: Horizontal structure of (a) radar reflectivity (dBZ), (b) temperature (K), (c) specific humidity (g/kg), (d) vertical velocity (Pa/s), (e) convective heating(K/s), (f) vorticity (/s), (g) divergence (/s) and (h) geopotential (m^2/s^2) of the slow wave.

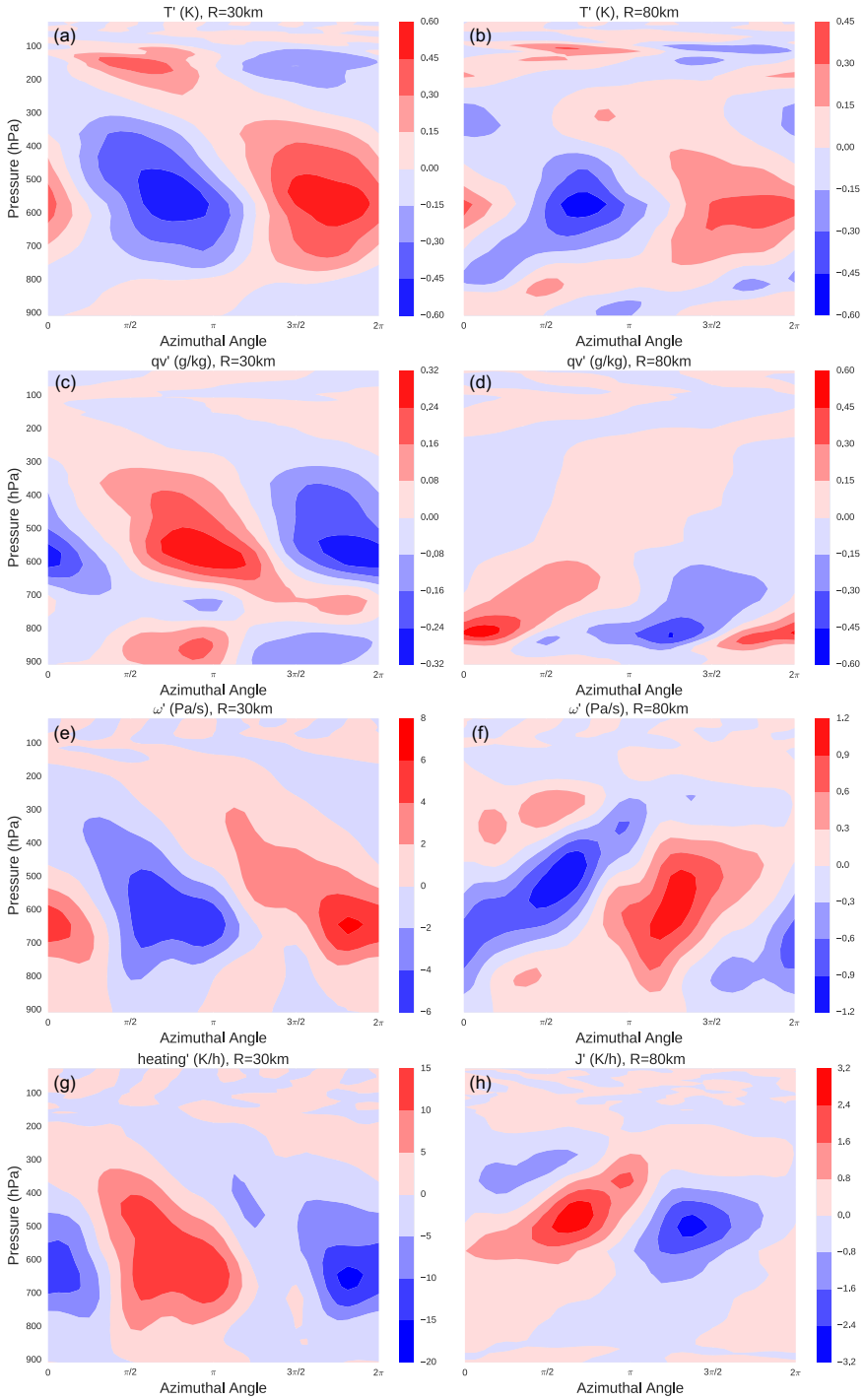

Figure 2.8: Vertical structure of (a) and (b) temperature (K), (c) and (d) specific humidity (g/kg), (e) and (f) vertical velocity (Pa/s) and (g) and (h) convective heating (K/h) of the slow wave at the radius of 30km (left panel) and 80km (right panel).

one banded structure. The amplitudes peak at two radii, one in the inner core region, and the other one widely expanded outside the eyewall. This is consistent with the fact that their power near (Figure 2.4(a)) and beyond the eyewall (Figure 2.4(b)) are comparable for the slow wave. The branches spiral in cyclonically, which indicates that the wave is propagating outward. Figure 2.7 (f), (g) and (h) show the vorticity, divergence and geopotential of the slow wave. Although we suspect the slow wave to be an inertia gravity wave, it still has a slight vorticity component Zhong & Zhang [2014]. The divergence and geopotential fields are not exactly quadratic in phase as are the inertia gravity waves in simple eigenfrequency models Montgomery & Lu [1997], Zhong & Zhang [2014]. We suspect that this is because the stratification and other convective responses can vary along radius and alter the structure of these fields.

Figures 2.9 and 2.10 show the horizontal and vertical structure of the fast-propagating wave. The structures are dominated by a wavenumber-2 perturbation, as expected from the power spectral analysis. A wavenumber-2 dominated perturbation in the eyewall is also consistent with the findings in observations [Reasor et al., 2000, Kuo et al., 1999]. At 80km, the positive temperature perturbation lags the descending vertical velocity by $\pi/2$ in phase toward the left, which is consistent with a gravity wave propagating cyclonically. Unlike the slow wave, the vertical structure of the fast wave is predominately barotropic below the outflow layer. Note that the vertical temperature and specific humidity structures of the fast wave and the slow wave are plotted in the same color scale (although the colorbars are different), therefore it can be easily seen that the fast wave has a slightly weaker temperature field below the outflow layer and a much weaker specific humidity field compared to those of the slow wave. Its horizontal structure shows a stronger perturbation within the inner vortex and

a relatively weak spiral perturbation outside. As shown in Figure 2.9 (f), (g) and (h), near the inner core region, a positive vorticity anomaly corresponds to a negative geopotential perturbation, which indicates that it behaves more like a vortex Rossby wave. Moving outward, vorticity is no longer anti-correlated with geo-potential. Divergence flow is followed by a negative geopotential perturbation, which is consistent with a cyclonic propagating gravity wave.

The frequency and horizontal structures of the fast wave are very similar to those of the unstable mixed vortex Rossby inertia gravity wave found by Schecter & Montgomery [2004], Menelaou et al. [2016]. This type of wave has a strong vortex Rossby wave component in the inner core region, where the radial gradient of background potential vorticity is strong, while emitting a frequency matched gravity wave outward where the PV gradient becomes negligible. The instability of such a wave originates from the interaction between the vortex Rossby wave and inertia gravity wave. Unlike convectively coupled instability, the instability of such a wave does not require any interaction between vertical modes, which is consistent with its barotropic vertical structure. The findings suggest that the fast wave is a very different type of wave than the slow wave, and they may have very different instability mechanisms, which we will explore in a following study.

Because the selection of the filtering windows is somewhat subjective, we also applied EOF analysis on the combined field of temperature, vertical velocity and specific humidity, to extract the fast and the slow waves more objectively. We found that the first two pairs of EOF modes are able to capture the structure of the fast and the slow wave, although the variation explained by them is less than 25%. Figure 2.11 is showing an example of the first four EOFs of one of the ensemble members. EOF1 and EOF2 resemble the structure of the slow wave, and EOF3 and EOF4 reproduce the

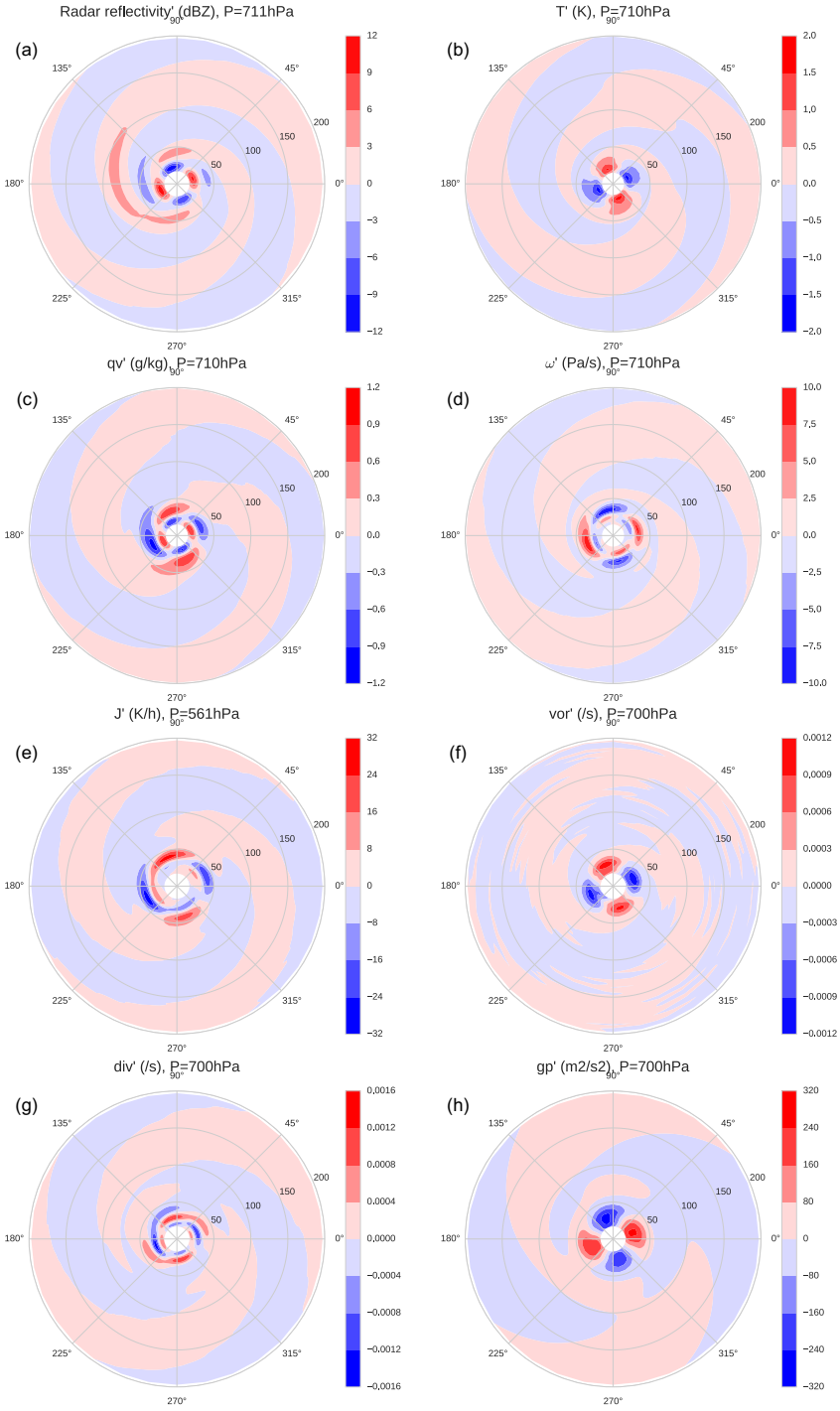

Figure 2.9: Horizontal structure of (a) radar reflectivity (dBZ), (b) temperature (K), (c) specific humidity (g/kg), (d) vertical velocity (Pa/s), (e) convective heating(K/s), (f) vorticity (/s), (g) divergence (/s) and (h) geopotential (m^2/s^2) of the fast wave.

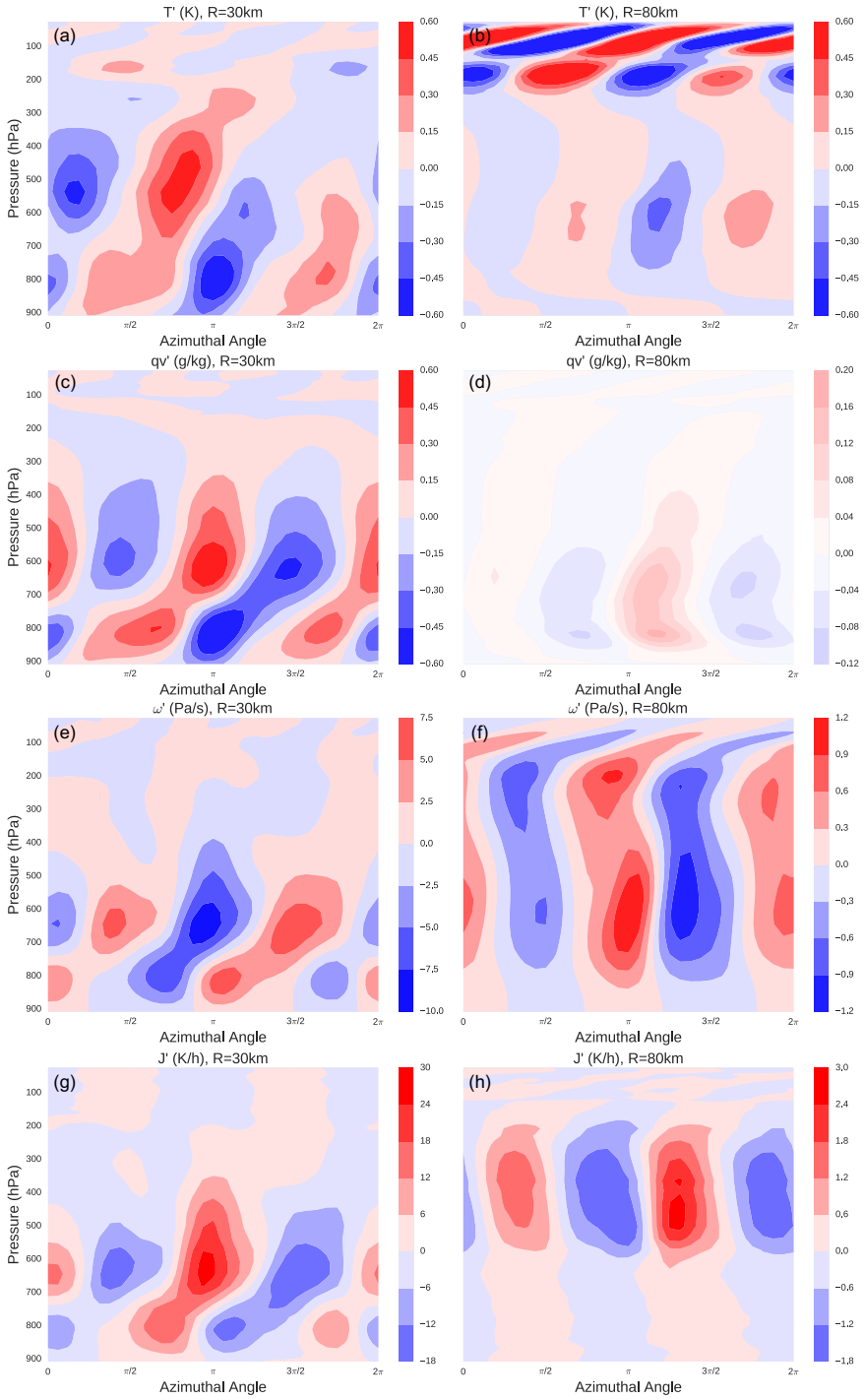

Figure 2.10: Vertical structure of (a) and (b) temperature (K), (c) and (d) specific humidity (g/kg), (e) and (f) vertical velocity (Pa/s) and (g) and (h) convective heating (K/h) of the fast wave at the radius of 30km (left panel) and 80km (right panel).

structure of the fast wave. We need to note that the order of the leading EOFs are specific to this ensemble member. Although EOF analysis is able to extract the fast and the slow wave objectively, there are several limitations of using EOF analysis. First, EOF analysis distinguishes modes with different wavenumber and frequency as different EOF modes even if they have similar phase speed and belong to the same type of wave. Second, two EOFs which are orthogonal to each other are needed to represent a single propagating wave. Third, the order of the leading EOFs and the phase of each EOF mode are not consistent across ensemble members which makes it difficult to construct the composite.

2.5 Conclusions

There are two distinct spectral peaks in the power of asymmetries in the simulated hurricanes near and outside the eyewall based on the space-time spectral analysis. The fast propagating wave propagates much faster than the local background rotation outside the eyewall, and is believed to be associated with vortex Rossby perturbations in the inner core region. The unstable mixed vortex-Rossby-inertial-gravity wave from a simple eigenfrequency model [Schecter & Montgomery, 2004, Menelaou et al., 2016] resembles the structure of such fast-propagating wave. The fast-propagating wave has very strong perturbations within or near the eyewall, and relatively weak perturbations outside the eyewall. The other spectral peak is nearly stationary. However, intrinsically it is a fast retro-propagating gravity wave. The vertical structure of the dynamic and convective fields of this wave resemble those of convectively coupled waves, and encourage us to explore more on the effect

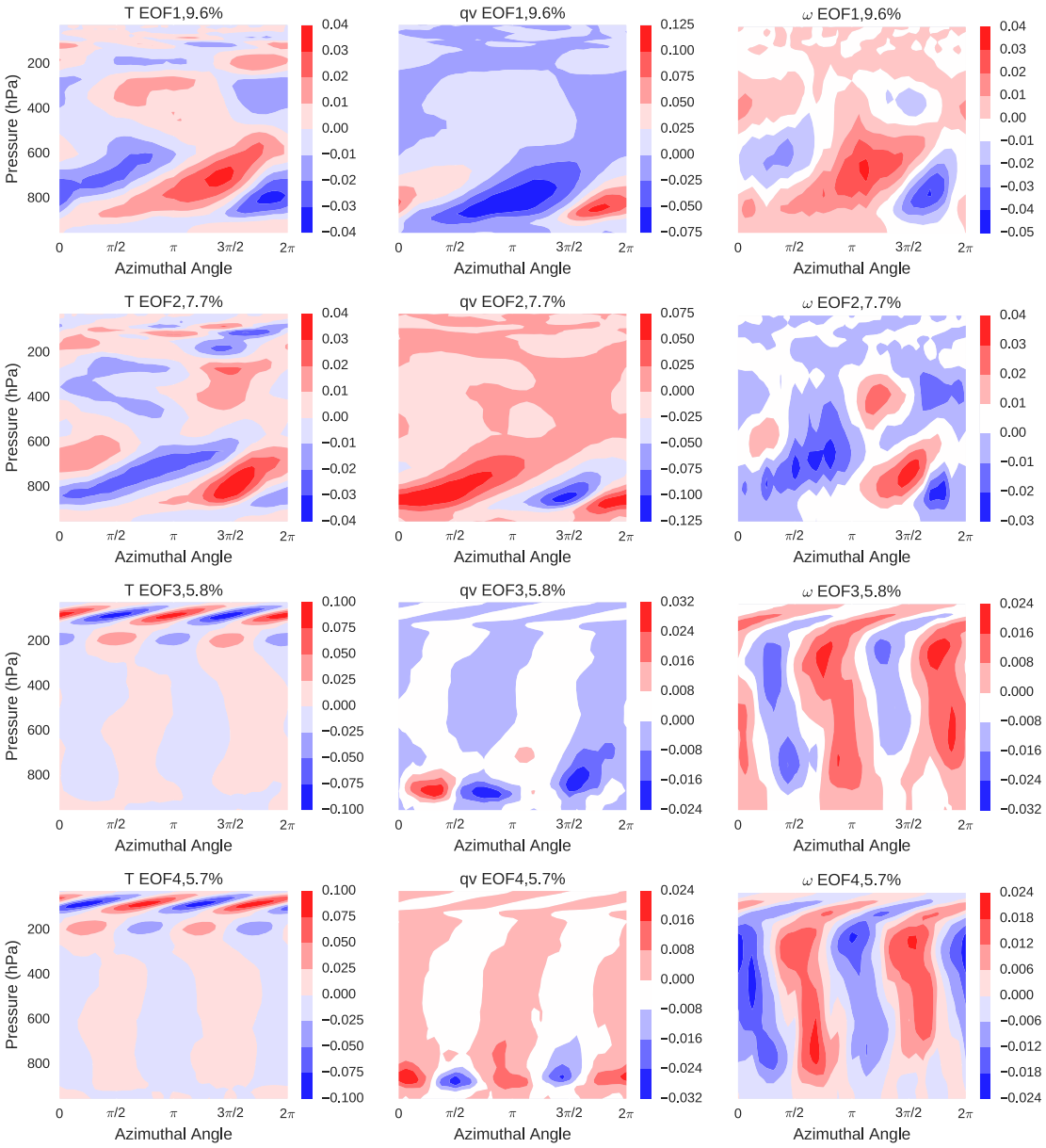

Figure 2.11: Leading EOFs of the temperature (left panel), specific humidity (middle panel) and vertical velocity (right panel) of one of the ensemble members at the radius of 80km.

of convective coupling.

One of the limitations of this work is that the characteristics of the asymmetries are only examined based on a single azimuthal mean hurricane structure. As some previous studies [Montgomery & Lu, 1997, Schecter & Montgomery, 2004, Menelaou et al., 2016] pointed out, the structures and the frequencies of the dominant asymmetries can vary with the background vortex structure, especially for the fast-propagating wave as its inner part is associated with a vortex-Rossby wave that is highly dependent on the background vorticity and its gradient. We are aware of the sensitivity of the asymmetries to the intensity, size and structure of the hurricane, however the sensitivity study is beyond the scope of this work. Another limitation is that the setup of the simulation is not realistic enough to include environmental forcing such as vertical wind shear or the beta-effect, and those external forcings may play a role in the convective and kinematic asymmetries. Therefore, the dominant asymmetries found in this study might not necessarily apply to more realistic simulations. Such effect due to external forcing is beyond the scope of this work, and will be addressed in future studies.

3

Convectively coupled linear instability in TC-like vortices

3.1 Introduction

In the first chapter, we studied the asymmetries near and outside the eyewall in an ensemble of idealized hurricane simulations. We identified the dominant modes based on the power spectra of the

asymmetric signals and roughly classified their wave types according to their dispersion relationship and the regressed vertical and horizontal structures. We suspect that the fast propagating wave is related to the vortex-Rossby-inertia-gravity wave, and the near stationary wave is likely a gravity wave. In this chapter, we are going to focus on the instability mechanisms that can potentially give rise to the dominant modes observed in the WRF simulations.

Various instability mechanisms have been proposed to understand the asymmetric feature in tropical cyclones, including barotropic instability, mixed vortex-Rossby-inertia-gravity instability, and potentially convectively coupled instability. Barotropic instabilities are a well-established instability mechanism which can broadly exist in sheared flows [Rayleigh, 1880, Fjørtoft, 1950, Kuo, 1949]. In the context of tropical cyclones, barotropic instabilities can emerge when the radial gradient of the background potential vorticity (PV) reverses its sign and allows two counterpropagating vortex Rossby waves to be phase-locked on each side of the PV peak [Peng & Williams, 1991, Weber & Smith, 1993, Montgomery & Shapiro, 1995, Schubert et al., 1999]. The barotropic instability has been used to explain asymmetric features in the inner-core region, such as polygonal eye structure [Schubert et al., 1999, Reasor et al., 2000], mesovortices [Kossin & Schubert, 2001, 2004] and vortical swirls in hurricane eyes [Kossin et al., 2002] in real-world TCs.

The aforementioned barotropic instability is usually studied by a simplified non-divergent model because divergence is not critical to barotropic instability. However, when divergence is taken into account and allows the inertia-gravity wave to propagate, there can be another type of instability, called mixed vortex-Rossby-inertia-gravity instability [Ford, 1993, 1994a,b, Schecter & Montgomery, 2004, Menelaou et al., 2016]. This type of instability is excited by a vortex-Rossby wave in the inner

vortex resonating with a frequency-matched outward-propagating inertia-gravity wave. The instability mechanism is similar to an earlier finding of the Lighthill radiation mechanism [Lighthill, 1952], in which a vortical source generates frequency-matched acoustic waves in the compressible flow. Ford [1994a,b] first investigated the instability of an axisymmetric vortex with a single radial discontinuity in potential vorticity with a shallow-water model and suggested that the growth rate of the instability was too weak to be of practical interest with the order of unity Froude numbers (Fr) and Rossby numbers (Ro). Schecter & Montgomery [2004] investigated the instability mechanism of Rankine-type vortices with $\mathrm{Ro} \gg 1$, which is typical for intense hurricanes. They found that the e-folding growth time scale can be as small as several rotation periods in some cases, but the growth rate decays with the smoothness of the vortex edge. Menelaou et al. [2016] further explored the instability with non-monotonic background vortices and found that barotropic instability contributes to the overall instability in addition to the vortex-Rossby-inertia-gravity instability. In an idealized full-physics simulation, Chow et al. [2002] observed that the perturbation vertical velocity behaves as large-scale moving spirals, and their structure is similar to the analytical solution of inertia-gravity waves radiated by vorticity fluctuations from the inner vortex.

However, the vortex-Rossby-inertia-gravity instability still has its limitations in explaining the asymmetries of tropical cyclones in the following ways. First, the instability is sensitive to the background vortex, such as the strength of the inner vortex, the smoothness of the vortex edge [Schecter & Montgomery, 2004], the depth of the inner vortex hole, the thickness of the annulus, the background stratification and the strength of a PV skirt outside the main vortex [Menelaou et al., 2016]. Given such sensitivity, the instability is not very robust as the background vortex varies. Second, the

mixed vortex-Rossby-inertia-gravity wave has relatively weaker inertia-gravity wave spirals compared to its inner-core vortex-Rossby wave perturbations. Therefore this instability mechanism is mostly used to explain the development of elliptical or polygonal eyewall rather than spiral rainbands.

Convective coupling is another mechanism that can potentially lead to instability of the asymmetries in tropical cyclones. Many studies [Chen & Yau, 2001, Wang, 2002] have suggested that vortex Rossby waves and the convective asymmetries are a highly coupled system. On one hand, convection influences the cyclone-scale circulation through diabatic forcing. On the other hand, convection is modified by the large-scale flow, such as large-scale convergence or the moisture advection. However, the role of convections on the wave instabilities in tropical cyclones is not fully understood. Therefore, it is crucial to incorporate the feedback between convections and the dynamics of the tropical cyclones to understand the instability mechanisms.

Some efforts have been made to study the effect of convection on TC-like vortices. Schecter & Montgomery [2007] investigated the effect of non-precipitating clouds on the linear instability of TC-like vortices. They applied a buoyancy reduction factor in their linearized model to account for the locally reduced stratification due to convective heating, and they found that the reduced stratification near the eyewall weakened the barotropic instability. It also damps the mixed vortex-Rossby-inertia-gravity instability by enhancing the critical layer damping. Lahaye & Zeitlin [2016] further studied the saturation of instabilities of TC-like vortices using a non-linear model with the effects of moist convection. They found that the inertia-gravity wave emission is substantially stronger and lasts for a much longer time compared to the dry case and the simulation without evaporation, due to a strong convergence zone outside of the vortex.

However, the effect of convection can be much more complicated than simply reducing stratification. Given the complexity of convection and its significant effect on instability mechanisms of the hurricane asymmetries, we are going to investigate the convectively coupled instability of TC-like vortices in this chapter, by incorporating a two-baroclinic-mode convective parameterization with an eigenfrequency model. We will introduce the eigenfrequency framework and a simple model for convective parameterization in section 3.2. In section 3.3, we will discuss the results from the convectively coupled eigenfrequency model. Section 3.4 will highlight the main conclusions and discuss potential directions for future work.

3.2 Model description

In this section, we are going to introduce the convectively coupled eigenfrequency framework that will be used to study the unstable normal modes of TC-like vortices. The framework consists of the dynamic perturbation equations as a response to convective heating and a simple two-mode convective parameterization. The coupled model will ultimately lead to a standard matrix eigenvalue problem, whose eigenvalues represent the growth (or damping) rate and the propagating speed of the normal modes, and the corresponding eigenvectors represent the radial structure of the normal modes.

3.2.1 Dynamic response to convective heating

We now present the 3D perturbation equations linearized around a barotropic vortex whose mean state is in hydrostatic and gradient wind balance. First, we start with the primitive equations in a

cylindrical coordinate (r, λ, z) with hydrostatic and Boussinesq approximations,

$$\frac{\partial u}{\partial t} + u\frac{\partial u}{\partial r} + \frac{v}{r}\frac{\partial u}{\partial \lambda} + w\frac{\partial u}{\partial z} - (f + \frac{v}{r})v = -\frac{1}{\bar{\varrho}}\frac{\partial p}{\partial r} \tag{3.1a}$$

$$\frac{\partial v}{\partial t} + u\frac{\partial v}{\partial r} + \frac{v}{r}\frac{\partial v}{\partial \lambda} + w\frac{\partial v}{\partial z} + (f + \frac{v}{r})u = -\frac{1}{\bar{\varrho} r}\frac{\partial p}{\partial \lambda} \tag{3.1b}$$

$$\frac{\partial T}{\partial t} + u\frac{\partial T}{\partial r} + \frac{v}{r}\frac{\partial T}{\partial \lambda} + w(\frac{\partial T}{\partial z} + \frac{g}{c_p}) = J \tag{3.1c}$$

$$-\frac{\partial p}{\partial z} = \varrho g \tag{3.1d}$$

$$\frac{1}{r\bar{\varrho}}\frac{\partial (r\bar{\varrho} u)}{\partial r} + \frac{1}{r}\frac{\partial v}{\partial \lambda} + \frac{1}{\bar{\varrho}}\frac{\partial (\bar{\varrho} w)}{\partial z} = 0, \tag{3.1e}$$

where (u, v, w) are the radial, azimuthal and vertical velocity respectively in the cylindrical coordinate; p and ϱ represent the pressure and density; T is temperature, J is convective heating, and f is the Coriolis parameter. Overbars represent the basic state in hydrostatic and gradient-wind balance, and primes denote deviation from this basic state, which is assumed to be small. Eqs. (3.1a) and (3.1b) are the horizontal momentum equations; Eq. (3.1c) is the heat equation with diabatic heating incorporated; Eq. (3.1d) represents the hydrostatic balance; and Eq. (3.1e) is the mass continuity equation.

Given that the reference state is a barotropic vortex in hydrostatic and gradient wind balance,

$$-\frac{\partial \overline{p}}{\partial z} = \bar{\varrho} g \tag{3.2a}$$

$$(f + \frac{\overline{v}}{r})\overline{v} = \frac{1}{\bar{\varrho}}\frac{\partial \overline{p}}{\partial r}, \tag{3.2b}$$

we then linearize the governing equations about its basic state, $u = u'$, $v = v' + \overline{v}(r)$, $w = w'$, $p =$

$p' + \overline{p}(r,z)$, $T = T' + \overline{T}(r,z)$, $J = J'$, and we will have

$$(\frac{\partial}{\partial t} + \overline{\Omega}\frac{\partial}{\partial \lambda})u' - \overline{\xi}v' = -\frac{1}{\overline{\varrho}}\frac{\partial p'}{\partial r} \tag{3.3a}$$

$$(\frac{\partial}{\partial t} + \overline{\Omega}\frac{\partial}{\partial \lambda})v' + \overline{\eta}u' = -\frac{1}{\overline{\varrho} r}\frac{\partial p'}{\partial \lambda} \tag{3.3b}$$

$$(\frac{\partial}{\partial t} + \overline{\Omega}\frac{\partial}{\partial \lambda})T' + w'(\frac{\partial \overline{T}}{\partial z} + \frac{g}{c_p}) = J' \tag{3.3c}$$

$$-\frac{1}{\overline{\varrho}}\frac{\partial p'}{\partial z} + \frac{g}{\overline{T}}T' = 0 \tag{3.3d}$$

$$\frac{1}{r\overline{\varrho}}\frac{\partial (r\overline{\varrho}u')}{\partial r} + \frac{1}{r}\frac{\partial v'}{\partial \lambda} + \frac{1}{\overline{\varrho}}\frac{\partial (\overline{\varrho}w')}{\partial z} = 0, \tag{3.3e}$$

where $\overline{\Omega} = \overline{v}/r$ is the mean angular velocity; $\overline{\xi} = f + 2\overline{v}/r$ is the effective Coriolis parameter; and $\overline{\eta} = f + \overline{v}/r + \mathrm{d}\overline{v}/\mathrm{d}r$ is the mean vertical absolute vorticity.

By further assuming a rigid lid at the top of the troposphere and constant buoyancy frequency, we then expand the variables in terms of the baroclinic modes numbered j,

$$(\overline{\varrho}u', \overline{\varrho}v', p') = \sum_j (u_j(r), v_j(r), p_j(r))\frac{H_T}{2j}\cos(\frac{j\pi z}{H_T}) \tag{3.4}$$

$$(\frac{g\overline{\varrho}}{\overline{T}}T', \frac{g\overline{\varrho}}{\overline{T}}J', N^2\overline{\varrho}w') = \sum_j (T_j(r), J_j(r), w_j(r))\frac{\pi}{2}\sin(\frac{j\pi z}{H_T}) \tag{3.5}$$

where H_T is the height of the lid at the top of the troposphere, and $N^2 = \frac{g}{\overline{T}}(\frac{\partial \overline{T}}{\partial z} + \frac{g}{c_p})$ is the buoyancy frequency.

Substituting the expansion forms into the linearized perturbation equations and with some ma-

nipulations, we will have

$$(\frac{\partial}{\partial t} + \overline{\Omega}\frac{\partial}{\partial \lambda})u_j(r) - \overline{\xi}v_j(r) = \frac{\partial T_j(r)}{\partial r} \tag{3.6a}$$

$$(\frac{\partial}{\partial t} + \overline{\Omega}\frac{\partial}{\partial \lambda})v_j(r) + \overline{\eta}u_j(r) = i\frac{n}{r}T_j(r) \tag{3.6b}$$

$$(\frac{\partial}{\partial t} + \overline{\Omega}\frac{\partial}{\partial \lambda})T_j(r) - c_j^2(\frac{1}{r}\frac{\partial(ru_j(r))}{\partial r} + \frac{1}{r}\frac{\partial v_j(r)}{\partial \lambda}) = J_j(r) \tag{3.6c}$$

where $c_j = NH_T/(j\pi)$ is the gravity wave speed of the jth vertical mode. When convective heating is decoupled from the system, i.e., $J_i = 0$, the perturbation equations become essentially the same as the dry dynamic equations used in Schecter & Montgomery [2004], Menelaou et al. [2016].

3.2.2 Convective parameterization

The convective parameterization closely follows Kuang [2008a], Andersen & Kuang [2008], and the key processes and assumptions will be briefly discussed here. The physical meanings of the parameters used in the convective parameterization and their default values from Kuang [2008a], Andersen & Kuang [2008] are summarized in Table 3.1.

For the rest of this chapter, we restrict the model to the first two baroclinic modes, $j = 1, 2$, for simplicity, because they are sufficient to explain most of the convective activity, which will be verified from Chapter 4. For convective parameterization, two more prognostic variables are introduced, q,

the mid-tropospheric moisture anomaly, and L, the lower-tropospheric heating anomaly,

$$(\frac{\partial}{\partial t} + \frac{\overline{v}}{r}\frac{\partial}{\partial \lambda})q = a_1 w_1 + a_2 w_2 - d_1 J_1 - d_2 J_2 \tag{3.7a}$$

$$(\frac{\partial}{\partial t} + \frac{\overline{v}}{r}\frac{\partial}{\partial \lambda})L = \frac{1}{\tau_L}(L_{eq} - L), \tag{3.7b}$$

where a_j and d_j represent the mid-tropospheric moisture tendencies due to vertical advection and convection, respectively. L_{eq} is the lower-tropospheric convective heating that keeps the strict quasi-equilibrium between the boundary layer and the free troposphere, and τ_L is the time scale of L relaxing to L_{eq}. J_1 and J_2 are convective heating of the first two baroclinic modes, and they can be rewritten in terms of lower- (L) and upper- (U) tropospheric heating anomalies,

$$J_1 = L + U \tag{3.8a}$$

$$J_2 = L - U, \tag{3.8b}$$

The total upper-tropospheric heating is assumed to be proportional to the lower-tropospheric heating,

$$\frac{U_0 + U}{L_0 + L} = r_0 + r_q q \tag{3.9}$$

where U_0 and L_0 is the mean-state upper- and lower-tropospheric heating and $r_0 = U_0/L_0$ is the ratio between these two. r_q is the linear dependence of the ratio on mid-tropospheric moisture. The physical intuition behind this formulation is that an anomalously moist mid-troposphere tends to make the entrained air moister than normal and the evaporative cooling weaker than normal.

This effect leads to parcels rising to a greater altitude and heating the upper troposphere more. The opposite process holds for an anomalously dry mid-troposphere. Eq.(3.9) can be linearized into

$$U = L_0 r_q q + r_0 L, \tag{3.10}$$

therefore J_1 and J_2 can be represented in terms of q and L,

$$J_1 = (1 + r_0)L + L_0 r_q q \tag{3.11a}$$

$$J_2 = (1 - r_0)L - L_0 r_q q, \tag{3.11b}$$

To fully close the convective parameterization, lower-troposphere heating is assumed to relax quickly toward the quasi-equilibrium state where convection acts to keep the difference between the boundary layer moist static energy (MSE), h_b, and the vertically averaged lower-tropospheric saturation moist static energy $\langle h* \rangle_{LT}$ constant,

$$(\frac{\partial}{\partial t} + \frac{\overline{v}}{r}\frac{\partial}{\partial \lambda})h_b = (\frac{\partial}{\partial t} + \frac{\overline{v}}{r}\frac{\partial}{\partial \lambda})\langle h* \rangle_{LT}. \tag{3.12}$$

Specifically, the quasi-equilibrium state is achieved by convection in the way that a positive convection anomaly dries and cools the boundary layer through downdrafts and turbulent transport, and it also modifies the lower-tropospheric saturation MSE by heating the atmosphere. These processes

are formulated as

$$(\frac{\partial}{\partial t} + \frac{\overline{v}}{r}\frac{\partial}{\partial \lambda})h_b = -b_1 J_1 - b_2 J_2 \tag{3.13a}$$

$$(\frac{\partial}{\partial t} + \frac{\overline{v}}{r}\frac{\partial}{\partial \lambda})\langle h* \rangle_{LT} = (\frac{\partial}{\partial t} + \frac{\overline{v}}{r}\frac{\partial}{\partial \lambda})(F(\gamma T_1 + (1-\gamma)T_2)), \tag{3.13b}$$

where b_1 and b_2 describes the reduction of boundary layer MSE by convection J_1 and J_2. F is a constant factor relating the change in lower-troposphere saturation MSE proportionally to the change in lower-troposphere temperature, and γ describes the relative influence of the two modes on the temperature of the lower troposphere.

With some manipulations of Eqs.(3.6c), (3.11), (3.13b) and (3.13), the quasi-equilibrium lower-tropospheric heating L_{eq} can be expressed as

$$L_{eq} = \frac{\mathcal{A} L_0 r_q}{B} q - \frac{F\gamma c_1^2}{B}(\nabla_H \cdot u_1 - \frac{\varepsilon}{c_1^2} T_1) - \frac{F(1-\gamma)c_2^2}{B}(\nabla_H \cdot u_2 - \frac{\varepsilon}{c_2^2} T_2), \tag{3.14}$$

where $\mathcal{A} = (b_2 - b_1) + F(1-2\gamma)$, and $B = F + (b_1 + b_2) - \mathcal{A} r_0$.

Table 3.1: Description of parameters used in the convective parameterization

Parameters	Normative values	Description
a_1, a_2	1.4, 0.0	Increase in q tendency per unit vertical velocity by advection
d_1, d_2	1.1, -1.0	Decrease in q tendency per unit heating J_1 and J_2
r_0	1.0	Background mean U/L ratio
r_q	1.0 K^{-1}	Linear dependence of U/L ratio on moisture anomaly
b_1, b_2	1.0, 2.0	Tendency for reduction in boundary layer moist static energy per unit heating J_1 and J_2
F	4	Ratio between saturated MSE and temperature in the lower-tropospheric "non-entraining" convection region
γ	0.5	Relative contribution of the first mode temperatures to the lower-tropospheric temperature anomaly
τ_L	30.0 min	Adjustment time to approach QE over the lower troposphere
c_1, c_2	(50.0, 25.0) m/s	Dry gravity wave speeds for the first and second modes
ε	0 day^{-1}	Temperature anomaly damping coefficient

3.2.3 Eigenfrequency formulation

We have formulated a linear system of convectively coupled barotropic vortices. The system is then Fourier transformed into azimuthal wavenumber-frequency space,

$$(u_j, v_j, T_j, L, q) = \sum_n (\tilde{u}_{j,n}(r), \tilde{v}_{j,n}(r), \tilde{T}_{j,n}(r), \tilde{L}_n(r), \tilde{q}_n(r))(\exp(i(n\lambda - \omega t)) + c.c), \quad j = 1, 2 \tag{3.15}$$

Substituting the expansion forms into the linearized momentum equations 3.6(a) and (b) yields

$$(-i\omega + in\overline{\Omega})\tilde{u}_{n,j}(r) - \overline{\xi}\tilde{v}_{n,j}(r) = \frac{\partial \tilde{T}_{n,j}(r)}{\partial r} \tag{3.16a}$$

$$(-i\omega + in\overline{\Omega})\tilde{v}_{n,j}(r) + \overline{\eta}\tilde{u}_{n,j}(r) = i\frac{n}{r}\tilde{T}_{n,j}(r). \tag{3.16b}$$

The perturbation temperature equations with convective heating become

$$(-i\omega + in\overline{\Omega})\tilde{T}_{n,1}(r) = c_1^2(\frac{1}{r}\frac{\partial}{\partial r}(r\tilde{u}_{n,1}(r)) + i\frac{n}{r}\tilde{v}_{n,1}(r)) + ((1+r_0)\tilde{L}_n(r) + L_0 r_q \tilde{q}_n(r)) \quad (3.17a)$$

$$(-i\omega + in\overline{\Omega})\tilde{T}_{n,2}(r) = c_2^2(\frac{1}{r}\frac{\partial}{\partial r}(r\tilde{u}_{n,2}(r)) + i\frac{n}{r}\tilde{v}_{n,2}(r)) + ((1-r_0)\tilde{L}_n(r) - L_0 r_q \tilde{q}_n(r)), \quad (3.17b)$$

and the prognostic equations for q and L become

$$\begin{aligned}(-i\omega + in\overline{\Omega})\tilde{q}_n(r) = &- a_1 c_1^2(\frac{1}{r}\frac{\partial}{\partial r}(r\tilde{u}_{n,1}(r)) + i\frac{n}{r}\tilde{v}_{n,1}(r)) - a_2 c_2^2(\frac{1}{r}\frac{\partial}{\partial r}(r\tilde{u}_{n,2}(r)) + i\frac{n}{r}\tilde{v}_{n,2}(r)) \\ &- d_1((1+r_0)\tilde{L}_n(r) + L_0 r_q \tilde{q}_n(r)) - d_2((1-r_0)\tilde{L}_n(r) - L_0 r_q \tilde{q}_n(r)) \quad (3.18)\end{aligned}$$

$$\begin{aligned}(-i\omega + in\overline{\Omega})\tilde{L}_n(r) = &- \frac{F\gamma}{B\tau_L}(c_1^2(\frac{1}{r}\frac{\partial}{\partial r}(r\tilde{u}_{n,1}(r) + i\frac{n}{r}\tilde{v}_{n,1}(r)) - \varepsilon\tilde{T}_{n,1}(r))) \\ &- \frac{F(1-\gamma)}{B\tau_L}(c_2^2(\frac{1}{r}\frac{\partial}{\partial r}(r\tilde{u}_{n,2}(r) + i\frac{n}{r}\tilde{v}_{n,2}(r)) - \varepsilon\tilde{T}_{n,2}(r))) \\ &+ \frac{AL_0 r_q}{B\tau_L}\tilde{q}_n(r) - \frac{1}{\tau_L}\tilde{L}_n(r) \quad (3.19)\end{aligned}$$

The above equations formulate a standard eigenvalue problem which is solved on a radially discretized domain. We have chosen the domain size to be 2,000 km along the radius with a 1km resolution so that there are no convective activities near the boundary, and we can apply an outgoing radiating boundary condition at the outer boundary. For more details of the discretization along the radius, please refer to Appendix A. The resulting complex frequency eigenvalues ω can be separated into the real part, which gives the modal frequency, and the imaginary part, which gives the modal

growth or decay rate. The corresponding eigenvectors provide the modal structure of the prognostic fields (u_j, v_j, T_j, q and L).

3.3 Results

3.3.1 Background mean vortex and convective heating

In this section, we will present the background vortex structure around which the instability is analyzed, and the background heating structure that will be incorporated in the convectively coupled model.

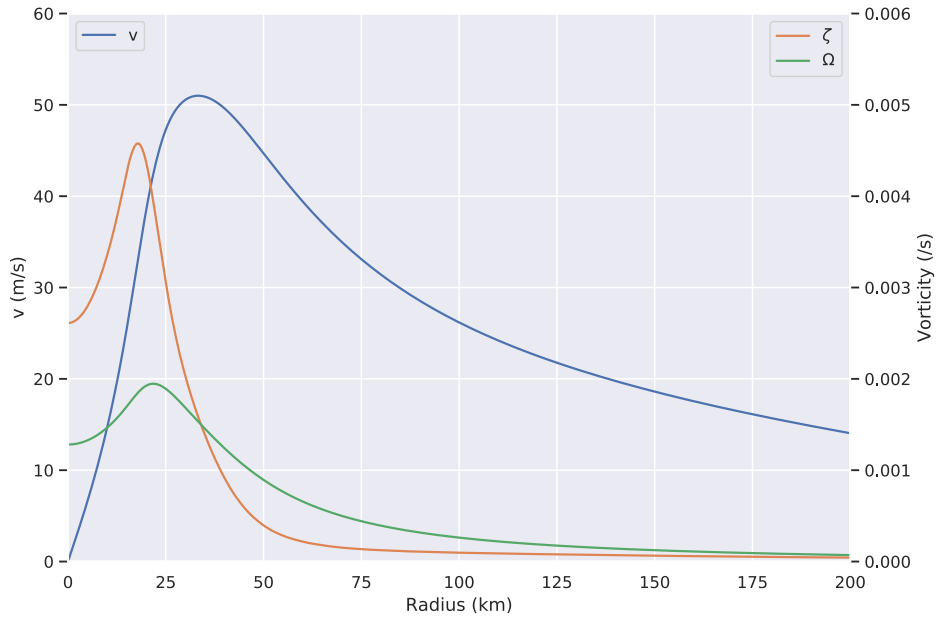

Figure 3.1: Ensemble-averaged time-averaged (48h-144h) height-averaged azimuthal mean structure of tangential wind speed (m/s), angular vorticity (/s) and absolute vorticity (/s)

We obtained the background vortex by averaging the azimuthal velocity vertically and azimuthally

over time from the 3rd day to the 10th day and over the ten ensemble members of the WRF simulations. Figure 3.1 shows the mean tangential velocity (m/s), the mean angular velocity (/s), and the mean absolute vorticity (/s) along the radius. The tangential velocity peaks around 30km where the eyewall is located, and the absolute vorticity peaks a little inward at about 20km. The non-monotonic structure of the absolute vorticity satisfies the necessary condition for barotropic instability, but it does not guarantee that the barotropic instability will be the dominant instability mechanism. The strong vorticity and its gradient at inner radii also provide a favorable background state for the mixed vortex-Rossby-inertia-gravity type of instability to occur.

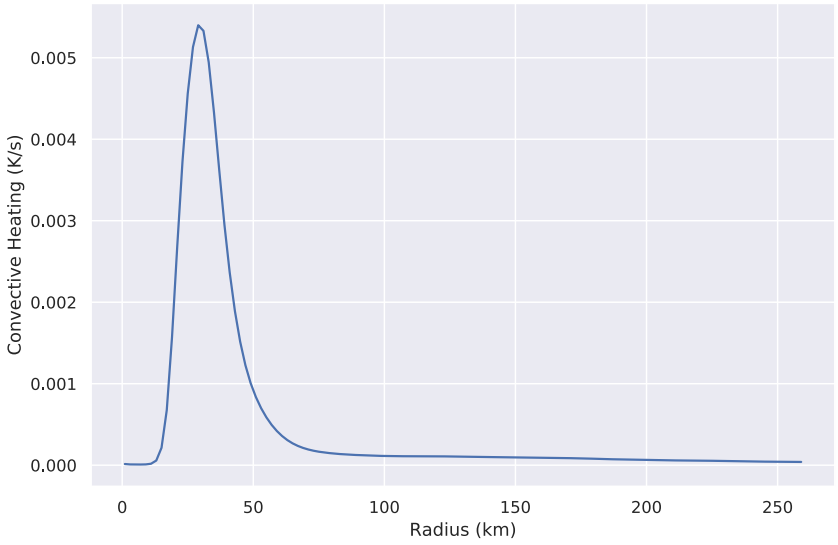

Figure 3.2: Convective heating (K/s) structure derived from ensemble-averaged time-averaged (48h-144h) azimuthal mean precipitation rate.

Figure 3.2 shows the mean convective heating (L_o) structure for the convectively coupled model. The heating is derived from the ensemble-averaged, time-averaged azimuthal mean precipitation

rate. The reason why we are not using azimuthally and vertically averaged convective heating directly is because the mean convective heating becomes negative in the regions with subsidence mainly due to the evaporation and sublimation of precipitable water transported into the area by the outflow and the mean convective heating cannot represent the strength of local convections. Therefore, we use the precipitation rate to represent the local strength of convection and derive the equivalent convective heating, L_o.

3.3.2 Instability with no coupled convection

Before we incorporate the convective coupling into the eigenfrequency framework, we are going to discuss the results based on the dry model first to see if there are any instabilities embedded in the dry dynamics. Figure 3.3 shows the growth rates and the propagating speeds of the unstable modes at each azimuthal wavenumber. The position of the dots indicates the azimuthal wavenumber and the propagating speeds of the unstable modes, while the size of the dots represents their growth rates. The mode with the largest growth rate can grow as fast as five-fold per day, even without convective coupling. It has an azimuthal wavenumber-two structure and propagates at about 50 m/s at the eyewall, which is consistent with the fast propagating wave we found in the WRF simulations but propagates slightly faster.

Figure 3.4 shows the horizontal structure of the temperature, divergence, and vorticity of the most unstable mode. The vorticity perturbation is mostly confined within 30km where the strong background vorticity gradient is located, and it is in phase with the perturbation temperature (or pressure), which indicates that the most unstable mode behaves like a vortex Rossby wave in the

inner vortex region. Outside the center vortex, the temperature (or pressure) perturbation is no longer in phase with the vorticity perturbation but is quadratic to the divergency perturbation. A positive temperature anomaly follows a divergent anomaly, which is consistent with the feature of an inertia gravity wave. Therefore, the horizontal structure of this most unstable mode is consistent with the mixed vortex-Rossby-inertia-gravity wave in which the vortex-Rossby wave in the inner vortex resonates with the gravity wave outside.

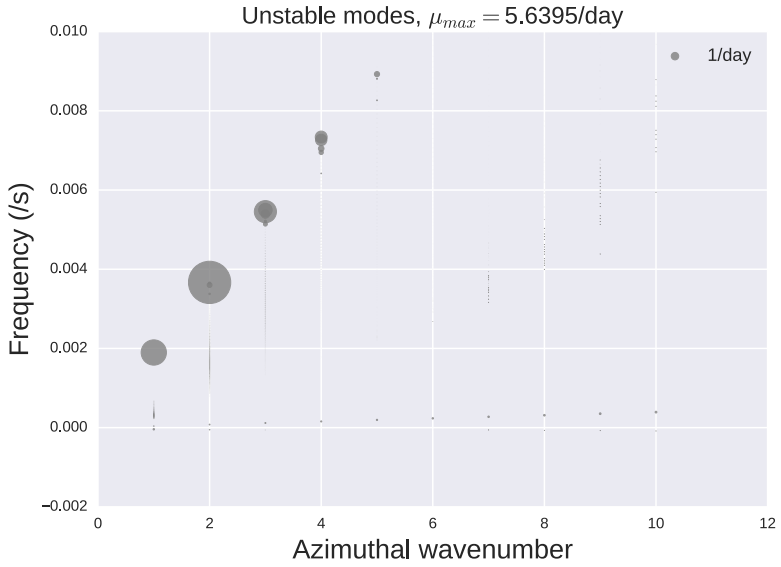

Figure 3.3: Propagating speeds and growth rates of the unstable modes from the dry eigenfrequency model. The size of the dots indicate the strength of the growth rates.

3.3.3 Convectively coupled experiments

Now we are going to examine the results from the convectively coupled model. The first experiment is the control case, in which the parameter values are chosen from Kuang [2008a] and Andersen &

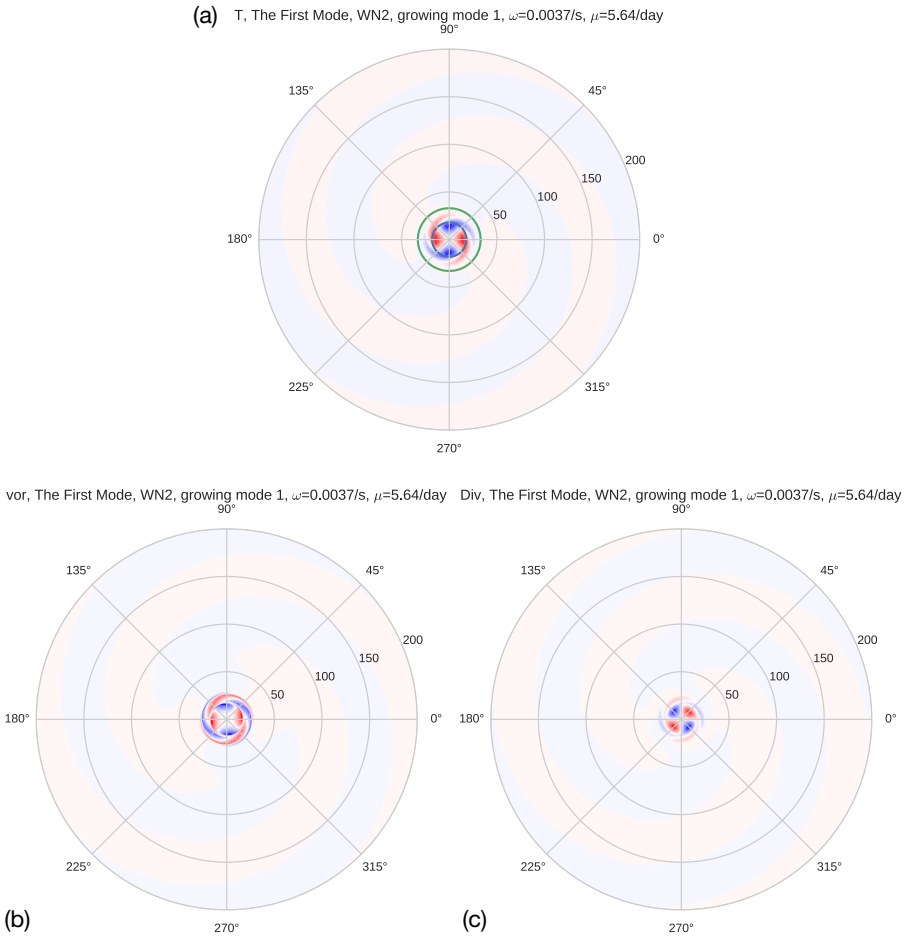

Figure 3.4: The horizontal structure of the most unstable mode from the dry eigenfrequency model in (a) temperature, (b) vorticity and (c) divergency.

Kuang [2008] and are summarized in Table 3.1. The key parameters will be briefly described here. First, the background U/L ratio, r_0, is set to 1 in the control case, meaning that the anomalous heating has the same strength in the upper- and lower-troposphere without mid-tropospheric moisture anomaly. In addition, r_q, which represents the dependence of the shape of convective heating on the mid-tropospheric moisture, is set to 1.0 K^{-1} so that it captures the effect of a more top-heavy convective heating profile due to a moist anomaly in the mid-troposphere. Then, γ is set to 0.5, assuming that the boundary layer MSE is in quasi-equilibrium with the lower-tropospheric temperature anomaly. Lastly, b_1 is set to 1 to represent the cooling of the sub-cloud layer due to the precipitation from a positive deep convection anomaly.

Figure 3.5 presents the growth rates and the propagating speeds of the unstable modes of the convectively coupled experiment with the normative values of the parameters. We notice that the growth rates of the fast-propagating branch are weakened with the convective coupling. We suspect the reason being that the first mode convective heating weakens the equivalent background stratification and both the barotropic instability and the mixed vortex-Rossby-inertia-gravity instability decreases with weaker stratification. In addition to the instability of the fast-propagating branch, the convective coupling leads to a set of unstable modes that propagate much slower than the background rotation rate. Its dispersion relationship is consistent with a retro-propagating inertia gravity wave with a radial wavelength of about 100 km. Therefore we consider these unstable modes as convectively coupled inertia gravity waves.

The horizontal and vertical temperature and heating structures of the most unstable convectively coupled gravity wave with azimuthal wavenumber two is shown in Figure 3.6, and the vertical struc-

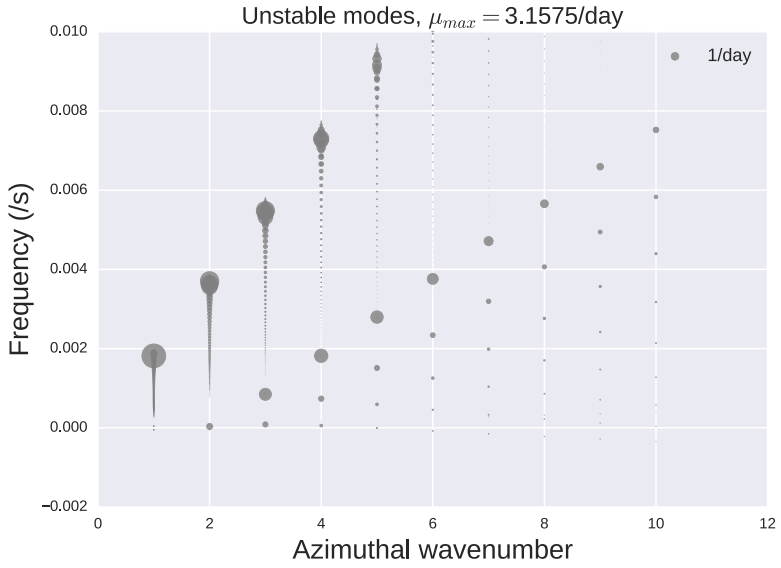

Figure 3.5: Propagating speeds and growth rates of the unstable modes from the convectively-coupled eigenfrequency model with normative parameters. The size of the dots indicate the strength of the growth rates.

ture is plotted at the radius of 30km. The intense heating perturbations (especially the second baroclinic mode) are confined around 30km, where the background heating L_o peaks. From the vertical structures at 30km, we can see that the second baroclinic temperature and heating structures are slightly in phase, which is where the instability lies and is consistent with the moist-stratiform instability mechanism [Kuang, 2008a].

Although the convectively coupled experiment can produce instability for the retro-propagating gravity waves, the features of the convectively coupled unstable modes are still different in many ways from the slow-propagating signal that we see in the WRF simulations. First, the slow-propagating signal from WRF is nearly stationary; therefore, it is much slower than the unstable modes from the simple model. Second, in the WRF simulations, the temperature perturbation has a second peak

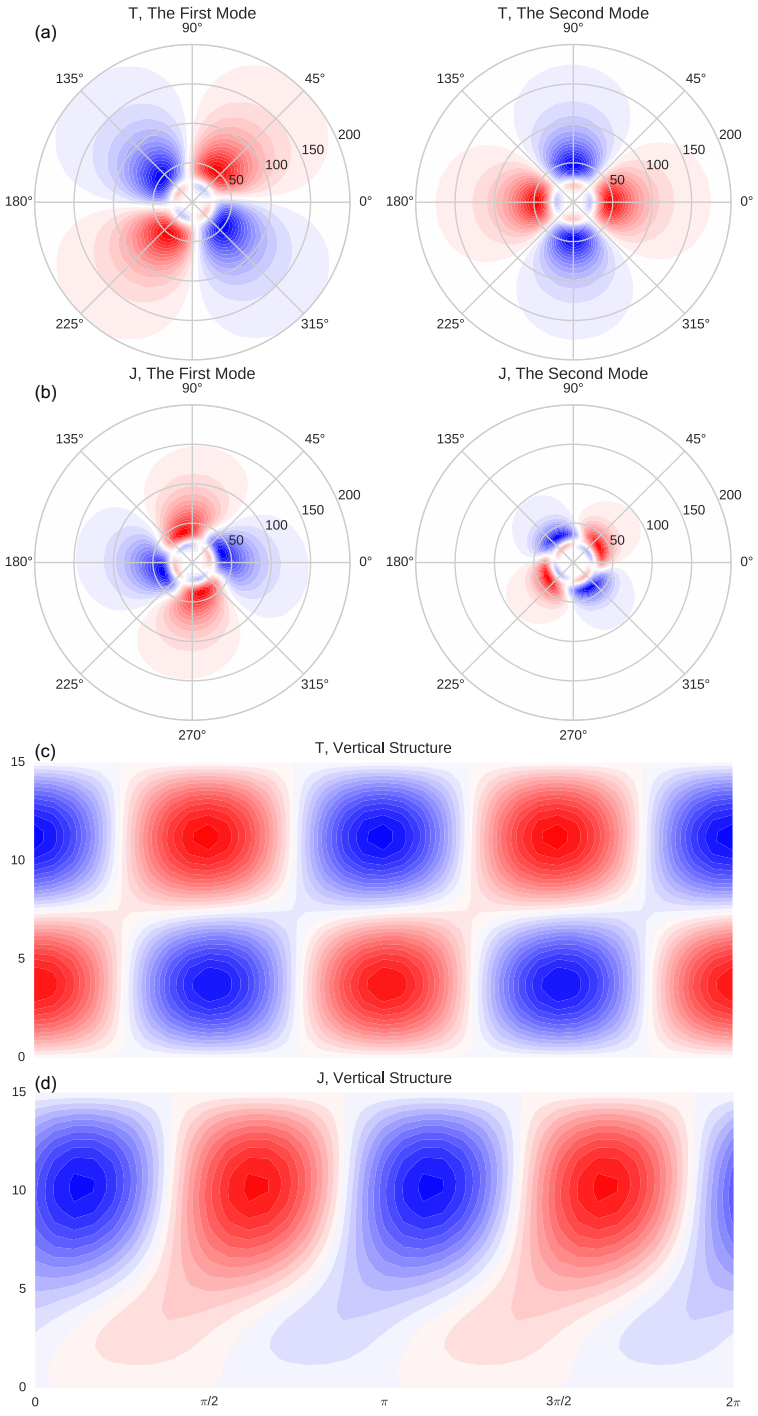

Figure 3.6: Horizontal and vertical structure of the most unstable mode from the convectively coupled eigenfrequency model with normative parameters. (a) is the horizontal temperature structure; (b) is the horizontal heating structure; (c) is the vertical temperature structure and (d) is the vertical heating structure.

outside the eyewall, which is comparable in strength to that near the eyewall.

Considering the discrepancies between the control case and the signals from the WRF simulations, we then modify the parameters based on some simple physical intuitions to verify whether it can improve the results. The original parameters from Kuang [2008a] are estimated from the CSRM simulations in Kuang [2008b] whose reference state is the TOGA case, therefore the parameters may not be applicable in some regions of a hurricane, e.g., at the eyewall of a hurricane. Based on simple physical intuitions, we will modify the parameter choices at those regions and allow the parameters to vary along the radius. r_q is tuned to a very small value (0.0001 K^{-1}) in the inner vortex because the convection is dominated by nearly undiluted updrafts and the environment is already very moist that additional moist anomaly will not make much difference to the shape of the anomalous heating. For a similar reason, γ is increased to 1 at inner radii because nearly undiluted updrafts keep the boundary layer MSE in equilibrium with a deeper layer of the free troposphere. b_1 is also tweaked to a smaller value (0.5) at inner radii because the boundary layer there is very moist that the precipitation induced evaporation is not very effective in cooling the boundary layer.

With the set of modified parameters, Figure 3.7 shows the growth rates and the propagating speeds of the unstable modes from the convectively coupled model. With the modified parameters near the eyewall, the gravity wave branch propagates much slower than the control case. In Appendix C, we derived the analytical solutions of the moist-stratiform instability with a set of simplified parameters, and found that the growth rate is proportional to L_0 and r_q. With the modified parameters in this experiment, $L_0 r_q$ now peaks at a larger radius with inhibited r_q effect in the inner vortex, and therefore the local background rotation rate where $L_0 r_q$ peaks becomes slower. Figure

3.8 shows both the horizontal structure and the vertical structure of temperature and convective heating fields of the nearly stationary unstable mode with azimuthal wavenumber-2. The temperature and heating perturbations now have a stronger signal outside the eyewall and spiral structures. The vertical heating structure is dominated by the first baroclinic mode, while the temperature is dominated by the second baroclinic mode, which is consistent with the unstable convectively-coupled mode from Kuang [2008a]. Although the eigenfrequency model is able to produce instabilities with nearly stationary frequencies with the modified parameters, the gravity wave branch has larger growth rate at larger azimuthal wave-number, which is inconsistent with what is found in the WRF simulation, as the WRF simulations has the strongest slow-propagating signal at azimuthal wave-number one. We will leave it to Chapter 4 for further improvements of the convective parameters.

3.4 Conclusion

Asymmetries are an important feature in tropical cyclones, and the mechanisms that lead to asymmetries in tropical cyclones, such as spiral rainbands or the polygonal eyewall, have been studied extensively via simulations and observations. Some studies suggest that they are associated with vortex Rossby-waves [Schubert et al., 1999, Reasor et al., 2000, Kossin & Schubert, 2001, 2004, Kossin et al., 2002], or inertial gravity waves. In contrast, others suggest that they might be related to the instabilities of inertia-Gravity wave radiated from a Rossby-like wave in the vortex core [Ford, 1993, 1994a,b, Schecter & Montgomery, 2004, Menelaou et al., 2016]. However, the impact of convec-

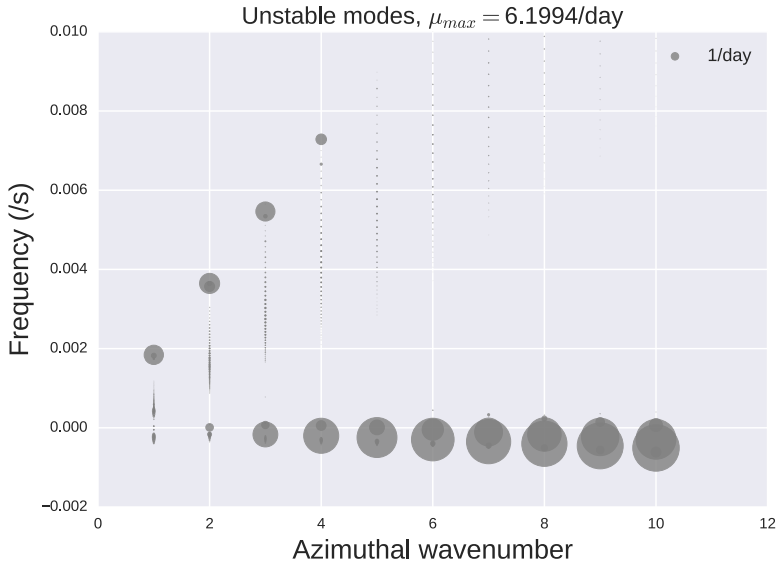

Figure 3.7: Propagating speeds and growth rates of the unstable modes from the convectively coupled eigenfrequency model with modified parameters based on simple physical intuitions. The size of the dots indicate the strength of the growth rates.

tion on the instability mechanisms of azimuthally asymmetric disturbances has not been extensively investigated.

Therefore, in this chapter, we investigated the linear instability of a TC-like vortex from the perspective of convectively coupled waves. We incorporated a simple two-mode convective parameterization [Kuang, 2008a] into the linearized primitive equations of a TC-like vortex [Schecter & Montgomery, 2004, Menelaou et al., 2016], and numerically solved for the eigenmodes and the eigenvalues of the linear system.

We found that with a realistic TC-like vortex structure diagnosed from the WRF simulations, a branch of fast propagating modes becomes unstable even without convective coupling. The instabilities are dominated by an azimuthal wavenumber-2 asymmetry, which is consistent with the

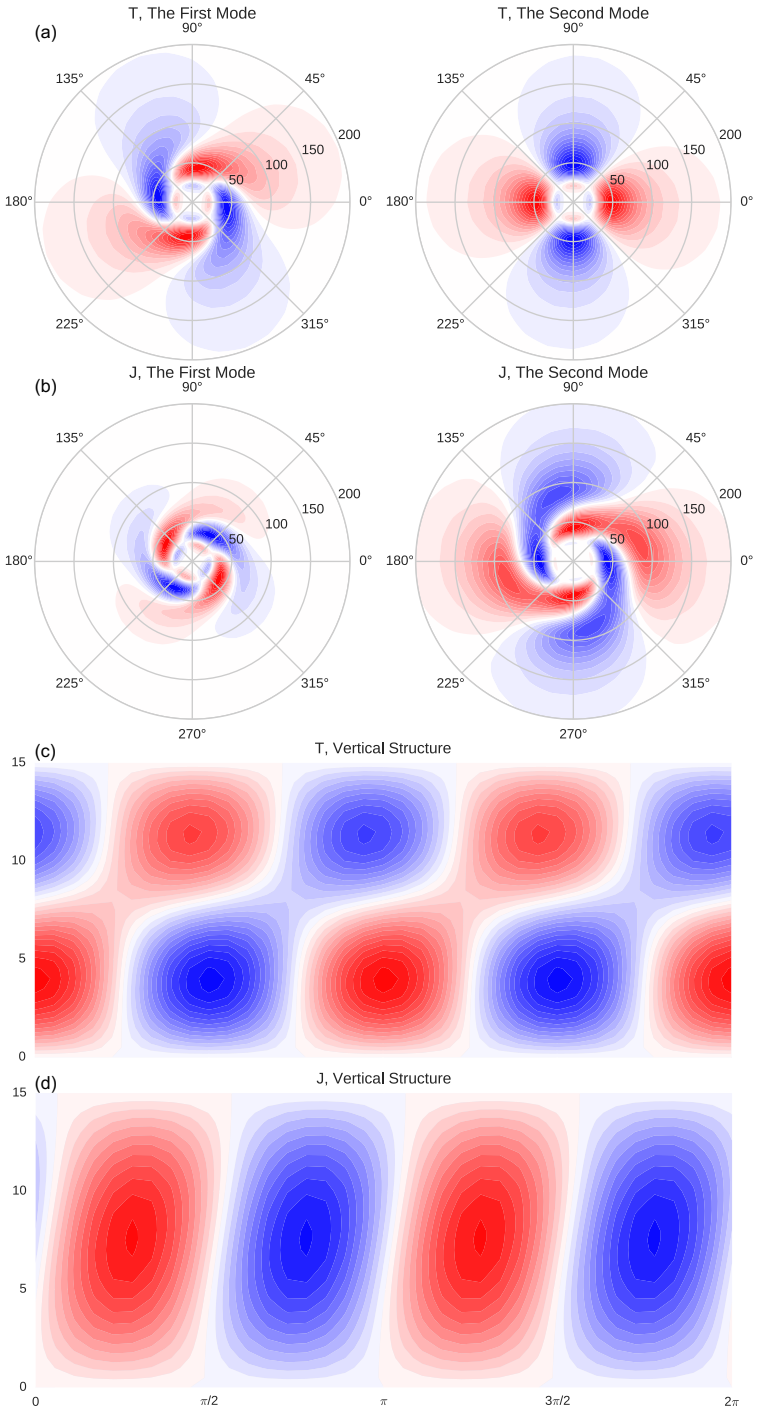

Figure 3.8: Horizontal and vertical structure of the most unstable mode from the convectively coupled eigenfrequency model with modified parameters based on simple physical intuitions. (a) is the horizontal temperature structure; (b) is the horizontal heating structure; (c) is the vertical temperature structure and (d) is the vertical heating structure.

WRF simulations. The structure of the most unstable mode shows a vortex-Rossby wave feature in the inner vortex but behaves more like a gravity wave at the outer region, which is similar to the structure of the fast propagating wave found in WRF simulations. Such a structure suggests that the instability is associated with a vortex-Rossby wave radiating an outward propagating gravity wave.

With convective coupling, strong instabilities can arise from the convectively coupled dynamics, while the instabilities of the fast propagating branch are reduced. The unstable modes from the convectively coupled dynamics have much slower propagating speeds than their background rotation rates. They are therefore considered convectively coupled gravity waves propagating against the background vortex.

Based on simple physical reasonings, we then modified some of the parameters in the convective parameterization. The convectively coupled unstable modes are now nearly stationary, whose frequencies are similar to those of the slow propagating wave from the WRF simulations. However, it still fails to produce greater growth rate at lower azimuthal wave-numbers. On the other hand, modifying the parameters based on physical intuitions lacks a solid foundation and the quantitative accuracy for estimating the parameters, though it is a useful first step to take. Therefore, we are going to estimate the parameters more systematically using the framework developed by Kuang [2018] and revisit the convectively coupled instability in Chapter 4.

Although the simple model cannot replicate the feature of the slow-propagating branch in the WRF simulations perfectly, the results suggest the importance of convective coupling in generating unstable modes in TC-like vortices and encourages future studies to explore more from the convectively coupled perspective.

To summarize, we developed a convectively coupled eigenfrequency framework to study the instability mechanisms of asymmetries in tropical cyclones. The model indicates a possible instability mechanism of convective coupled instability. We examined one background vortex structure and tested several sets of convective parameters, and this framework can be easily applied to a different background vortex and a different set of parameters in the future. One of the limitations of the current model is that it assumes the background vortex to be barotropic, but the background vortex usually weakens with height. The effect of the sheared background vortex is not studied in this chapter but will be a potential future direction to be explored. Another limitation is that the model does not account for the background secondary circulation. However, the momentum and energy transport by the secondary circulation may be critical in regions such as the boundary layer or the eyewall.

4

From linear response functions to a simple model of convective parameterization

4.1 Introduction

In Chapter 2, we identified the features of asymmetries near and outside the eyewall in an ensemble simulation of an idealized hurricane. We found that the slow-propagating asymmetries resemble

the structure of convectively coupled waves. Such findings encouraged us to explore the instabilities in TC-like vortices more from a convectively-coupled aspect. Therefore, we constructed an eigenfrequency model to study the convectively-coupled linear instability in TC-like vortices in Chapter 3. To represent the convective feedback in the eigenfrequency model, we used a two-mode simple convective parameterization developed by Kuang [2008a]. This two-mode model has been used to understand the basic instability mechanisms in convectively coupled gravity waves [Kuang, 2008a] and convectively coupled equatorial waves [Andersen & Kuang, 2008]. Like other simple models of convective parameterization [Khouider & Majda, 2006, Mapes, 2000], this two-mode model was initially invented to be conceptually simple and served the purpose of understanding the underlying instability mechanisms. The choice of keeping the first two baroclinic modes was made mainly for simplicity and interpretability, and the parameters are roughly estimated based on cloud-system-resolving model (CSRM) simulations of convectively coupled waves [Kuang, 2008b], whose reference state is from the Tropical Ocean Global Atmosphere Coupled Ocean-Atmosphere Response Experiment (TOGA COARE; Webster & Lukas [1992]). One limitation is that the construction of the simple model and its parameter choices can be highly dependent on the reference state, such as the temperature and moisture profiles and the large-scale forcing. The model construction and the parameters may vary from the RCE state to the TOGA state [Kuang, 2018], and could be even more different in a hurricane case; they may also vary from the eyewall of a hurricane to the far-field of a hurricane. Therefore, to gain quantitative accuracy with a simple convective parameterization, more complete models will be needed to guide us through the construction of simple models and their parameter choices.

Linear response functions constructed from limited-domain CSRMs are such a complete model that represents the macroscopic behavior of moist convection as a response to weak large-scale perturbations with more quantitative accuracy [Kuang, 2010]. They can be coupled with a linearized large-scale dynamic model to study the linear instability of moist convecting atmospheres or their responses to weak forcing. This approach was used to study convectively coupled waves [Kuang, 2010] and weakly forced mock Walker cells [Kuang, 2012]. However, a limitation of the models based on linear response functions is that the models are usually of too-high dimensionality to be analyzed and interpreted. In some situations, it may even become computationally infeasible to solve for the linear instability of a coupled system due to its large dimensions. In addition, unlike simple convective parameterization models, it can be challenging to interpret the results from high dimensional coupled models and develop physical intuitions of the instabilities from such models.

A sweet spot where the convective parameterization model has both the quantitative accuracy in representing the behavior of moist convection and the interpretability to understand the instability mechanisms is to use the relevant linear response functions as guidance to construct simple models of convective parameterization. Kuang [2018] presented such a procedure to systematically construct simple models and constrain their parameters from linear response functions through a modular order-reduction procedure from control theory. The simple models developed from this procedure and the physical intuitions derived from them, therefore, have a more solid foundation.

In this chapter, we constrain the parameter choices used in Chapter 3, based on the procedure developed by Kuang [2018]. We introduce the simulation setups in the CSRM, and the procedure used to construct the linear response functions in section 4.2. In section 4.3, we will discuss the ref-

erence mean states along the radius of the simulated hurricane, the linear response functions associated with them, and the linear stability results derived from the linear response functions. Section 4.4 will present the results from the reduced model through the modular order-reduction procedure. In section 4.5, we will make the connection between the reduced model and the two-mode simple parameterization model. Section 4.7 will highlight the main conclusions and limitations, and also discuss potential directions for future works.

4.2 Construction of the linear response functions from CSRMs

4.2.1 Model descriptions and configurations

All CSRM simulations are performed with the System for Atmospheric Modeling (SAM, Khairoutdinov & Randall [2003]), version 6.10.9. The model solves the anelastic equations of motion, and the prognostic thermodynamic variables include the liquid ice static energy, total nonprecipitating water, and total precipitating water. All experiments are performed over an ocean surface with a fixed sea surface temperature of 29°C. The horizontal domain size is 64km $\times$ 64km with a resolution of 2km. There are 46 vertical layers, extending from the surface to about 24km, which are consistent with the vertical grid of the WRF simulations. The top third of the domain is a wave-absorbing layer.

We used a single momentum bulk scheme to parameterize microphysics and a simple Smagorinsky-type scheme for subgrid-scale turbulence. Surface latent and sensible heat fluxes are calculated using a bulk aerodynamics formula with a constant surface wind speed to eliminate the wind-induced sur-

face heat exchange. For simplicity, instead of using an interactive long-wave radiation scheme, we applied a time-invariant radiative forcing diagnosed from the WRF simulations.

The initial soundings of temperature and moisture and the thermodynamical forcing are all diagnosed from the WRF simulations so that the reference states simulated by SAM stay close enough from those of the WRF simulations. The reference states and forcings will be discussed in more detail in section 4.3.1.

4.2.2 Construction of the linear response functions

We are going to follow the procedure described in Kuang [2010, 2012] to construct the linear response functions from doubly-periodic limited-domain CSRM experiments, and the key steps will be briefly described here.

The purpose of the convective parameterization is to build a relationship between the convective tendencies of temperature and moisture and its thermodynamic state, which includes the profiles of temperature and moisture. The relationship can be approximately represented by the linear response functions within the vicinity of a given reference state. To be more precise, we define the deviations of horizontally averaged profiles of temperature T and moisture q of the CSRM from a given reference state to be the state vector, denoted as $\vec{x}$, and we also denote the linear response functions as M. Therefore, the anomalous convective tendencies of temperature and moisture can be written as

$$(\frac{\mathrm{d}\vec{x}}{\mathrm{d}t})_{conv} = \mathrm{M}\vec{x}. \tag{4.1}$$

To construct the linear response functions M for a given reference state, we first run the CSRM to the desired steady reference state. At the reference state, the mean convective tendencies of temperature and moisture are in statistical equilibrium with the reference forcings. Then, we add a set of anomalous temperature or moisture forcing to the CSRM, one at a time. The perturbation forcing of temperature or moisture is time-invariant and horizontally homogeneous. It is added layer by layer, with an amplitude of 0.5 K/day for temperature or 0.2 g/kg/day for moisture. The magnitude of the forcing is verified to be large enough to perturb the mean state to a new equilibrium, but still small enough that it is within the linear regime. When each of the anomalous forcing $\vec{f_i}$ is introduced, the simulation will reach a new equilibrium state, which deviates from the reference state by $\vec{x_i}$. Under the new equilibrium state, the anomalous convective tendencies $\mathrm{d}\vec{x_i}/\mathrm{d}t$ are in balance with the prescribed perturbation forcing $\vec{f_i}$. If we denote the deviations from the reference state as X, which consists of column vectors $\vec{x_i}$, and further denote the full set of anomalous forcing as F, which consists of column vectors of each prescribed anomalous forcing $\vec{f_i}$, then the linear response matrix M at a given reference state can be estimated through a matrix inversion as

$$\mathrm{M} = -\mathrm{F}\mathrm{X}^{-1}. \tag{4.2}$$

Since there are uncertainties in calculating the departures from the reference state X, there will be uncertainties in the construction of M as well. The errors in the eigenvalues of M due to the uncertainties in X scale as $|\partial\lambda| \propto |\lambda||\partial\mathrm{X}||/||\mathrm{X}||$. This relationship implies that the fastest decaying eigenmodes of M are influenced the most by the uncertainties in X. It also shows that the relative

error in λ can be reduced by reducing the relative uncertainties in X. Therefore, to increase the accuracy in M, we then calculate the structure of the fast decaying modes and apply stronger forcing onto these modes so that the deviations from the reference state become significant compared to their uncertainties. The details of the refinement process are described in Appendix B.

4.3 Linear instability from linear response functions

4.3.1 Reference mean states

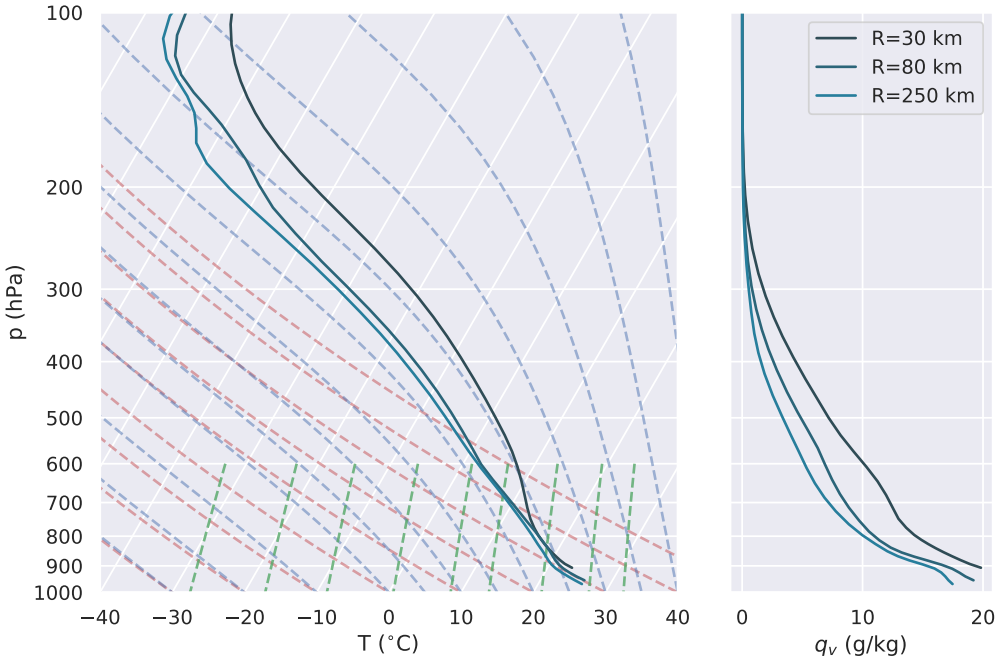

Figure 4.1: Ensemble-averaged time-averaged (48h-144h) azimuthal mean profile of (a) temperature (K) and (b) moisture (g/kg) at 30km, 80km and 260km from the WRF simulations.

We first define the mean states around which the linear response functions will be constructed.

To constrain parameters in the simple convective parameterization model for the eigenfrequency analysis, we are going to choose several representative reference states along the radius of the simulated hurricanes. According to the azimuthally averaged structure of vertical velocity shown in Figure 2.1(c), we will choose the azimuthally averaged states at 30km, 80km, and 260km as the reference states. 30km is located at the eyewall where deep convections and strong updrafts occur; 80km is right outside the eyewall where moderate subsidence dominates, while 260km is beyond the strong influence of the hurricane-scale circulation.

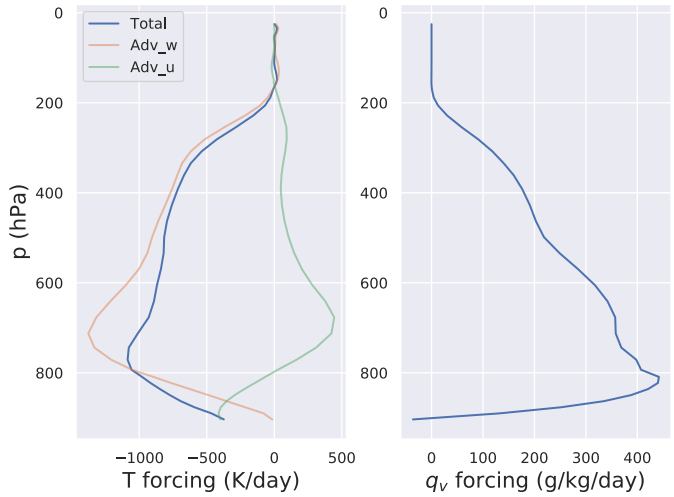

Figure 4.2: Ensemble-averaged time-averaged (48h-144h) large-scale forcing of (a) temperature (K/day) and (b) moisture (g/kg/day) at 30km from the WRF simulations.

Figure 4.1 shows the temperature and moisture profiles of the reference states at 30km, 80km, and 260km. The temperature profile at 30km stays close to a moist adiabatic curve, while going outward, the reference state becomes colder and drier. Figure 4.2 shows the large-scale forcing of temperature and moisture at 30km. There is a substantial large-scale cooling and moistening throughout

the column, which is mainly due to the strong updraft in the eyewall. The cooling and moistening forcing are then going to trigger deep convection in the CSRM. At 80km, the large-scale forcing (Figure 4.3) is mostly warming and drying throughout the column due to the subsidence. Convections are greatly inhibited under the warming and drying condition. In addition to the forcing of temperature and water vapor, it is critical to include the large-scale forcing of precipitating water (or ice), which is advected into the domain at about 200hPa by a layer of outflow. When the additional forcing of precipitating water sublimates and evaporates in the limited-domain CSRM, it cools and moistens the column and allows convection to happen occasionally. At 260km, both the temperature forcing and the moisture forcing (Figure 4.4) become weaker compared to those at inner radii. The forcing generally cools and moistens the column, and the radiative cooling becomes comparable to the advective cooling.

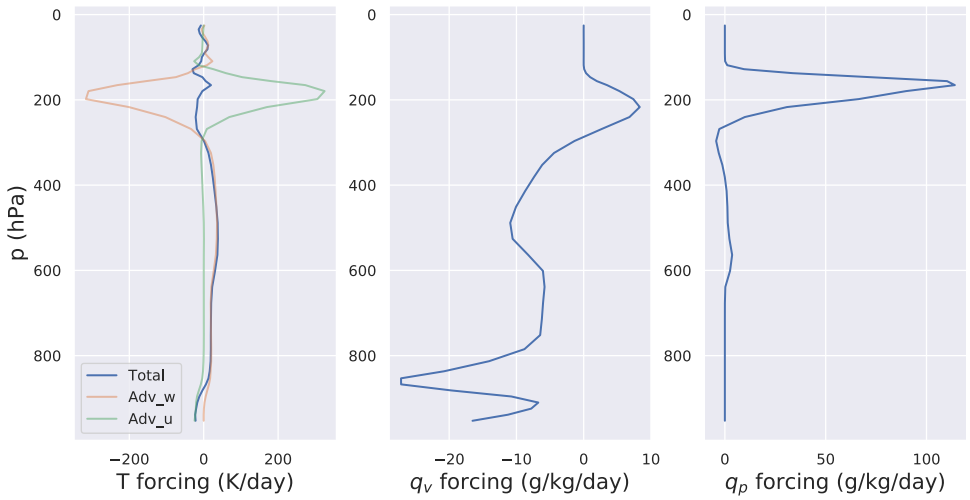

Figure 4.3: Ensemble-averaged time-averaged (48h-144h) large-scale forcing of (a) temperature (K/day), (b) moisture (g/kg/day) and (c) precipitable water (g/kg/day) at 80km from the WRF simulations.

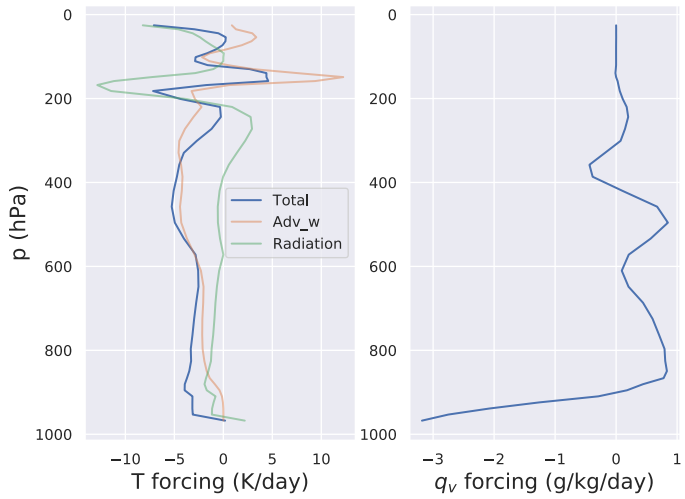

Figure 4.4: Ensemble-averaged time-averaged (48h-144h) large-scale forcing of (a) temperature (K/day) and (b) moisture (g/kg/day) at 260km from the WRF simulations.

4.3.2 Linear response functions

Following the procedure described in section 4.2.2, we constructed the linear response functions around the reference state at 30km, 80km, and 260km, respectively. In this section, we are going to highlight the key features of the linear response functions at different radii.

First, we are going to look at the linear response functions at 260km (Figure 4.5), as this radius is beyond the strong influence of the inner core circulation and convections. All tendencies are averaged over 2 hours. General features of the linear response functions at 260km resemble many of the critical features of the RCE case [Kuang, 2012], and will be briefly described here. A warm anomaly in the sub-cloud layer (below $\sim$ 850 hPa) leads to cooling locally and warming in the free troposphere. In contrast, a warm anomaly in the free troposphere leads to cooling at and above the

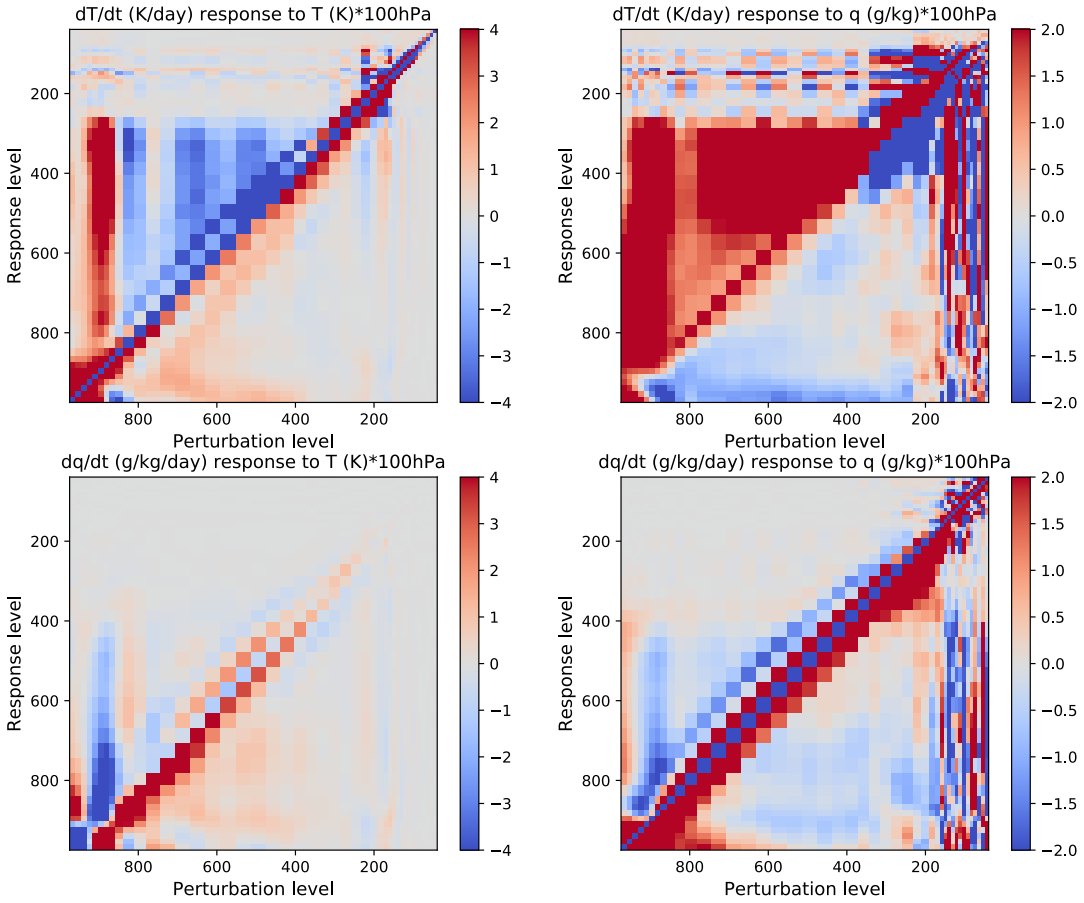

Figure 4.5: The four quadrants of the 2h-averaged linear response function for the 260km case. The horizontal axis is the pressure of the perturbed layer, and the vertical axis is the pressure of the responding layer. Each column of the matrices is normalized by the mass of the perturbed layer.

perturbed layer as it acts as a temperature barrier for convections. A warm anomaly in the lower sub-cloud layer facilitates overturning circulation in the sub-cloud layer and leads to moistening above and drying below, whereas a warm anomaly in the upper sub-cloud layer acts in the opposite way. A moist anomaly either in the sub-cloud layer or in the free troposphere generally leads to a warming above the perturbed layer and drying locally.

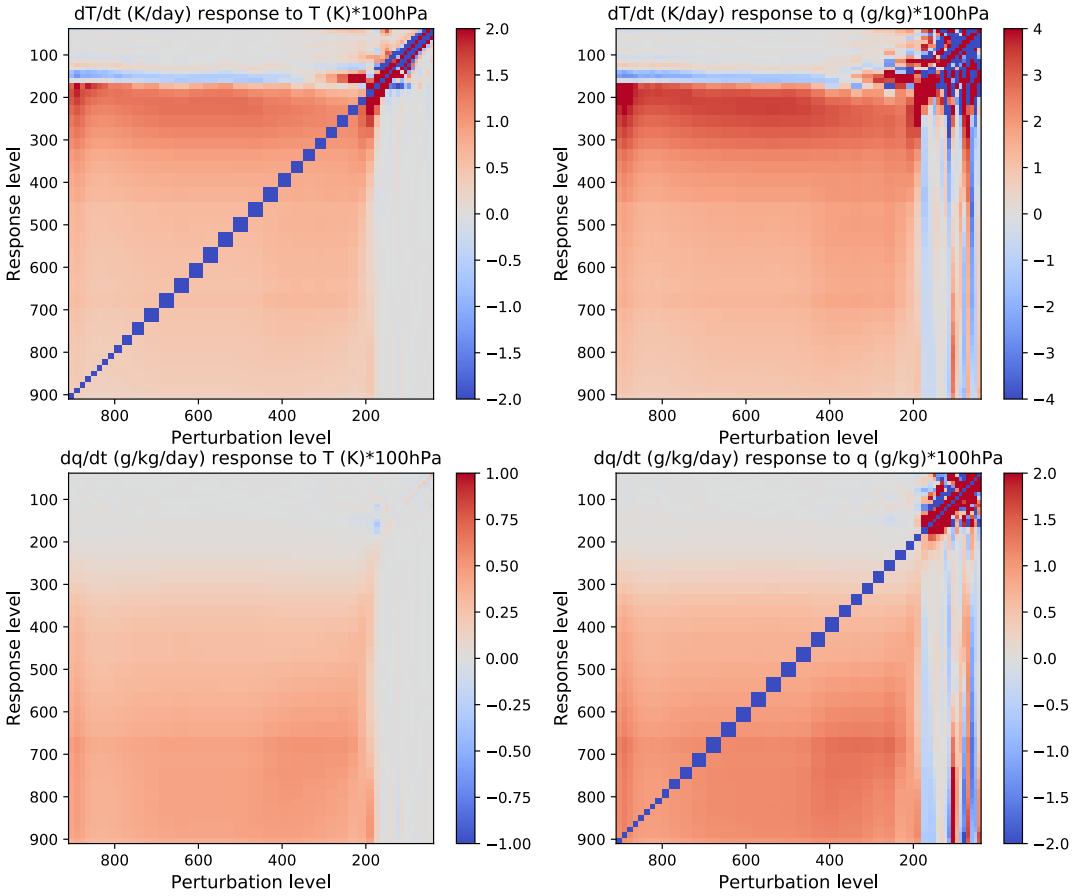

Figure 4.6: The four quadrants of the 2h-averaged linear response function for the 30km case. The horizontal axis is the pressure of the perturbed layer, and the vertical axis is the pressure of the responding layer. Each column of the matrices is normalized by the mass of the perturbed layer.

On the other hand, Figure 4.6 shows the linear response functions around the reference state at 30km, averaged over 2h as well. Its general features are very different from those of the RCE case or the 260km case. It shows that a warm or moist anomaly either in the sub-cloud layer or in the free troposphere leads to strong damping locally and warming and moistening anywhere else throughout the column. It indicates that any temperature or moisture deviation from the moist adiabatic profile will be quickly damped and redistributed throughout the whole column so that it reaches a new moist adiabatic profile. The linear response functions in the eyewall differ from the RCE case or the 260km case mainly because first, the eyewall is very moist so that the temperature and moisture profiles tend to stay close to the moist adiabatic profile; and second, the strong convection in the eyewall can efficiently redistribute energy throughout the whole column.

The linear response functions for the reference state at 80km averaged over 2 hours are presented in Figure 4.7. Qualitatively, it shows some features that are similar to the 260km case. A warm or moist anomaly in the sub-cloud layer leads to warming in the free troposphere; a warm anomaly in the free troposphere leads to cooling locally and above the perturbed layer. However, the magnitude of the response is much weaker, probably due to a stronger damping effect, which we will discuss in section 4.5. If we average the linear response functions for 30 minutes (not shown), then it will look much more similar to the 260km case.

4.3.3 Linear instability from the linear response functions

Before proceeding to the model order reduction to constrain the parameters of the simple convective parameterization, we are going to consider the linear instability of convectively coupled 2D gravity

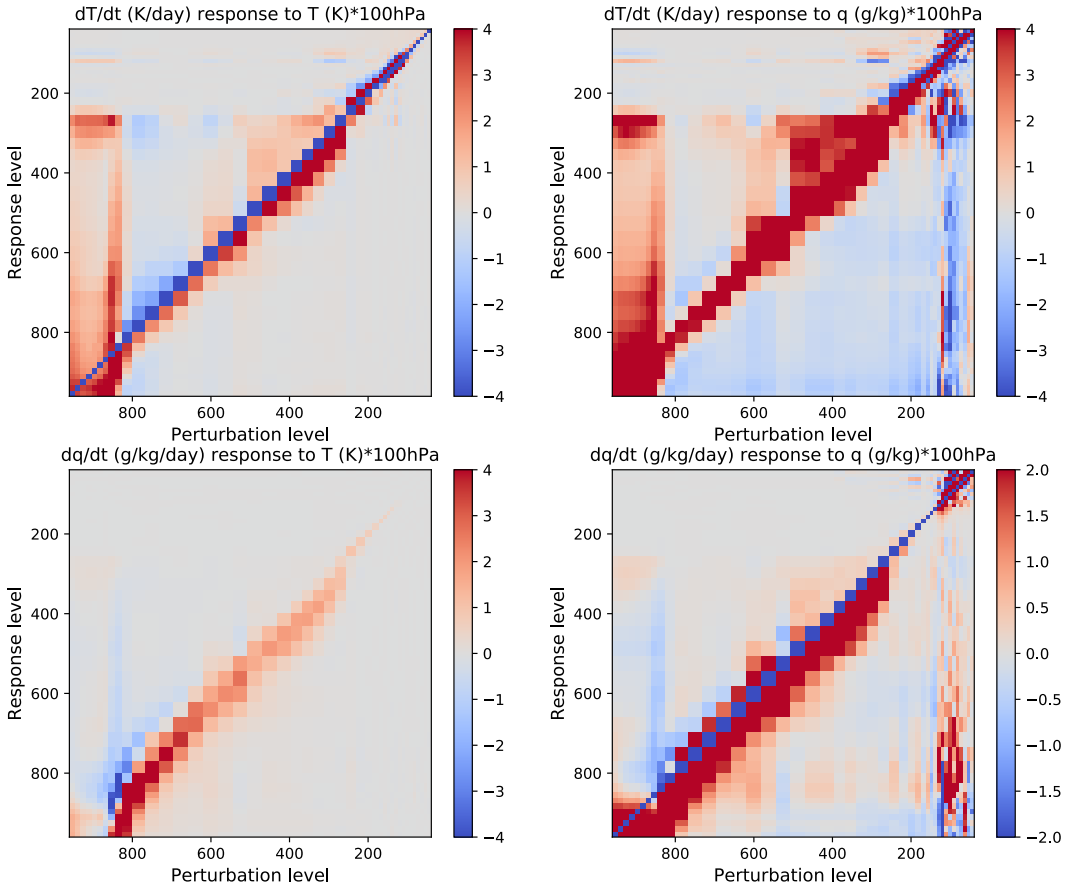

Figure 4.7: The four quadrants of the 2h-averaged linear response function for the 80km case. The horizontal axis is the pressure of the perturbed layer, and the vertical axis is the pressure of the responding layer. Each column of the matrices is normalized by the mass of the perturbed layer.

waves based on the linear response functions in this section. This simplified system captures the fundamental aspects of the coupling between convection and large-scale dynamics. It also sets a benchmark for us to evaluate the performance of model order reduction in section 4.4.

Similar to Kuang [2018], we consider a 2D linear gravity wave system that consists of a single horizontal wavenumber k and is discretized in height,

$$\frac{\mathrm{d}}{\mathrm{d}t}\begin{pmatrix}\vec{x}\\ \vec{w}\end{pmatrix} = \begin{pmatrix}\mathrm{M} & \mathrm{A}\\ k^2\mathrm{C} & \mathrm{D}\end{pmatrix}\begin{pmatrix}\vec{x}\\ \vec{w}\end{pmatrix}, \tag{4.3}$$

where $\vec{x}$ is the state vector that consists of temperature and moisture anomalies from their reference state; $\vec{w}$ is the vertical velocity anomaly; M is the linear response function; A describes the temperature and moisture tendencies due to vertical advection; k^2C relates the temperature and moisture anomalies and the vertical velocity through horizontal momentum equation, hydrostatic balance and continuity equation; and D represents the damping of vertical momentum which is treated as Rayleigh damping. For simplicity, the virtue effect in the large-scale wave dynamics is neglected, and a rigid lid ($w = 0$) is assumed at the model top.

Figure 4.8 shows the growth rates and phase speeds of the least stable modes for the 260km case from the full linear response functions in blue. Qualitatively, the propagating speeds and the growth rates resemble those of the RCE case. The least damped modes consist of two branches, an unstable propagating convectively-coupled wave branch with wavelengths of thousands of kilometers and phase speeds of 10 m/s to 20m/s, and a stationary branch which peaks at a wavelength

around 10,000 km. Since there is no active radiative feedback, the stationary branch is slightly decaying rather than growing [Kuang, 2018]. The azimuthal wavenumber-one structures of the most unstable mode at 260km are shown in Figure 4.9 on the left.

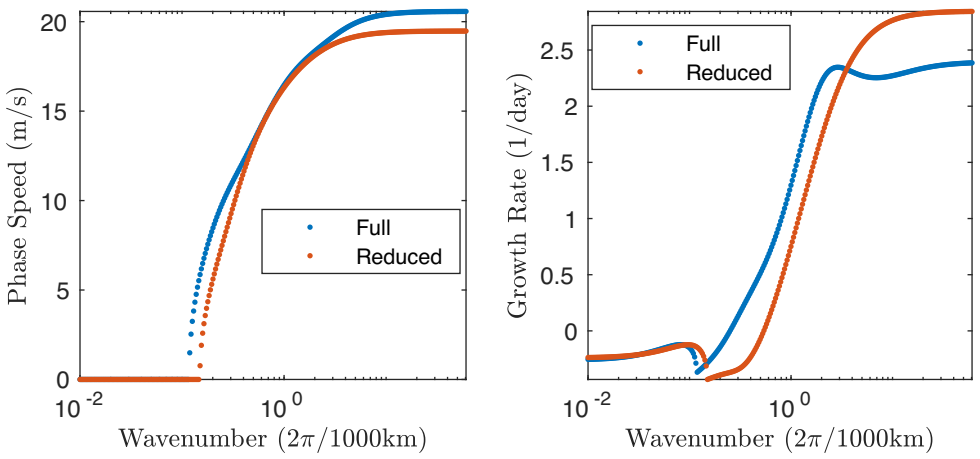

Figure 4.8: (right) Linear growth rates and (left) the phase speed of the least stable modes for the 260km case for the full model (blue) and the reduced sixth-order model (red).

The growth rates and the phase speeds of the least stable modes for the 80km case from the full model are shown in Figure 4.10 in blue. Similar to the 260km case, it has a stationary branch that is stable at large wavelengths (around 100,000 km to 10,000 km), and a propagating branch at smaller wavelengths (around 10,000 km to 500 km). However, the propagating branch is mostly decaying, and its growth rates are much weaker compared to the 260km case even when it becomes unstable. The azimuthal wavenumber-one structures of the least damped mode at 80km is shown in Figure 4.11 (the left panel). At very small wavelengths, the damping rates of the least damped modes are closely tied to the Rayleigh damping rate.

Figure 4.12 shows the growth rates and the phase speeds of the least stable modes for the 30km

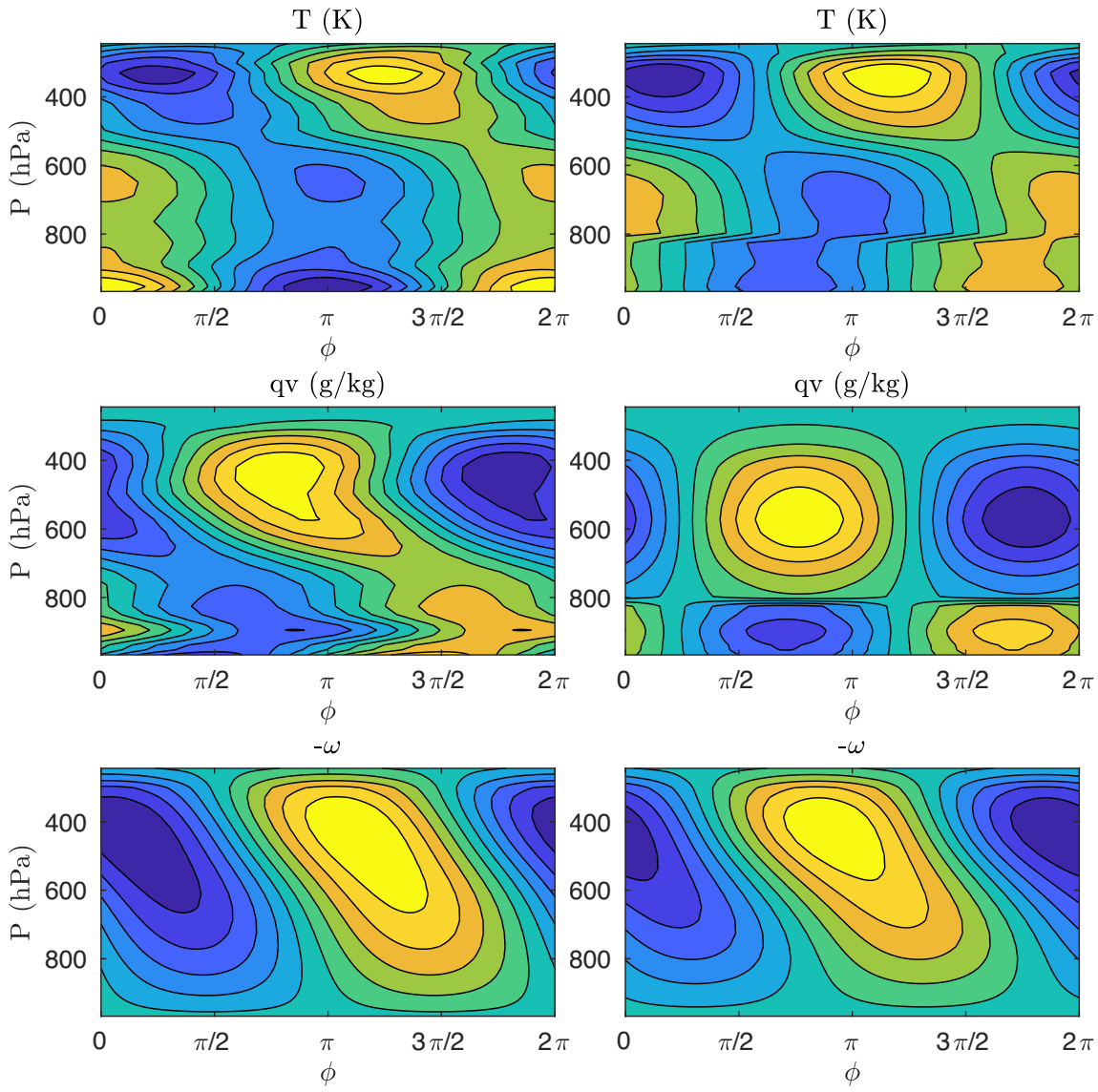

Figure 4.9: Temperature, specific humidity, pressure velocity and vertical velocity structures of the unstable propagating mode with azimuthal wavenumber one at 260km from the full model (left) and the reduced model (right).

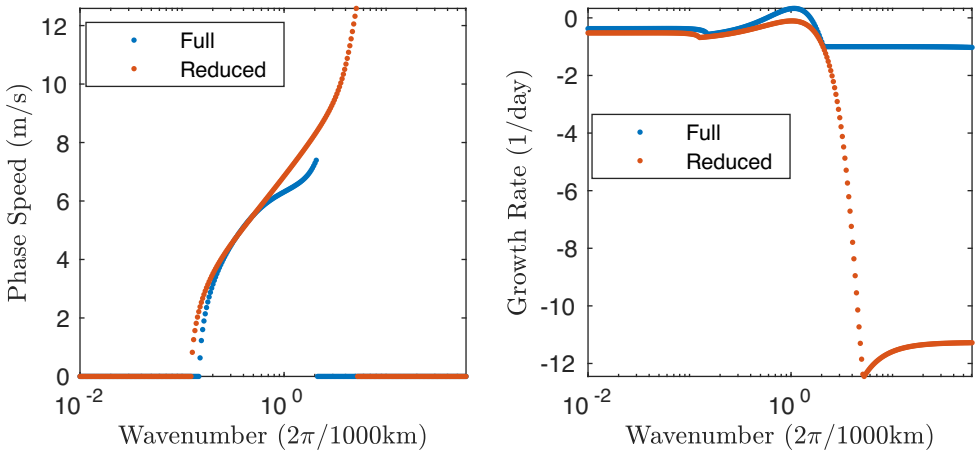

Figure 4.10: (right) Linear growth rates and (left) the phase speed of the least stable modes for the 80km case for the full model (blue) and the reduced sixth-order model (red).

case from the full model in blue. It has a stationary branch that is stable at large wavelengths and a propagating branch with very slow phase speeds and large growth rates at smaller wavelengths. As we increase the Rayleigh damping rate for momentum, this unstable branch becomes stable. We are going to discuss the instability more once we reduce the order of the system in the section 4.4.

4.4 Model order reduction

In this section, we reduce the dimension of the coupled model of 2-D gravity waves (Eq. 4.3) so that it is easier to interpret the instability mechanisms, and it connects to the two-mode convective parameterization more naturally. We are going to follow the procedure of model order reduction introduced in Kuang [2018], and the procedure is briefly described here.

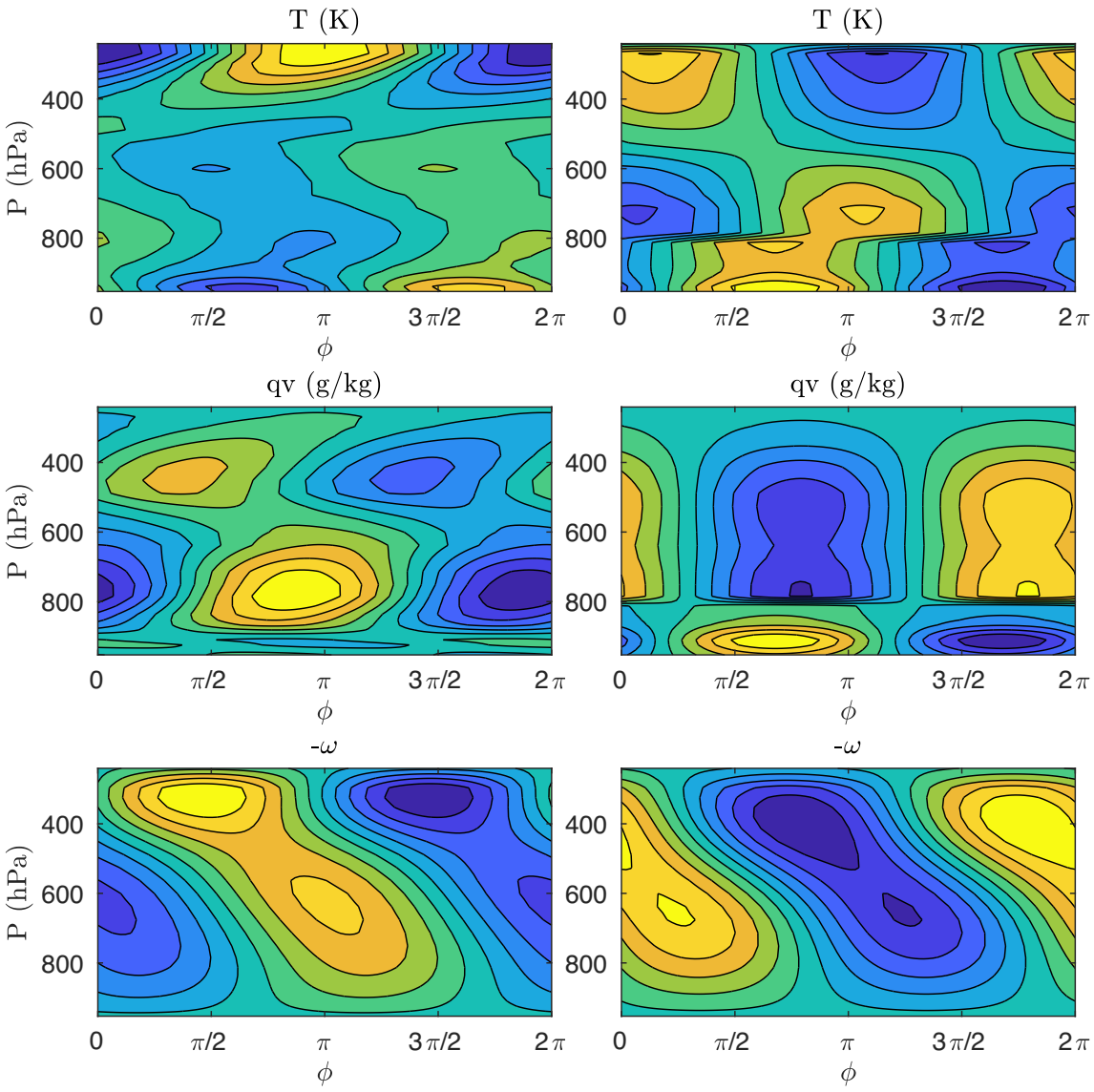

Figure 4.11: Temperature, specific humidity, pressure velocity and vertical velocity structures of the unstable propagating mode with azimuthal wavenumber one at 80km from the full model (left) and the reduced model (right).

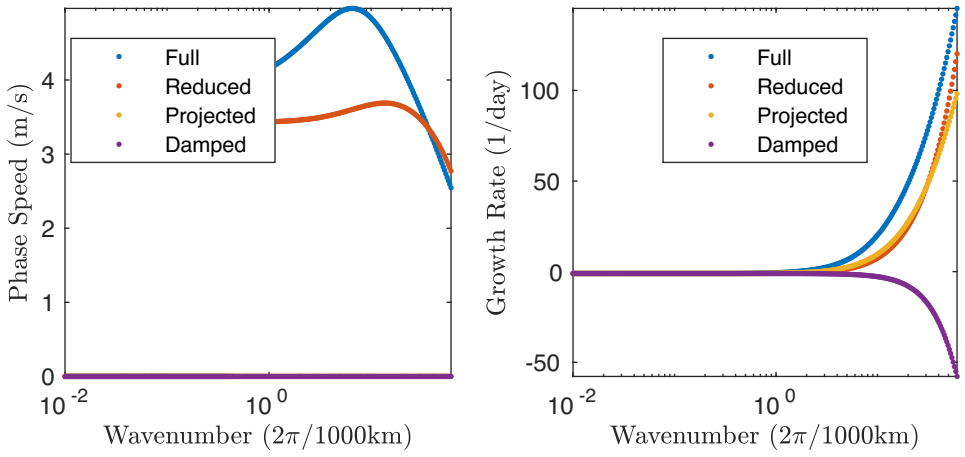

Figure 4.12: (right) Linear growth rates and (left) the phase speed of the least stable modes for the 30km case for the full model (blue) and the reduced sixth-order model (red).

In control theory, a standard linear dynamic system is usually written in the following form,

$$\begin{aligned} \frac{\mathrm{d}\vec{x}}{\mathrm{d}t} &= A\vec{x}(t) + B\vec{u}(t) \\ \vec{y} &= C\vec{x}(t) + D\vec{u}(t), \end{aligned} \tag{4.4}$$

where $\vec{u}$ is the input, $\vec{y}$ is the output, and $\vec{x}$ is the internal variable. Through model order reduction, the dimension of the internal state variable $\vec{x}$ will be reduced to a given order in a way that a measure of the output error is minimized. In particular, we used a balanced truncation algorithm to retain the states with the largest Hankel singular values [Moore, 1981, Safonov & Chiang, 1989].

Based on the model order reduction algorithm, we first define $\vec{x}$ on the right-hand side of Eq.(4.3) to be the input, $\mathrm{d}\vec{x}/\mathrm{d}t$ on the left-hand side to be the output and $\vec{w}$ to be the internal state variable, and reduce the order of $\vec{w}$ to 2 which is shown in Kuang [2018] to be sufficient and necessary to capture the instability mechanisms. After the order of $\vec{w}$ is reduced, we then consider the reduced $\tilde{\vec{w}}$ as

the input, $\mathrm{d}\tilde{\vec{w}}/\mathrm{d}t$ to be the output, and $\vec{x}$ to be the internal state variable, and reduce the order of the thermodynamic variable $\vec{x}$. For interpretability, the state vector $\vec{x}$ is reduced within the subspace that is spanned by the free tropospheric temperature, the free tropospheric moisture, and the boundary layer temperature and moisture. As in Kuang [2018], we choose to retain the first four modes of the thermodynamic state variable $\vec{x}$ so that the reduced model can still qualitatively reproduce the instability mechanisms from the full model and can also be easily interpreted. Once the full model, Eq.(4.3), is reduced to a six-order system which consists of four thermodynamic modes and two vertical velocity modes, the system is rotated and scaled so that the reduced model can be written as Eq.(3) in Kuang [2018],

$$\frac{\mathrm{d}}{\mathrm{d}t}\begin{pmatrix} T_1 \\ T_2 \\ q \\ h_b \\ w_1 \\ w_2 \end{pmatrix} = \left(\begin{array}{cccc|cc} & & & & -1 & 0 \\ & & \mathrm{M}^{4\times4} & & 0 & -1 \\ & & & & a_1 & a_2 \\ & & & & 0 & 0 \\ \hline k^2c_1^2 & 0 & 0 & 0 & -\varepsilon & 0 \\ 0 & k^2c_2^2 & 0 & 0 & 0 & -\varepsilon \end{array}\right)\begin{pmatrix} T_1 \\ T_2 \\ q \\ h_b \\ w_1 \\ w_2 \end{pmatrix}, \tag{4.5}$$

where T_1, T_2, q, h_b, w_1 and w_2 are the amplitudes of the four thermodynamic modes and the two vertical modes, $\mathrm{M}^{4\times4}$ is the reduced linear response function, c_1 and c_2 are the dry gravity wave speeds of the first- and second-mode, a_1 and a_2 represent the effect of vertical advection of the mid-tropospheric moisture by the two vertical velocity modes, and ε is the Rayleigh damping of the mo-

mentum. We should note that it is not always guaranteed that the reduced model will retain two free-tropospheric temperature modes, one moisture mode, and one boundary layer mode, as in Eq.(4.5). In most of the cases, these four modes happen to be the optimal modes to be retained, but there are also exceptions, and we will discuss how the exceptional cases are treated.

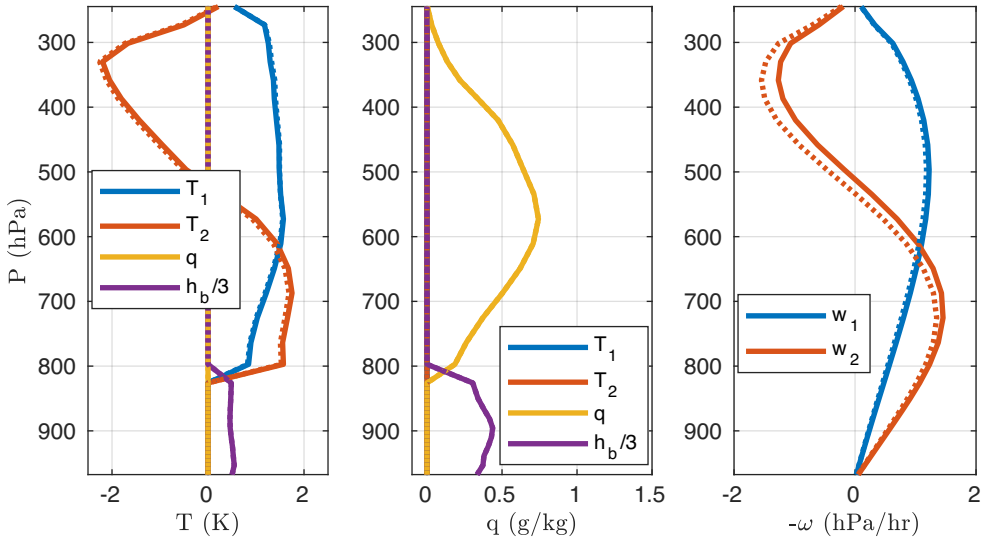

Figure 4.13: Basis functions used in the reduced sixth-order model for T_1, T_2, q, h_b, w_1 and w_2 for the 260km case.

Following the procedure described above, we reduced the order of the convectively-coupled model of 2-D gravity waves at 30km, 80km, and 260km, respectively. Figure 4.13 shows the vertical structures of the retained modes in terms of temperature, moisture, and vertical velocity for the 260km case. The retained thermodynamic modes include two free-tropospheric temperature mode, one free-tropospheric moisture mode, and one boundary layer mode. It justifies the choice of two baroclinic modes used in the simple convective parameterization model in Chapter 3. The phase speeds and the growth rates of the least stable modes from the reduced model are shown in

Figure 4.8 in red. The reduced model is able to reproduce the behavior of the least damped mode from the full model and captures the instability of the convectively coupled branch. The azimuthal wavenumber-one structures of the most unstable mode from the reduced model are shown in Figure 4.9 on the right. The reduced model reproduces the structures of both the vertical and horizontal velocities and the free-tropospheric temperature from the full model on the left. However, the moisture field is not well reproduced because only one moisture mode is retained. The boundary layer temperature and moisture are not well represented because they are not in phase from the full model.

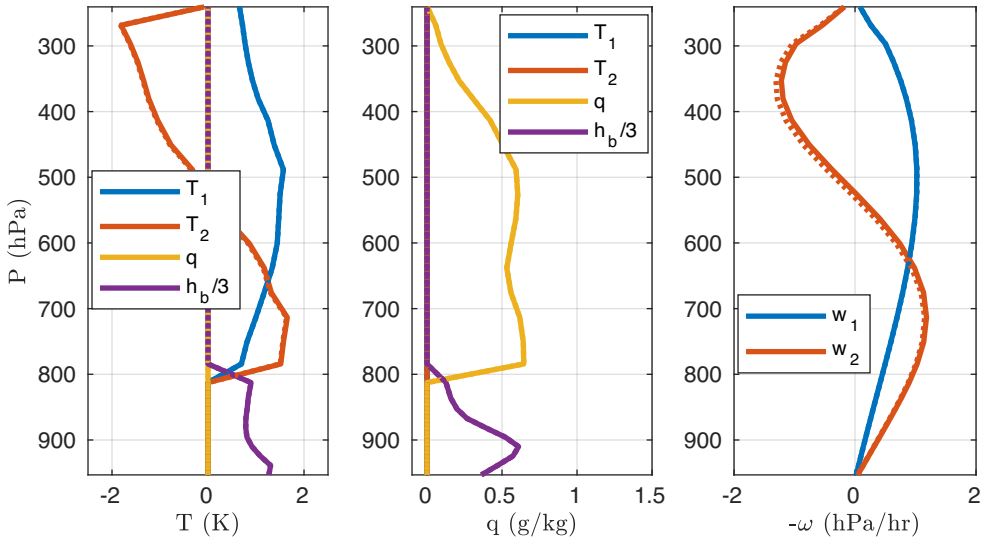

Figure 4.14: Basis functions used in the reduced sixth-order model for T_1, T_2, q, h_b, w_1 and w_2 for the 80km case.

Figure 4.14 represents the basis functions of the retained modes at 80km. It also retained two free-tropospheric temperature modes, one free-tropospheric moisture mode, and a boundary layer MSE mode. Qualitatively, the retained modes are similar to the modes retained for the 260km case.

It suggests that the same basis functions can be applied at different radii, and the behavior of the reduced models will not be sensitive to the slight modification in the basis functions. The phase speeds and the growth rates of the least stable modes from the reduced model are shown in Figure 4.10 in red. The behavior of the full model is well reproduced by the reduced model, except that the growth rates at very small wavelengths are not well resembled. This is because, at very small wavelengths, the structures of the least damped modes from the full model (not shown) have very high vertical wavenumbers that are not captured by the reduced modes. The azimuthal wavenumber-one structures of the least stable mode from the reduced model are shown in Figure 4.11 on the right.

At 30km, the four thermodynamic modes being retained are one free-tropospheric temperature mode, two free-tropospheric moisture modes, and one boundary layer MSE mode, which is different from the retained modes at the outer radius. The phase speeds and the growth rates of the least damped modes from the reduced model are shown in Figure 4.12 in red, which resembles the behavior of the full model. However, it is not ideal to have a different set of basis functions at 30km. In order to make the connection between the reduced model to the two-mode parameterization model and to have a fair comparison between the parameters at 30km and those at other radii, we then reduce the full model at 30km by projecting the full vertical structures of temperature, moisture, and vertical velocity onto a set of pre-calculated basis functions. The phase speeds and the growth rates of the least damped modes from the projected model are shown in Figure 4.12 in yellow. The modified reduced model can still reproduce the instabilities at small wavelengths, but cannot well represent the propagating speeds. If we increase the damping rate of the slowest-decaying eigenvector of $M^{4\times4}$, the unstable modes at small wavelengths will become stable (Figure 4.12 in purple). It

indicates that the instabilities are associated with the slowest-decaying mode of $M^{4\times4}$.

4.5 Bridge to the simple convective parameterization model

In this section, we are going to make the connection between the reduced model and the two-mode convective parameterization to estimate the parameters in the simple parameterization model and to better interpret the instabilities based on the derived parameters.

It is shown in Kuang [2018] that the convectively-coupled wave branch is not sensitive to the slowest-decaying eigenvector of $M^{4\times4}$. Therefore it is reasonable to further simplify the system by splitting the reduced model into two subspaces: a slow manifold along the direction of the slowest-decaying eigenvector of $M^{4\times4}$ and a fast manifold spanned by the remaining three eigenvectors. By design, the fast manifold and the slow manifold do not interact through convection. This will give us the following expression which is similar to Eq.(4) in Kuang [2018],

$$\frac{\mathrm{d}}{\mathrm{d}t}\begin{pmatrix} T_1^f \\ T_2^f \\ q^f \\ e^s \\ w_1 \\ w_2 \end{pmatrix} = \left(\begin{array}{cccc|cc} m_{11} & m_{12} & m_{13} & 0 & -1 & 0 \\ m_{21} & m_{22} & m_{23} & 0 & 0 & -1 \\ m_{31} & m_{32} & m_{33} & 0 & d_1^f & d_2^f \\ 0 & 0 & 0 & -\lambda^s & a_1^s & a_2^s \\ \hline (kc_1^f)^2 & 0 & 0 & k^2\varepsilon_1^s & -\varepsilon & 0 \\ 0 & (kc_2^f)^2 & 0 & k^2\varepsilon_2^s & 0 & -\varepsilon \end{array}\right)\begin{pmatrix} T_1^f \\ T_2^f \\ q^f \\ e^s \\ w_1 \\ w_2 \end{pmatrix}, \tag{4.6}$$

where T_1^f, T_2^f, and q^f are the amplitudes of the three independent modes of the fast subspace, e^s is

the amplitude of the slowest-decaying eigenvector,m_{ij} represents the convective response within the fast subspace, a_1^f and a_2^f are the vertical advection effect on q^f, c_1^f and c_2^f is the dry wave speeds for the adjusted modes, λ^s is the decay rate of the slowest-decaying eigenvector of $M^{4\times4}$, a_1^s and a_2^s are the effect of vertical advection by w_1 and w_2 on the slow mode, and $k^2\varepsilon_1^s$ and $k^2\varepsilon_2^s$ are the effects of the slow mode on the vertical velocities.

For ease of interpretation, the modes represented by T_1^f, T_2^f and q^f are designed in the following forms,

$$\begin{pmatrix} 1 \\ 0 \\ 0 \\ -h_{T_1} \end{pmatrix}, \begin{pmatrix} 0 \\ 1 \\ 0 \\ -h_{T_2} \end{pmatrix}, \begin{pmatrix} 0 \\ 0 \\ 1 \\ -h_q \end{pmatrix}, \tag{4.7}$$

where h_{T_1}, h_{T_2} and h_q are the first three components of the slowest-decaying left eigenvector of $M^{4\times4}$, $(h_{T_1}, h_{T_2}, h_q, 1)$. Since the slowest-decaying left eigenvector is orthogonal to the subspace spanned by the three fast-decaying eigenvectors and it is orthogonal to each of the modes in Eq. (4.7), it can be proven that the subspace spanned by the three modes designed in Eq. (4.7) is identical to the fast subspace.

In section 4.4, we have scaled the basis functions of q and h_b (as in Figure 4.13) so that both h_{T_1} and h_q equal to 1. Since h_{T_2} is small in practice, we then have the following approximation within the fast subspace

$$T_1 + q + h_b = 0. \tag{4.8}$$

If we interpret T_1, q, and h_b as contributions to column-integrated MSE from the free-tropospheric temperature, the free-tropospheric moisture, and the boundary layer moist static energy, then Eq. (4.8) can be interpreted as column MSE conservation within the fast subspace, and the modes represented by T_1^f, T_2^f, and q^f are simply modes that redistribute MSE throughout the column without net contribution to the column-integrated MSE.

Since our main focus is the convectively coupled branch and it is not sensitive to the slowest-decaying eigenvector of $\mathrm{M}^{4\times4}$, we are going to focus on the dynamics within the fast manifold and derive parameters of the two-mode convective parameterization model from this further simplified model within the fast manifold. We now eliminate the slow manifold in Eq. (4.6) and retain only the fast modes and the associated vertical velocities,

$$\frac{\mathrm{d}}{\mathrm{d}t}\begin{pmatrix} T_1^f \\ T_2^f \\ q^f \\ w_1^f \\ w_2^f \end{pmatrix} = \left(\begin{array}{ccc|cc} & \mathrm{M}^{f3\times3} & & -1 & 0 \\ & & & 0 & -1 \\ & & & a_1^f & a_2^f \\ \hline (kc_1^f)^2 & 0 & 0 & -\varepsilon & 0 \\ 0 & (kc_2^f)^2 & 0 & 0 & -\varepsilon \end{array}\right)\begin{pmatrix} T_1^f \\ T_2^f \\ q^f \\ w_1^f \\ w_2^f \end{pmatrix}, \tag{4.9}$$

First, let us derive the relationship between J_1 and J_2, the convective tendency of T_1^f and T_2^f, from the first two equations in Eq. (4.9). By eliminating T_1^f on the left hand side, it gives the relationship as Eq. (12) in Kuang [2018],

$$J_2 = -\gamma_\circ J_1 - \gamma_q q^f - \gamma_T T_2^f, \tag{4.10}$$

where $\gamma_0 = -m_{21}/m_{11}$, $\gamma_q = m_{13}m_{21}/m_{11} - m_{23}$ and $\gamma_T = m_{12}m_{21}/m_{11} - m_{22}$. The physical meanings of γ_0, γ_q and γ_T are described in Kuang [2018]. Briefly, γ_0 represents the top-heaviness of the convective heating without q^f and T_2^f anomalies; γ_q represents the effect of q^f on the top-heaviness of the convective heating; and γ_T is simply the damping of T_2^f. Considering Eq. (3.11), the parameters r_0 and r_q can be estimated as

$$r_0 = \frac{1+\gamma_0}{1-\gamma_0}, \quad r_q = \frac{\gamma_q}{(1-\gamma_0)L_0} \tag{4.11}$$

Second, we are going to derive the moisture tendency equation, by eliminating T_1^f and T_2^f from the first three equations in Eq. (4.9). It gives us the relationship as Eq. (14) in Kuang [2018],

$$\frac{\mathrm{d}q^f}{\mathrm{d}t} = d_1^f w_1^f + d_2^f w_2^f - d_1 J_1 - d_2 J_2 - d_q q^f \tag{4.12}$$

where $d_1 = (m_{32}m_{21} - m_{31}m_{22})/(m_{11}m_{22} - m_{12}m_{21})$, $d_2 = (m_{31}m_{12} - m_{32}m_{11})/(m_{11}m_{22} - m_{12}m_{21})$, and $d_q = -m_{33} - d_1 m_{13} - d_2 m_{23}$. If we combine the effect of q^f into J_2, we could redefine $\tilde{d}_2$ to be $d_2 - d_q/\gamma_q$. This describes how the parameters in Eq. (3.7a) are estimated.

Third, we will derive the tendency of the boundary layer moist static energy as a function of J_1

and J_2. Since $h_b = -h_{T_1} T_1^f - h_{T_2} T_2^f - h_q q^f$ within the fast manifold, we will have

$$\begin{aligned}
\frac{\mathrm{d}h_b}{\mathrm{d}t} &= -h_{T_1}\frac{\mathrm{d}T_1^f}{\mathrm{d}t} - h_{T_2}\frac{\mathrm{d}T_2^f}{\mathrm{d}t} - h_q\frac{\mathrm{d}q^f}{\mathrm{d}t} \\
&= -h_{T_1}(J_1 - w_1^f) - h_{T_2}(J_2 - w_2^f) - h_q(d_1^f w_1^f + d_2^f w_2^f - d_1 J_1 - d_2 J_2 - d_q q^f) \\
&= (h_{T_1} - h_q a_1) w_1^f + (h_{T_2} - h_q a_2) w_2^f - (h_{T_1} - h_q d_1) J_1 - (h_{T_2} - h_q d_2) J_2 + h_q d_q q^f.
\end{aligned} \tag{4.13}$$

Given that $h_{T_1} \approx 1$, $h_q \approx 1$, $a_1 \approx 1$ and $a_2 \approx 0$, the parameters in Eq. (3.13a) can be estimated as

$$b_1 = h_{T_1} - h_q d_1, \quad \tilde{b}_2 = h_{T_2} - h_q d_2 + h_q d_q/\gamma_q, \tag{4.14}$$

again if we include the effect of q^f in J_2.

Lastly, we are going to derive the quasi-equilibrium relationship, which is the relationship between the tendency of boundary layer MSE and the tendencies of free-tropospheric temperature modes T_1^f and T_2^f. Within the fast manifold, there is an eigenvector that decays much faster than the other two modes so that the fast manifold can be well estimated by the two relatively slow-decaying modes. This allows us to represent q^f as a linear combination of T_1^f and T_2^f,

$$q^f + f_1 T_1^f + f_2 T_2^f = 0 \tag{4.15}$$

Again, given that $h_b = -h_{T_1} T_1^f - h_{T_2} T_2^f - h_q q^f$ within the fast manifold, it leads to

$$\begin{aligned}\frac{\mathrm{d}h_b}{\mathrm{d}t} &= -h_{T_1}\frac{\mathrm{d}T_1^f}{\mathrm{d}t} - h_{T_2}\frac{\mathrm{d}T_2^f}{\mathrm{d}t} - h_q\frac{\mathrm{d}q^f}{\mathrm{d}t} \\ &= (h_q f_1 - h_{T_1})\frac{\mathrm{d}T_1^f}{\mathrm{d}t} + (h_q f_2 - h_{T_2})\frac{\mathrm{d}T_2^f}{\mathrm{d}t} \\ &= (h_q(f_1+f_2) - h_{T_1} - h_{T_2})\left(\frac{h_q f_1 - h_{T_1}}{h_q(f_1+f_2) - h_{T_1} - h_{T_2}}\frac{\mathrm{d}T_1^f}{\mathrm{d}t} + \frac{h_q f_2 - h_{T_2}}{h_q(f_1+f_2) - h_{T_1} - h_{T_2}}\frac{\mathrm{d}T_2^f}{\mathrm{d}t}\right)\end{aligned} \tag{4.16}$$

Comparing with Eq. (3.13b), the parameters can be estimated as

$$F = h_q(f_1+f_2) - h_{T_1} - h_{T_2}, \quad \gamma = \frac{h_q f_1 - h_{T_1}}{h_q(f_1+f_2) - h_{T_1} - h_{T_2}}. \tag{4.17}$$

Based on the derivations above, we are now able to estimate the parameters in a more systematic way. The estimated parameters at different radii are summarized in Table 4.1, and we are going to highlight some of the key features we can learn from the parameters. Note that the parameters are derived from the reduced models with the same basis functions so that a fair comparison across different radii can be made.

First, the parameter γ_q scales with the precipitation rate in general. However, if we normalize γ_q by the precipitation rate, it is nearly zero at 30km, which indicates that additional moist anomaly does not have a strong effect on the top-heaviness of the convective heating at the eyewall because the environment is already moist. γ_q is one of the critical factors that govern the moist-stratiform instability of the convectively coupled waves. A positive γ_q could give rise to such instability, and the larger γ_q is, the stronger the instability is. However, in section 4.3, we found the instability of

the convectively-coupled wave branch at 80km to be much weaker than the instability at 260km, because, in addition to γ_q, the damping parameters γ_T, d_q and b_q tend to scale with the convective strength (or precipitation rate) as well. At 80km, the damping effect from γ_T overcomes the instability effect from γ_q. In addition, the values of $\tilde{d}_2$ and $\tilde{b}_2$ at 30km are very sensitive to the basis functions we applied, because the normalized γ_q is close to zero at 30 km and the effect of q on J_q and h_b cannot be well absorbed into the J_2 term. Second, the magnitudes of b_1 and b_2 are smaller at inner radii, because the boundary layer in the inner region is so moist that the precipitation cannot effectively evaporate. Third, γ and F tend to have large values at smaller radii because the boundary layer tends to be in balance with a deeper free-troposphere when the environment is warmer and moister, and hence the entrainment is less important. Lastly, d_1^f, d_2^f, c_1^f and c_2^f are almost constant along the radius, because these parameters represent the dynamic process and are not sensitive to the change in convective processes along the radius.

Table 4.1: Parameter values for cases along the radius

Parameters	30 km	80 km	100 km	260 km	RCE
d_1^f, d_2^f	1.2, -0.3	1.2, -0.40	1.2, -0.40	1.0, -0.26	1.0, -0.20
γ_0	-0.11	0.21	0.15	0.045	0.14
γ_q, γ_T	-19, 1.3*1000	18, 49	13, 46	1.6, 3.7	0.65, 1.4
d_1, d_2	1.2, -0.30	1.0, -0.36	1.1, -0.38	0.60, 0.51	0.45, 0.70
$\tilde{d}_2$	6.7	-0.83	-0.75	-2.3	-2.1
b_1, b_2	0.030, -0.031	0.17, -0.056	0.13, -0.048	0.44, -0.90	0.54,-0.97
$\tilde{b}_2$	-7.4	0.39	0.41	2.2	1.8
γ, F	2.0, -12	0.70, 8.0	0.74, 4.9	0.47, 2.6	0.46, 2.8
c_1^f, c_2^f	0.97, 0.40	0.91, 0.39	0.96, 0.42	0.91, 0.40	0.89, 0.35

4.6 Revisit the convectively coupled instability in the eigenfrequency model

In Chapter 3, we built a convectively-coupled eigenfrequency model to investigate the linear instabilities of asymmetries in a tropical-cyclone like vortex, and applied the convective parameters estimated from previous studies [Kuang, 2008a, Andersen & Kuang, 2008] and modified them based on physical intuitions. This was certainly a useful first step to take, however it lacked a solid foundation and the quantitative accuracy for estimating the parameters. Therefore, in this section we are going to apply the parameters estimated in this chapter, and revisit the linear instabilities of the asymmetries from the eigenfrequency model. The parameters are summarized in Figure 4.15, where the solid curves represent the fit of r_q, γ and b_1 estimated from the derived values at several specified radii which are shown as crosses. Qualitatively, the change of the parameter values along the radius is consistent with our physical intuitions described in Chapter 3. However, the framework based on linear response functions constraints the parameters with more quantitative accuracy and provides more insights as to how the parameters change over the radius. More importantly, the linear response function based framework can show where the parameters change rapidly, and therefore more linear response functions in that region need to be constructed.

When the parameters estimated from the linear response functions are applied to the convectively coupled model, Figure 4.16 shows the growth rates and the propagating speeds of the unstable modes. The general features of the unstable modes are similar to the experiment with parameters modified based on simple physical intuitions, but growth rates of the nearly stationary modes are not monotonically increasing with azimuthal wavenumber. Instead, the growth rate now peaks at

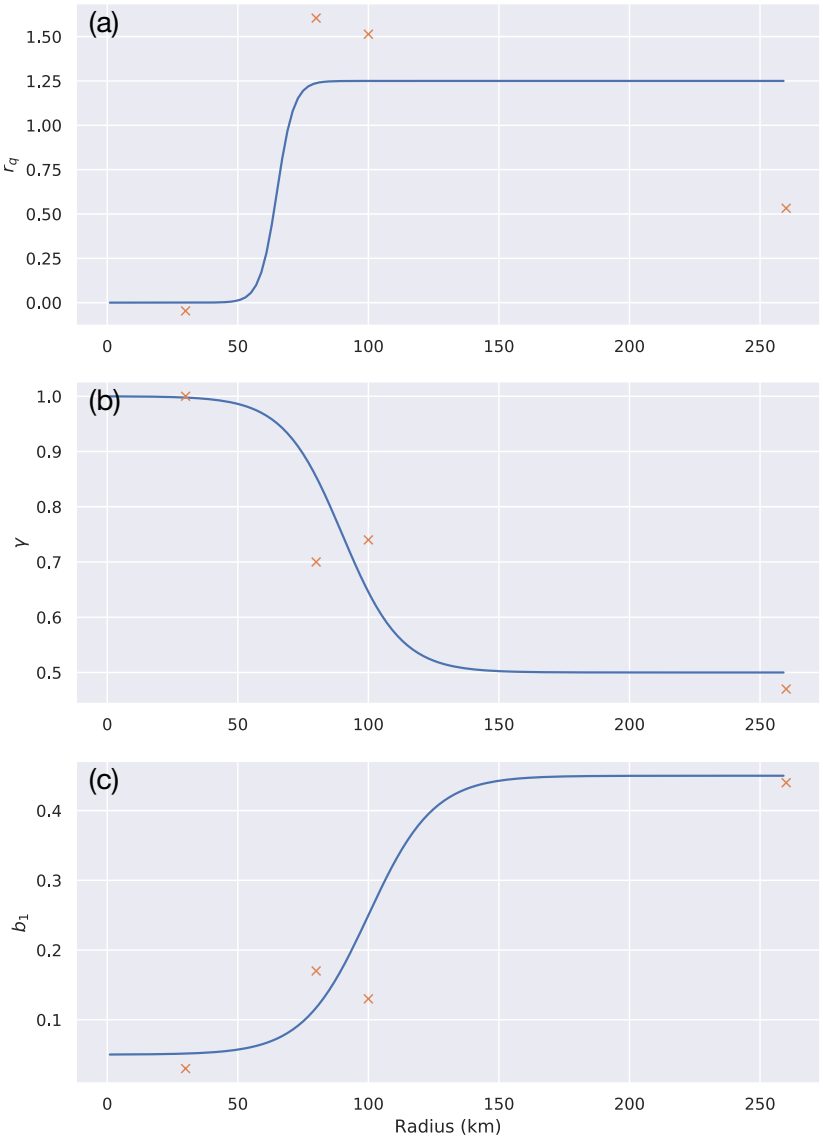

Figure 4.15: Parameter estimates of (a) r_q, (b) γ and (c) b_1 based on the framework of linear response functions. The crosses indicate the direct estimates from the framework of linear response functions, and the lines in blue represent the fit onto a functional form of a step function.

wavenumber 3. The growth rate of the wavenumber-one and wavenumber-two perturbations are also stronger than the previous cases. However, it is still different from what we observe from the WRF simulations whose signal is the strongest at wavenumber one. Figure 4.17 shows both the horizontal and vertical structure of temperature and convective heating fields of the nearly stationary unstable mode with azimuthal wavenumber-two. Similar to the previous experiments in Chapter 3, the temperature structure is dominated by the second baroclinic mode, while the convective heating is dominated by the first baroclinic mode, indicating the convectively-coupled origin of the unstable modes. In addition, the horizontal structures of the temperature and convective heating now have a clear spiral structure.

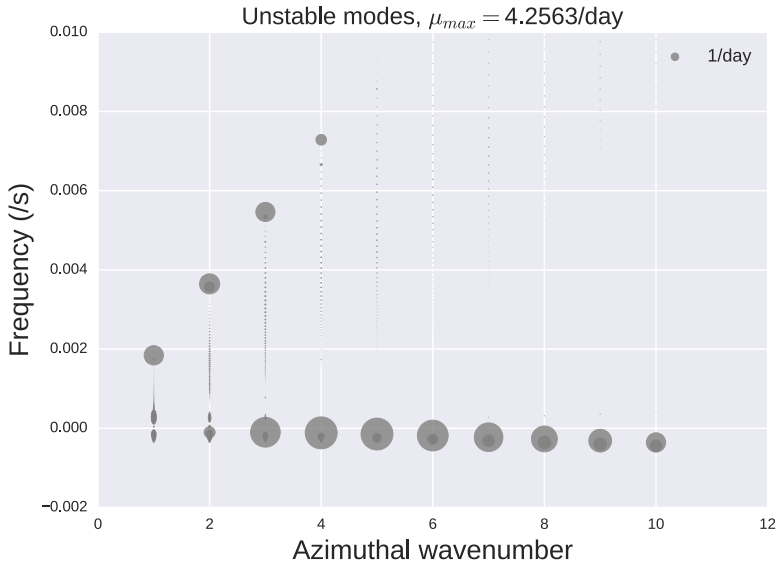

Figure 4.16: Propagating speeds and growth rates of the unstable modes from the convectively coupled eigenfrequency model with refined parameters based on linear response functions. The size of the dots indicate the strength of the growth rates.

[Kuang, 2008a] pointed out that with increasing relaxation timescale τ_L, the instability at higher

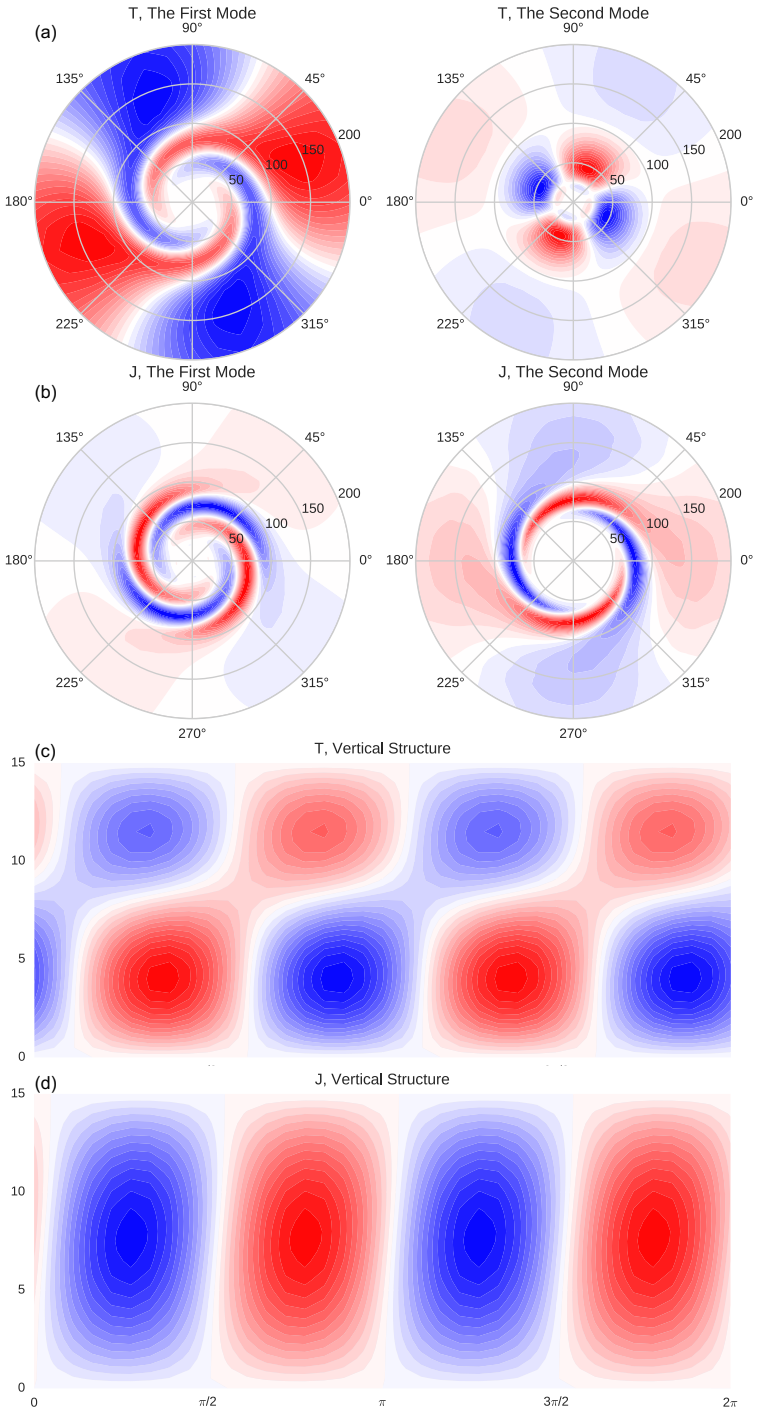

Figure 4.17: Horizontal and vertical structure of the most unstable mode from the convectively coupled eigenfrequency model with refined parameters based on linear response functions. (a) is the horizontal temperature structure; (b) is the horizontal heating structure; (c) is the vertical temperature structure and (d) is the vertical heating structure.

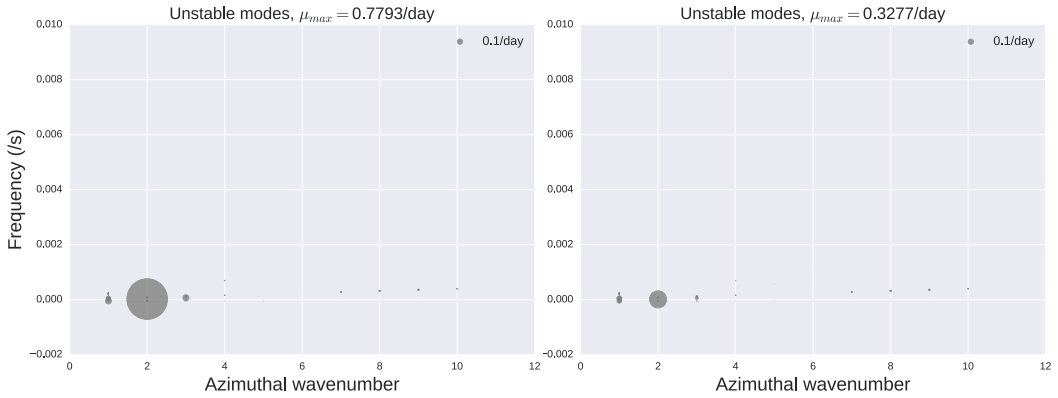

Figure 4.18: Propagating speeds and growth rates of the unstable modes from the convectively coupled eigenfrequency model with refined parameters based on linear response functions, (a) with τ=10 minutes, and (b) with τ=30 minutes. The size of the dots indicate the strength of the growth rates.

wavenumber is preferably reduced. Therefore, we performed a sensitivity test of the relaxation timescale τ_L (Figure 4.18), and verified that the unstable convectively coupled modes are indeed inhibited at higher azimuthal wavenumber. The overall instability of the convectively coupled branch is greatly reduced due to the increased relaxation time scale. In order to visualize the sensitivity of the gravity wave branch to τ_L, the instability of the mixed vortex-Rossby gravity wave is not plotted in Figure 4.18.

4.7 Conclusion

In this chapter, we demonstrated a systematic procedure that can guide us toward the construction of a simple convective parameterization model and help us quantitatively constrain the parameters.

We started by constructing linear response functions, which are considered as a complete model that relates the thermodynamic state variables to their convective tendencies. The linear response

functions are constructed around several reference states along the radius, and we found that the linear response functions at outer radii qualitatively resemble the behavior of the linear response functions of the RCE case. At inner radii, when the environment is very warm and moist, the convection tends to quickly damp any temperature and moisture anomalies and adjust the temperature and moisture toward a moist adiabatic profile.

With the linear response functions, we then reduce the order of the convectively coupled 2-D gravity wave system to retain only two vertical velocity modes and four thermodynamic modes. The reduced sixth-order model is able to reproduce the behavior of the least damped mode from the full model based on the linear response functions. The retained thermodynamic modes include two free-tropospheric temperature modes, one free-tropospheric moisture mode and one boundary layer MSE mode, which is consistent with the choices of the previous simple models.

After we reduce the order of the convectively coupled system, we split the reduced model into a slow manifold and a fast manifold and focus only on the fast manifold because the instability of the convectively coupled branch is not sensitive to the change in the slow manifold. This procedure also allows us to cast the reduced model into the form of the two-mode convective parameterization and to estimate the parameters in the convective parameterization. The trends of the parameters along the radius are generally consistent with our physical intuitions, as discussed in section 4.5.

Lastly, we applied the parameters estimated from the framework of linear response functions to the eigenfrequency model and revisit the linear instabilities from the simple model. The strongest instability of the convectively-coupled branch now shifts toward lower azimuthal wavenumber, though the model with the refined parameters still fails to capture the stronger signals at azimuthal

wavenumber-one and wavenumber-two. Such improvements encourages to build more linear response functions along the radius to constrain the parameters more.

To summarize, we applied the framework developed in Kuang [2018] to better constraint the convective response in an idealized tropical cyclone based on linear response functions. Such a framework builds a more solid foundation for the construction of simple convective parameterizations, validates the physical intuitions behind the parameter choices, and estimates the parameters in the simple convective parameterization with more quantitative accuracy.

5

A new framework to study SEF

5.1 Introduction

In the previous chapters, we have discussed the asymmetric features of a tropical cyclone, including the propagating characteristics and potential mechanisms of spiral rainbands and eyewall deformations. In this chapter, we are going to discuss another remarkable structural feature of tropical cyclones that is closely related to the intensity changes of tropical cyclones, the secondary eyewall for-

mations (SEF). Secondary eyewall formations represent the process during which an outer eyewall and a secondary wind maxima form at several times the radius of the primary eyewall. They are frequently observed in matured hurricanes and are often associated with a temporary weakening of the hurricane intensity when the outer eyewall contracts and intensifies, followed by an increase in the area covered by strong winds and consequent damages.

Previous studies have proposed many possible mechanisms for SEF. Early studies [Shapiro & Willoughby, 1982, Schubert & Hack, 1982, Hack & Schubert, 1986] emphasized the importance of dynamical adjustment to latent heating outside the primary eyewall by using a variation of the Eliassen [1951] balanced vortex model. Recently, Moon & Nolan [2010] studied the response of the hurricane wind field to the rainband heating with a 3-D, non-hydrostatic, linear model of vortex dynamics. They showed that realistic distributions of asymmetric diabatic heating in outer rainbands could reproduce secondary wind maximum and other circulation features often observed in rainbands. With WRF simulations, Rozoff et al. [2012] found that the secondary eyewall emerged where increased inertial resistance increases the efficiency with which latent heating locally warms the troposphere and increases the tangential winds.

In addition to the dynamical adjustment, many recent papers [Smith et al., 2009, Huang et al., 2012, Kepert, 2013] argued that the unbalanced boundary layer dynamics is essential in initiating or contributing to the SEF and eyewall replacement cycle. Smith et al. [2008] argued that a major deficiency in conventional hurricane theory is the assumption of gradient wind balance in the boundary layer. Using a slab boundary layer model, they addressed the role of the supergradient wind, the over-shooting radial inflow, and a resulting strong convergence region within the boundary layer

in spinning up the hurricane and forming the primary eyewall. Huang et al. [2012] proposed that a similar mechanism also applies to SEF, and Abarca & Montgomery [2013] further concluded that axisymmetric boundary layer dynamics alone are capable of developing secondary wind maxima. In contrast, Kepert [2013] argued that the boundary layer could assist but not initiate SEF. He found that the updraft motion within the boundary layer is simply determined by the vorticity field applied above through Ekman pumping. Recently, Kepert & Nolan [2014] qualitatively specified a physical link between the boundary layer convergence and the deep convection, in which the boundary layer convergence can localize convection through the release of conditional instability, reduction of stability from vertical stretching, or through moisture convergence. One limitation of most of the boundary layer models is that they assumed the vortex in the free-troposphere to be constant and did not account for the feedback from the boundary layer to the imposed pressure gradient at the top.

Several studies have tried to compare the relative importance of dynamical adjustment and unbalanced boundary layer processes. Rozoff et al. [2012] found that response to diabatic forcing dominates the response to frictional forcing, and Menelaou et al. [2014] argued that the secondary wind maxima could be generated even without boundary layer physics. However, Menelaou et al. [2014] used a dry dynamic model, thus neglected the feedback between moist convection and boundary layer flow, which is likely important for SEF. The boundary layer dynamics may serve to modify temperature and moisture profile through the convergence of enthalpy, therefore increasing instability and CAPE, and these indirect effects of the boundary layer dynamics on SEF require futher tests.

A convincing mechanism of SEF is still lacking, mainly because the dynamics and the moist convections associated with SEF are strongly coupled, and the causality remains a "chicken and egg" problem. A comprehensive model, such as WRF, can simulate the phenomenon of SEF; however, it is difficult to use such a model to directly study the feedback between the convections and dynamics since they are highly coupled in such a comprehensive model. Therefore, the primary purpose of this chapter is to introduce a new framework that aims to untangle the feedback between convective processes and axisymmetric dynamics and allows more flexibility for us to test different hypotheses.

The rest of the chapter will be organized in the following sections. In section 5.2, we will introduce the WRF simulations of SEF, which will be considered as ground truth for the simple model to compare. We will then introduce the simple axisymmetric framework in section 5.3 and describe the coupling between the dry axisymmetric model and a cloud-resolving model. In section 5.4, we will discuss some preliminary results, and in section 5.5 we will highlight some potential directions of the coupled framework.

5.2 Idealized simulation of SEF in WRF

We use the Weather Research and Forecasting (WRF) model to perform an idealized simulation of SEF in a tropical cyclone. The model configuration is similar to those used in a previous idealized hurricane study [Zhu & Zhu, 2014]. The model surface is set to be sea surface with a homogenous surface temperature of 29°C. The simulation is performed on an f-plane with a constant Coriolis parameter equivalent to that at 20°N. The simulation is done over three two-way nested do-

mains with a horizontal resolution of 2km, 6km, and 18km and domain size of 600km×600km, 1080km×1080km and 5400km×5400km. Doubly-periodic lateral boundary conditions are applied to the outermost lateral boundaries. The outermost domain is large enough to prevent interaction among hurricanes across the lateral boundaries. There are 47 levels in the vertical with a model top at approximately 20hPa. The simulation is run for 96 hours, and the history snapshots are output every 10 minutes in the inner domain.

We use the Mellor-Yamada-Janjic (MYJ) scheme [Janjić, 1996, 2001] for the subgrid-scale (SGS) vertical turbulent mixing, and the 2-D Smagorinsky [1963] turbulence scheme for horizontal diffusion. The Charnock formula [Charnock, 1955], used in the MYJ surface scheme to determine surface roughness, is replaced by the formula proposed by Davis et al. [2008] to reflect the observed variation of drag coefficient in the high wind regime [Donelan et al., 2004]. We choose the Thompson scheme [Thompson et al., 2004, 2008] for microphysics, and the Kain-Fritsch scheme [Kain, 2004] as the cumulus parameterization for the outermost domain. No cumulus parameterization is used in the two inner domains. We use the Rapid Radiative Transfer Model radiation (RRTM) scheme [Mlawer et al., 1997] for longwave radiation and the Dudhia scheme [Dudhia, 1989] for shortwave radiation. Since this idealized study focuses on internal feedbacks, vertical wind shear and other environmental forcing are not imposed in the simulation.

We initialized the simulation with an idealized category-1 hurricane vortex, and the temperature and the pressure fields are in hydrostatic balance and gradient wind balance with the vortex wind. The radial profile of the tangential wind is determined based on Wood & White [2011]'s formula, and the vertical extension is based on an analytical function proposed by Nolan & Montgomery

[2002]. The initial far-field temperature and humidity profiles are specified by the non-Saharan air layer sounding of Dunion & Marron [2008], which is a modified and extrapolated version of Jordan [1958].

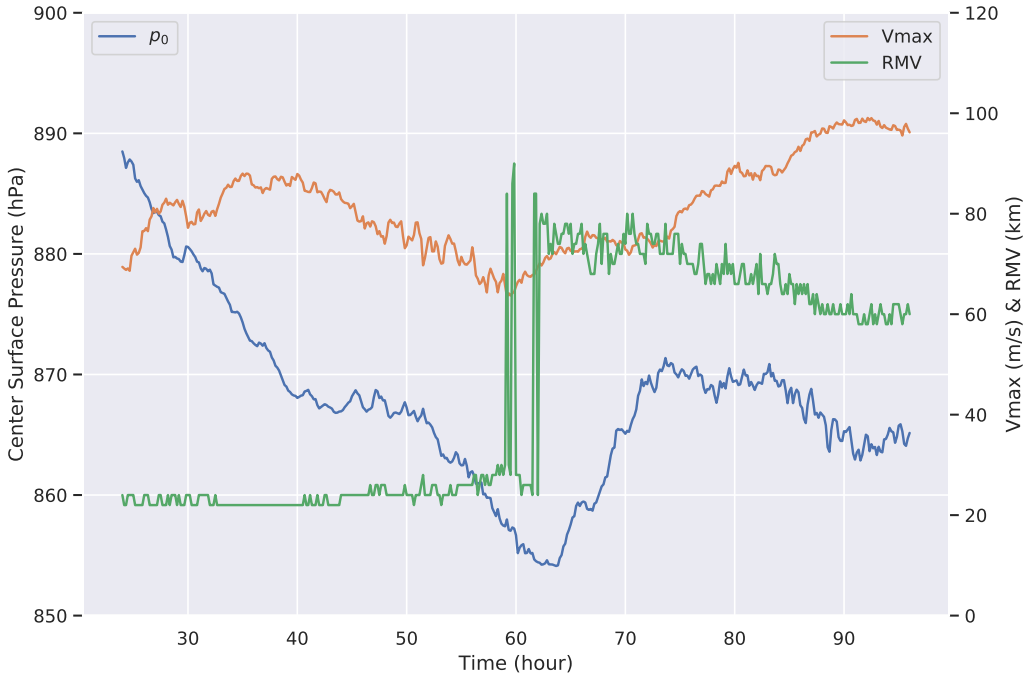

Figure 5.1: Time evolution of the centeral surface pressure (hPa, blue curve), the maximum mean tangential wind at the height of 1 km (m/s, yellow curve), and the radius of maximum wind (km, green curve) of the WRF simulation.

Figure 5.1 shows the time series of the surface pressure at the center of the storm, the maximum azimuthal mean tangential winds, and the radius of the maximum wind (RMW) at the height of 1km of the simulated vortex. After the initial spin-down, the deep convection develops and saturates the vortex core, and the storm can be self-maintained. The storm undergoes a rapid intensification during which the central surface pressure quickly drops to about 870 hPa, the maximum tangential wind increases to 90 m/s and the RMW contracts to 30 km. At 60h, there is a sudden increase

in RMW and a drop in the maximum tangential wind, which corresponds to the formation of a secondary eyewall. After the secondary eyewall forms, the eyewall replacement cycle begins, during which the maximum tangential wind recovers, and the RMW contracts to a smaller radius. During the same period, the central surface pressure slightly increases. Once the ERC is completed, the tropical cyclone re-intensifies to a stage with stronger tangential winds and larger impact area than before.

Figure 5.2 shows the snapshots of the simulated radar reflectivity at the height of 1km during the ERC with a time interval of 4 hours and illustrates a horizontal view of the ERC. During the early stage from 28h to 52h, scattered convections start to develop at a larger radius. Then convections become more organized and begin to spiral inward and wrap around the primary eyewall. At 56h, a closed secondary eyewall forms with a well organized spiral rainband attached at a larger radius. During the ERC (from 56 h to 76 h), the secondary eyewall continues to intensify and contract, while the primary eyewall becomes weaker and weaker and eventually diminishes. After the ERC, the outer eyewall takes over the role of the primary eyewall and remains at a radius about 30 km larger than the original one. The time evolution of azimuthal mean vertical velocity at the height of 5km and the tangential wind at the height of 1km are shown in Figure 5.3, which provides an azimuthally averaged view of the SEF and ERC. It confirms that weak updrafts form at a larger radius between 150km to 200km before 50h and rapidly propagate inward and form a secondary eyewall at about 80km. After the ERC is completed, the tropical cyclone becomes a stronger and larger one.

Although the simulation is performed with an idealized setting, it resembles many of the critical aspects that were observed from the flight-level data and satellite microwave imagery [Sitkowski

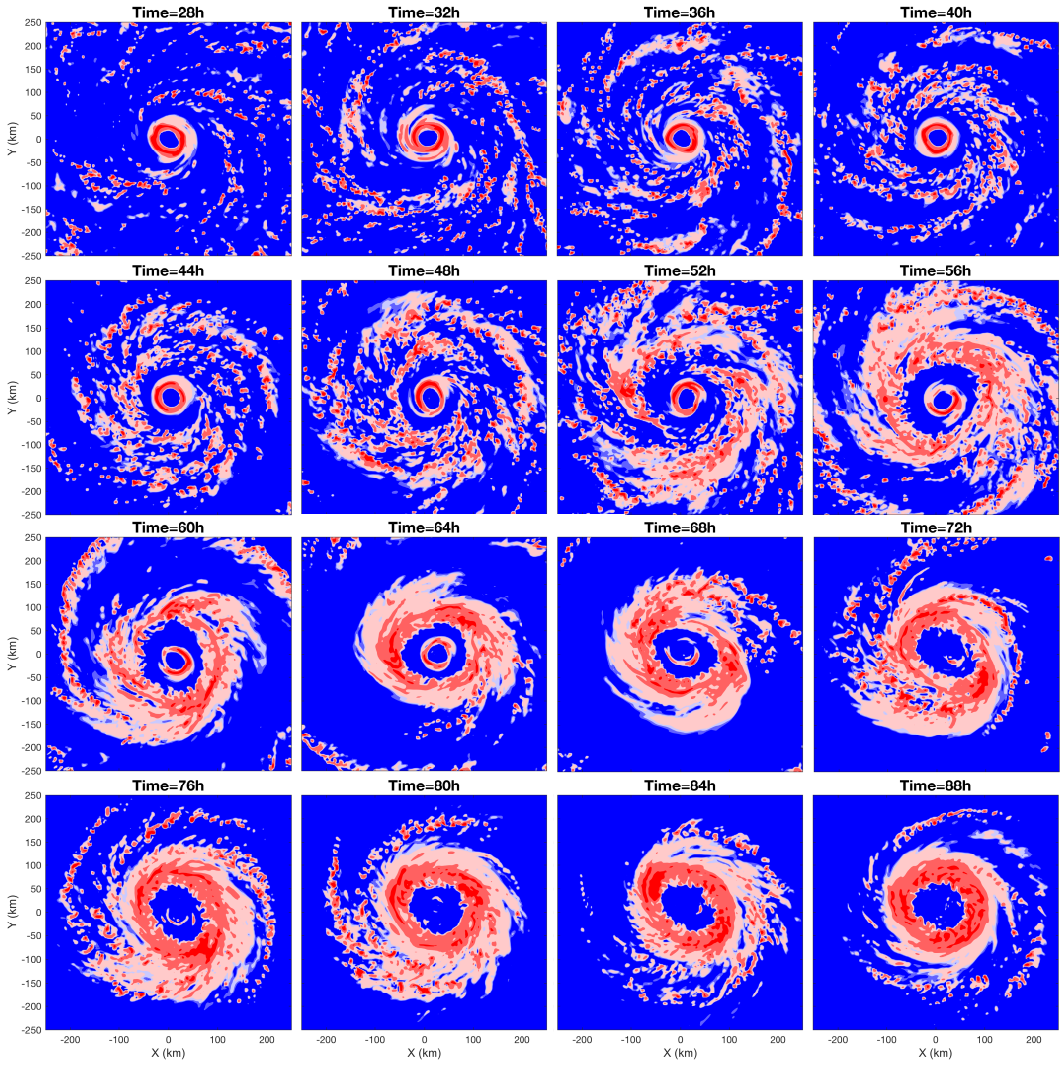

Figure 5.2: Snapshots of synthetic radar reflectivity (dBZ) at the height of 1 km from the 28th hour to the 88th hour at a time interval of 4 h.

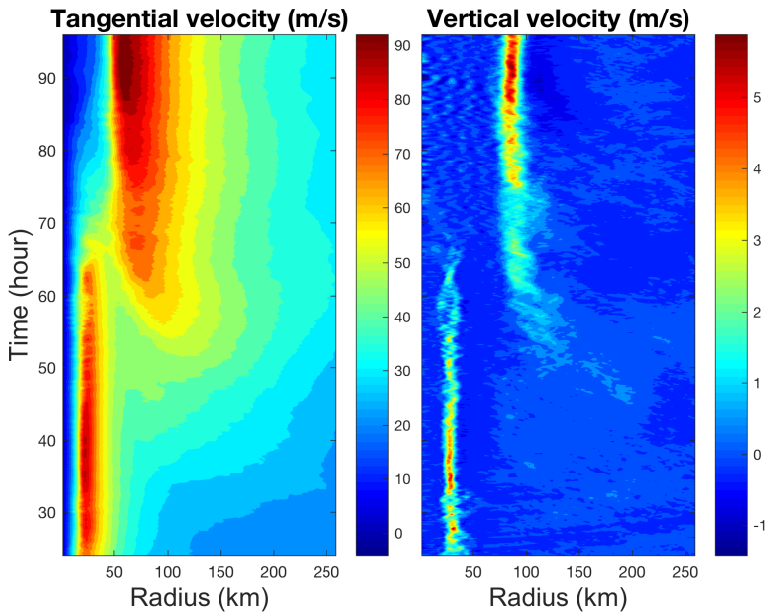

Figure 5.3: Hovmöller diagram of the azimuthal mean (a) tangential wind (m/s) at the height of 1 km and (b) vertical velocity (m/s) at the height of 5 km.

et al., 2011]. Therefore, for the rest of the chapter, we are going to consider this idealized simulation from a full physics model as the ground truth to validate the simple framework that we are going to develop.

5.3 The convectively coupled axisymmetric framework

The convectively coupled axisymmetric framework consists of two parts, a dry axisymmetric dynamic model that simulates hurricane-scale circulation as the response to convective heating, and a cloud-resolving model that resolves local convections given the forcing from the hurricane-scale circulation. The framework explicitly simulates the feedback between the hurricane-scale circulation and local convections, therefore provides us more flexibility to manipulate one component or

another in the whole feedback loop and allows us to test different hypothesis directly.

5.3.1 The dry axisymmetric dynamic model

The dry axisymmetric dynamic model largely follows the numerical model developed by Rotunno & Emanuel [1987], except that all the processes of moist convections have been externalized, and all the hydro-variables are set to zero. The axisymmetric model is non-hydrostatic and compressible, and can be written in the following form,

$$\frac{\partial u}{\partial t} = -u\frac{\partial u}{\partial r} - w\frac{\partial u}{\partial z} + (f + \frac{v}{r})v - c_p\bar{\vartheta}\frac{\partial \pi}{\partial r} + D(u) \tag{5.1a}$$

$$\frac{\partial v}{\partial t} = -u\frac{\partial v}{\partial r} - w\frac{\partial v}{\partial z} - (f + \frac{v}{r})u + D(v) \tag{5.1b}$$

$$\frac{\partial w}{\partial t} = -u\frac{\partial w}{\partial r} - w\frac{\partial w}{\partial z} - c_p\bar{\vartheta}\frac{\partial \pi}{\partial z} + D(w) + g\frac{\vartheta - \bar{\vartheta}}{\bar{\vartheta}} \tag{5.1c}$$

$$\frac{\partial \pi}{\partial t} = -\frac{\bar{c}^2}{c_p\bar{\varrho}\bar{\vartheta}^2}(\frac{1}{r}\frac{\partial (ru\bar{\varrho}\bar{\vartheta})}{\partial r} + \frac{\partial (w\bar{\varrho}\bar{\vartheta})}{\partial z}) \tag{5.1d}$$

$$\frac{\partial \vartheta}{\partial t} = -u\frac{\partial \vartheta}{\partial r} - w\frac{\partial \vartheta}{\partial z} + H_{diab} + D(\vartheta) \tag{5.1e}$$

The five prognostic variables are the velocities in the radial, azimuthal, and vertical directions, (u, v, w); the non-dimensional pressure perturbation from its base state π; and the potential temperature ϑ. Parameters include f, the Coriolis parameter, c_p, the specific heating of dry air at constant pressure, $\bar{c}$, the speed of sound and $\bar{\varrho}$, the density of air. Quantities with an overbar represent their reference states, which are functions of z only, and here the reference state is chosen to be the motionless hydrostatic state. The symbols D denote diffusive processes, which are dominated by eddy diffusion

in an axisymmetric model. H_{diab} is the azimuthal mean convective heating from microphysics and convection, treated as an external forcing to the dry dynamic model. Depending on the purpose of the experiments, the convective heating can either be diagnosed from a full physics simulation or computed from a cloud-resolving model coupled to the dry model as shown in section 5.3.2.

For details of the axisymmetric model, including its diffusion scheme, boundary conditions, the design of its top sponge layer, the treatment of its radiative cooling, and its space discretization, please refer to Rotunno & Emanuel [1987]. One detail that we have done differently from Rotunno & Emanuel [1987] is that we excluded the Richardson number dependence of the diffusivity μ, because we found that the vertical diffusivity can be too small to smooth out small scale noise under large Richardson number regime, and it can cause instability when the dry model is then coupled with a CRM. We use the 4th-order Runge-Kutta scheme for time integration.

5.3.2 Coupling with a cloud resolving model

On top of the dry axisymmetric model, we are going to cover a small region of the domain with a cloud-resolving model to resolve local convections. The CRM obtains hurricane-scale forcing such as the horizontal and vertical advection of temperature and moisture from the dry axisymmetric model and calculates local convective heating, which is then fed back to the axisymmetric model. On the one hand, the coupling internalizes the forcing of convective heating locally, which is now evolving with the hurricane-scale dynamics and not simply an external forcing. On the other hand, we still have the flexibility to manipulate each component of the system.

To study SEF, we choose to have the CRM covering the area of outer rainbands, which even-

tually develop into a secondary eyewall so that the interaction between the convection within the secondary eyewall region and the hurricane-scale circulation can be directly represented. The CRM domain is slanted to account for the slanted structure of convection. Both the dry axisymmetric model and the CRM are initialized with the same initial condition, including the same initial sounding and the same forcing. During each iteration of the coupling, the cloud-resolving model is forced by the hurricane-scale vertical velocity w, and the large-scale temperature forcing, $F = -u\frac{\partial}{\partial x} + D(\vartheta) + R_{cooling} + R_{damping}$ diagnosed from the dry model, and feeds the updated convective heating Q_{CRM} back to the dry model. Since the dry model does not have prognostic equations for the hydrometers, the large-scale forcing of the water vapor is not included in the feedback between the dry model and the CRM.

Specifically, we use the System for Atmospheric Modeling (SAM, Khairoutdinov & Randall [2003]) as the cloud-resolving model. All simulations are performed over an ocean surface with a fixed sea surface temperature of 29°C. The horizontal domain size is 64km × 64km with a resolution of 0.5 km. There are 70 vertical layers with 300m vertical resolution. The top third of the domain is a wave-absorbing layer.

5.4 Preliminary results

To validate the dry axisymmetric model, we first force the model with convective heating diagnosed from the WRF simulation. Figures 5.4 and 5.5 shows the structure of the tangential winds (m/s) and vertical winds (m/s) from the dry model as a function of height and radius compared to those from

the WRF simulations during the ERC.

Qualitatively, the dry axisymmetric model can reproduce the circulation structure from the WRF simulation, given the convective heating diagnosed from WRF. It can reproduce the super-gradient tangential wind in the boundary layer during the early stage of secondary eyewall formation. Near the outer boundary of the dry model, the vortex structure tends to be flat along the radius mainly due to the flux form boundary condition used at the outer boundary, which largely eliminates the horizontal gradient of variables. The vertical velocity from the dry model resembles those from the WRF simulation as well but is less noisy than those from WRF. Quantitatively, the dry model tends to produce weaker circulation than those from WRF. Such differences may be caused by the axis-symmetric simplification made by the dry model. The WRF simulations are fully three-dimensional, while the dry model is an axis-symmetric model with the asymmetric terms being parameterized. Therefore, the dry model cannot replicate the WRF simulations perfectly, but it is useful to study the behavior of the hurricane-scale circulation as response to the convective heating.

5.5 Potential future directions

The first experiment this model would be able to test is whether intensification of secondary eyewall is due to linear instability or finite amplitude instability. Both the dry model and the CRM can be initialized to the same steady state. Then an instantaneous heating perturbation can be introduced to the system to kick the system from its balanced state. From this experiment, we can test how large the perturbation is necessary for the secondary eyewall to develop, at which height such perturba-

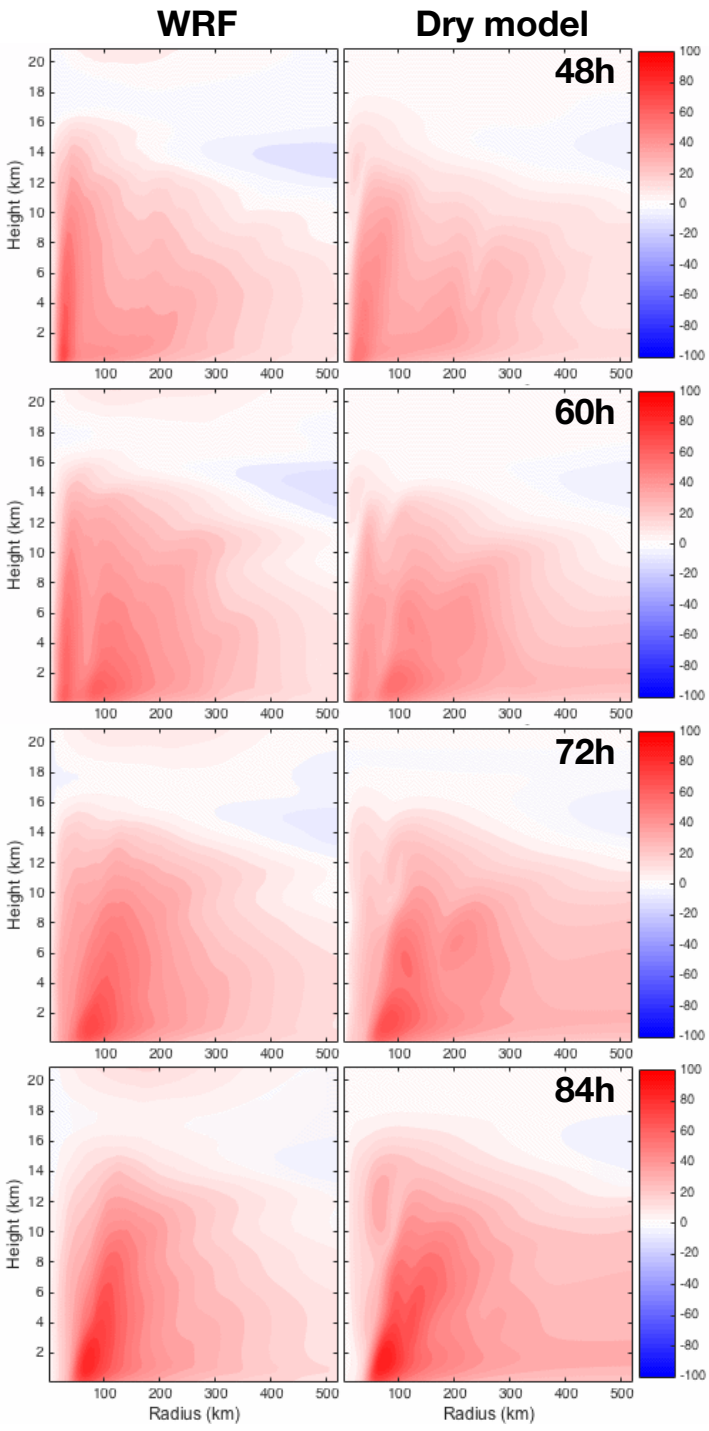

Figure 5.4: Snapshots of tangential winds (m/s) as a function of height and radius from the WRF simulation (on the left) and the dry model (on the right) forced by the convective heating from the WRF simulation.

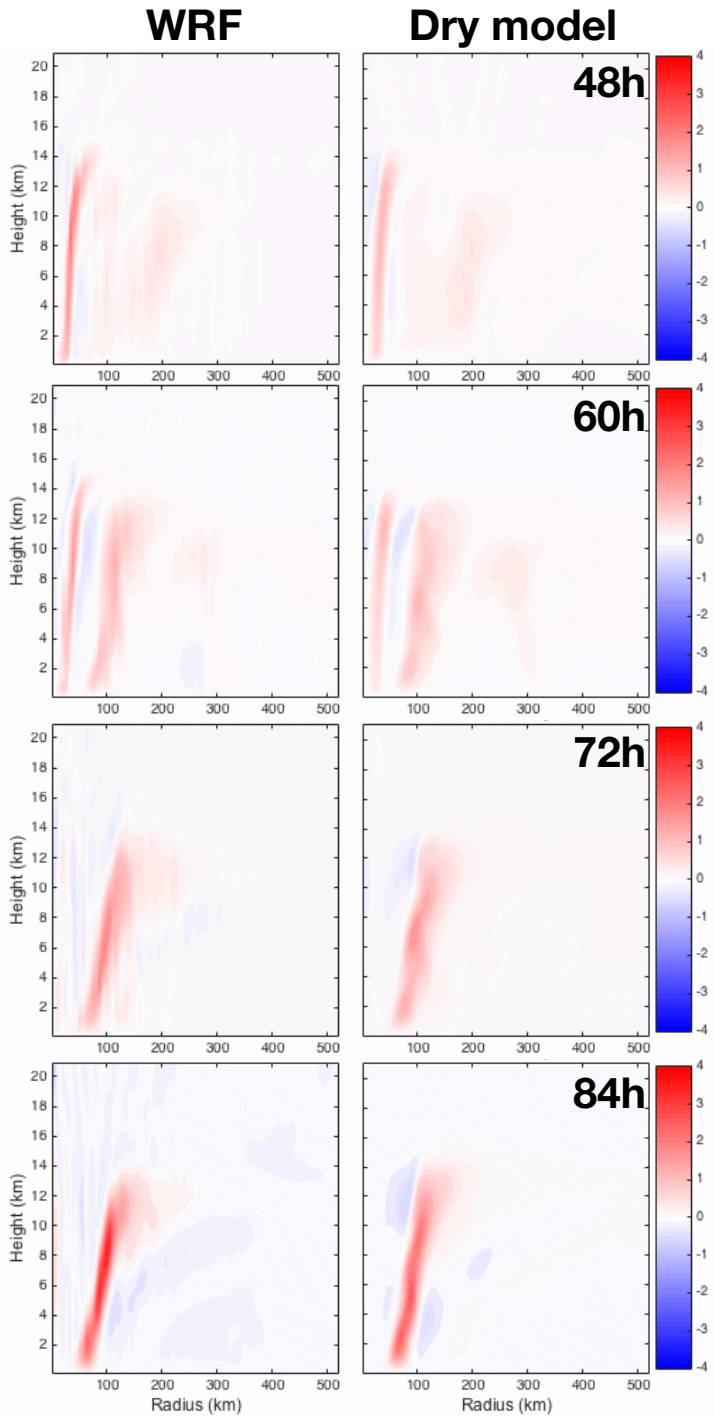

Figure 5.5: Snapshots of vertical winds (m/s) as a function of height and radius from the WRF simulation (on the left) and the dry model (on the right) forced by the convective heating from the WRF simulation.

tion could effectively trigger the secondary eyewall formation.

Second, the model can also be used to test the effect of wind dependent surface fluxes. As a control experiment, we could fix the local surface fluxes and test whether the secondary eyewall can still develop and be able to maintain itself. As a comparison, we could then allow the surface fluxes to be interactive with the surface wind and see if it makes any differences.

Third, to test the inertial stability hypothesis, we can tune the background vortex structure to change the azimuthal mean inertial stability. With all other conditions to be the same, we could test whether and how the secondary eyewall will develop.

6

Conclusions and Future Work

6.1 Conclusions

Understanding the structure of a tropical cyclone, such as deformations of the eyewall, spiral rainbands, or concentric eyewalls, is critical for understanding the track and intensity change of a hurricane. Many studies have shown that organized structure features [Schubert et al., 1999, Montgomery & Kallenbach, 1997, Kossin & Schubert, 2001, Nolan et al., 2001, Hendricks et al., 2009,

Wang, 2009, Hendricks & Schubert, 2010, Naylor & Schecter, 2014] are associated with the intensity and track change of tropical cyclones. In the thesis, we investigated both the asymmetric the symmetric structures of an idealized hurricane.

For asymmetric features of a hurricane, they are usually classified into different categories based on how far they are from the center of a hurricane and are considered to be related to different mechanisms. To capture the asymmetries, most studies [Reasor et al., 2000, Wang, 2001, Chen & Yau, 2001, Wang, 2002, Corbosiero et al., 2006] tend to focus on a limited area of a hurricane and study the characteristics of asymmetries from either Hovmöller diagram or a series of snapshot structures. In terms of their mechanism, some studies suggest that they are associated with vortex Rossby-waves [Schubert et al., 1999, Reasor et al., 2000, Kossin & Schubert, 2001, 2004, Kossin et al., 2002], or inertial gravity waves [Abdullah, 1966, Kurihara, 1976, Willoughby, 1978, Diercks & Anthes, 1976, Willoughby et al., 1984]. In contrast, others suggest that they might be related to the instabilities of inertia-Gravity wave radiated from a Rossby-like wave in the vortex core [Ford, 1993, 1994a,b, Schecter & Montgomery, 2004, Menelaou et al., 2016]. However, the connection among different radii can be easily ignored if we only focus on a limited area, and a complete view of the asymmetric features in hurricanes and their instability mechanisms can hardly be revealed. Therefore, in the first three chapters, we intended to more systematically document the asymmetric characteristics across different radii of an idealized hurricane and to better understand the instability mechanisms that can potentially lead to such asymmetries.

In Chapter 2, we dived into the frequency-wavenumber space and found that there are two distinct spectral peaks in the power of asymmetries in the simulated hurricanes both near and outside

the eyewall. The fast propagating branch propagates slower than the background rotation near the eyewall but much faster than the local background rotation outside the eyewall. Its propagating speed and its horizontal structure suggest that the mixed vortex-Rossby-inertial-gravity instability is a plausible mechanism. The other spectral peak is nearly stationary in the absolute reference frame, but intrinsically it is a fast retro-propagating gravity wave. The vertical structure of the dynamic and convective fields of this wave resemble those of convectively coupled waves and encourage us to explore more on the effect of convective coupling.

Given the two branches of signals that we saw in the WRF simulations, we then moved on to investigate the instability mechanisms that can potentially be related to the asymmetries. In Chapter 3, we developed a convectively coupled eigenfrequency framework to study the linear instability of a TC-like vortex, in particular from the perspective of convectively coupled waves.

The simple model can produce a branch of fast propagating unstable modes even without convective coupling. Similar to the WRF simulation, the unstable modes are dominated by an azimuthal wavenumber-2 asymmetry, and its structure is consistent with a vortex-Rossby wave in the inner vortex radiating an outward propagating gravity wave outside. With convective coupling, strong instabilities can arise from the convectively coupled dynamics, i.e., the moist-stratiform instability. The unstable modes from the convectively coupled dynamics have much slower propagating speeds than their background rotation rates. They are therefore considered as convectively coupled gravity waves propagating against the background vortex. After tailoring the parameters of the convective parameterization to be more suitable for the eyewall region, the convectively coupled unstable modes become nearly stationary, which is more consistent with the slow propagating wave from the

WRF simulations. The unstable modes now have spiral structures and strong perturbations beyond the eyewall. With the refined parameters from Chapter 4, we found that the growth rate of the convectively coupled peaks at azimuthal wavenumber three instead of increasing with the azimuthal wavenumber, but the simple model is still not able to produce strong instability at wavenumber one. Although the simple model cannot replicate the feature of the slow-propagating branch in the WRF simulations perfectly, the results suggest the importance of convective coupling in generating unstable modes in TC-like vortices and encourages future studies to explore more from the convectively coupled perspective.

To better constrain convective parameterization, we demonstrated a systematic procedure that guided us toward the construction of a simple convective parameterization model and helped us constrain the parameters with more quantitative accuracy in Chapter 4.

We started by constructing linear response functions around several representative reference states along the radius. The linear response functions are considered as a complete model that relates the thermodynamic state variables with their convective tendencies. We found that the linear response functions at outer radii qualitatively resemble the behavior of the RCE case. In contrast, at inner radii, where the environment is very warm and moist, the convection tends to quickly damp any temperature and moisture anomalies and adjust the temperature and moisture toward a moist adiabatic profile.

With the linear response functions, we then reduce the order of the convectively coupled 2-D gravity wave system to retain only two vertical velocity modes and four thermodynamic modes, which include two free-tropospheric temperature modes, one free-tropospheric moisture mode and

one boundary layer MSE mode in most of the cases. The optimally retained modes are consistent with the choices of the two-mode convective parameterization. The reduced sixth-order model can reproduce the behavior of the least damped mode from the full model based on the linear response functions. After we reduce the order of the convectively coupled 2-D gravity wave system, we split the reduced model into a slow manifold and a fast manifold and estimate the parameters in the convective parameterization within the fast manifold, because the instability of the convectively coupled branch is not sensitive to the change in the slow manifold.

To summarize, we first analyzed the asymmetric signals near and beyond the eyewall from an ensemble of idealized hurricanes simulations in WRF. We found a fast-propagating signal, which is considered as a mixed vortex-Rossby-gravity wave and a nearly stationary wave whose vertical structure resembles that of a convectively-coupled wave. To understand the instability mechanisms of the signals seen in the WRF simulations, we then developed a convectively coupled eigenfrequency framework to investigate the linear instabilities of a TC-like vortex. We confirmed that the mixed type of instability could generate the fast-propagating branch even without convective coupling, and the moist-stratiform instability embedded in the convectively coupled dynamics can give rise to the nearly stationary branch. To better constrain the convective response in the tropical cyclones, we then applied the framework based on linear response functions developed by Kuang [2018] to estimate the parameters in the simple convective parameterization. Such a framework provides a more solid foundation for the construction of simple convective parameterizations and validates the physical intuitions behind the parameter choices.

6.2 Future work

There are many limitations to the current work that will require future studies to tackle. One of the limitations is that the characteristics of the asymmetries are only examined based on a single azimuthal mean hurricane structure. As some previous studies [Montgomery & Lu, 1997, Schecter & Montgomery, 2004, Menelaou et al., 2016] pointed out, the structures and the frequencies of the dominant asymmetries can vary with the background vortex structure, especially for the fast-propagating wave as its inner part is associated with a vortex-Rossby wave that is highly dependent on the background vorticity and its gradient. For future studies, it will be useful to test the sensitivity of the asymmetric signals on the background vortex structure both in the simulations and in the simple eigenfrequency model.

Second, the setup of the WRF simulation is not realistic enough to include environmental forcings such as vertical wind shear or the beta-effect, and those external forcings may play a role in the convective and kinematic asymmetries. Therefore, the dominant asymmetries found in this study might not necessarily apply to more realistic simulations. Future work could focus on either more realistic simulations or real-world TCs.

Third, the eigenfrequency model assumes the background vortex to be barotropic, but the background vortex of a hurricane usually weakens with height. So the effect of the sheared background vortex will be another potential future direction to be explored. Another limitation is that the model does not take the background secondary circulation into account. However, the momentum and energy transport by the secondary circulation may be critical in regions such as the boundary

layer or the eyewall.

Lastly, we only constructed linear response functions around four reference states along the radius. However, to more accurately map out the parameters, it requires the construction of linear response functions around more reference states where the parameters change rapidly, e.g., from right outside the eyewall to the subsidence region. More importantly, it is useful to generalize the parameter estimates through scaling or other methods so that we do not have to construct a new set of linear response functions every time we want to study a new hurricane.

A

Discretized Eigenvalue Problem

With given zonal wave number n and baroclinic mode j, Eqs.?? can be solved numerically as an eigen-frequency problem. The N grids are evenly distributed on the domain $[0, r_b]$, and u, v are defined at the center of each grid, while p is defined at the boundary of each grid. Therefore, Eqs.?? can be

written in the discretized form,

$$-i\omega\tilde{u}_{i+\frac{1}{2}} = -in\overline{\Omega}_{i+\frac{1}{2}}\tilde{u}_{i+\frac{1}{2}} + \overline{\xi}_{i+\frac{1}{2}}\tilde{v}_{i+\frac{1}{2}} + \frac{\tilde{T}_{i+1} - \tilde{T}_i}{\delta r} \tag{A.1a}$$

$$-i\omega\tilde{v}_{i+\frac{1}{2}} = -\overline{\eta}_{i+\frac{1}{2}}\tilde{u}_{i+\frac{1}{2}} - in\overline{\Omega}_{i+\frac{1}{2}}\tilde{v}_{i+\frac{1}{2}} + i\frac{n}{2r_{i+\frac{1}{2}}}(\tilde{T}_i + \tilde{T}_{i+1}) \tag{A.1b}$$

$$-i\omega\tilde{T}_i = c_j^2\frac{r_{i+\frac{1}{2}}\tilde{u}_{i+\frac{1}{2}} - r_{i-\frac{1}{2}}\tilde{u}_{i-\frac{1}{2}}}{r_i\delta r} + ic_j^2\frac{n}{r_i}\frac{\tilde{v}_{i-\frac{1}{2}} + \tilde{v}_{i+\frac{1}{2}}}{2} - in\overline{\Omega}_i\tilde{T}_i \tag{A.1c}$$

where $i = 1, 2, \ldots, N-1$. The boundary conditions are $\tilde{p}_0 = 0$ and $\tilde{p}_N = 0$.

The discretized form is a standard matrix eigenvalue problem,

$$\omega X = \mathcal{A}X \tag{A.2}$$

where ω is the eigenfrequency; $X = (\tilde{u}_{\frac{1}{2}}, \tilde{v}_{\frac{1}{2}}, \tilde{T}_1, \ldots, \tilde{T}_{N-1}, \tilde{u}_{N-\frac{1}{2}}, \tilde{v}_{N-\frac{1}{2}})^{\mathrm{T}}$ is the eigenvector of the discretized system, and $\mathcal{A}$ is a $(3N-1) \times (3N-1)$ matrix representing the discretized differential

operator, which has the following form,

$$\begin{pmatrix}
-in\overline{\Omega}_{\frac{1}{2}} & \overline{\xi}_{\frac{1}{2}} & -\frac{1}{r} & 0 & 0 & 0 & 0 & 0 & 0 & 0 \\
-\overline{\eta}_{\frac{1}{2}} & -in\overline{\Omega}_{\frac{1}{2}} & i\frac{n}{2r_{\frac{1}{2}}} & 0 & 0 & \ddots & \ddots & \ddots & \ddots & 0 \\
-\frac{c_j^2 r_{\frac{1}{2}}}{r_1\ r} & i\frac{nc_j^2}{2r_1} & -in\overline{\Omega_1} & \frac{c_j^2 r_{\frac{3}{2}}}{r_1\ r} & i\frac{nc_j^2}{2r_1} & 0 & \ddots & \ddots & \ddots & 0 \\
0 & 0 & -\frac{1}{r} & -in\overline{\Omega}_{\frac{3}{2}} & \overline{\xi}_{\frac{3}{2}} & \frac{1}{r} & 0 & \ddots & \ddots & 0 \\
0 & 0 & i\frac{n}{2r_{\frac{3}{2}}} & -\overline{\eta}_{\frac{3}{2}} & -in\overline{\Omega}_{\frac{3}{2}} & i\frac{n}{2r_{\frac{3}{2}}} & 0 & 0 & \ddots & 0 \\
0 & \ddots & 0 & -\frac{c_j^2 r_{\frac{3}{2}}}{r_2\ r} & i\frac{nc_j^2}{2r_2} & -in\overline{\Omega_2} & \frac{c_j^2 r_{\frac{5}{2}}}{r_2\ r} & i\frac{nc_j^2}{2r_2} & 0 & 0 \\
0 & \ddots & \ddots & 0 & \ddots & \ddots & \ddots & \ddots & \ddots & 0 \\
0 & \ddots & \ddots & \ddots & 0 & -\frac{c_j^2 r_{N-\frac{3}{2}}}{r_{N-1}\ r} & i\frac{nc_j^2}{2r_{N-1}} & -in\overline{\Omega}_{N-1} & \frac{c_j^2 r_{N-\frac{1}{2}}}{r_{N-1}\ r} & i\frac{nc_j^2}{2r_{N-1}} \\
0 & \ddots & \ddots & \ddots & \ddots & 0 & 0 & -\frac{1}{r} & -in\overline{\Omega}_{N-\frac{1}{2}} & \overline{\xi}_{N-\frac{1}{2}} \\
0 & 0 & 0 & 0 & 0 & 0 & 0 & i\frac{n}{2r_{N-\frac{1}{2}}} & -\overline{\eta}_{N-\frac{1}{2}} & -in\overline{\Omega}_{N-\frac{1}{2}}
\end{pmatrix} \tag{A.3}$$

Therefore, given the structure of a vortex, eigenvalues and eigenvectors can be derived from matrix $\mathcal{A}$ to infer the radial structures and instabilities of the waves. We will be applying monopolar vortex to validate the numerically solved eigenfrequency problem,

$$v = \frac{2R}{1 + R^2} v_{max} \tag{A.4}$$

where $R = r/r_{max}$.

B

Refinement of linear response functions through SVD decomposition

As we discussed in Section 3.2.2, to increase the accuracy in the linear response functions M, we could apply stronger forcing for the fast decaying modes so that its deviations from the reference state become significant. In this section, we are going to describe the procedure to refine the linear

response functions.

After applying the perturbation forcing layer by layer, we can estimate the linear response matrix M through a matrix inversion as Eq. (3.2). If we define W_s and W_F as the weighing matrix for the state vector $\vec{x}$ and the forcing $\frac{\mathrm{d}\vec{x}}{\mathrm{d}t}$, then we will have

$$\mathrm{W}_s\vec{x} = \mathrm{W}_s\mathrm{M}^{-1}\mathrm{W}_F^{-1}(\mathrm{W}_F\frac{\mathrm{d}\vec{x}}{\mathrm{d}t}) \tag{B.1}$$

The weighing matrix we use mainly represents the mass of each layer, so the norm of $\mathrm{W}_s\vec{x}$ or $\mathrm{W}_F\frac{\mathrm{d}\vec{x}}{\mathrm{d}t}$ is a mass-weighted measure. We then perform SVD decomposition on the matrix $\mathrm{W}_s\mathrm{M}^{-1}\mathrm{W}_F^{-1} = \mathrm{USV}^*$, and we will have

$$\mathrm{W}_s\vec{x} = \mathrm{USV}^*(\mathrm{W}_F\frac{\mathrm{d}\vec{x}}{\mathrm{d}t}) \tag{B.2}$$

If we choose the perturbation forcing to be proportional to each $\vec{v_i}$, where $\vec{v_i}$ is the ith column vector of matrix V, the response then becomes

$$\mathrm{W}_s\vec{x} = \mathcal{A}_i s_i \vec{u}_i, \tag{B.3}$$

where $\mathcal{A}_i$ is the amplitude of the forcing, s_i is the ith singular value, and $\vec{u}_i$ is the ith column vector of matrix U.

This indicates that the weighted norm of the response is proportional $\mathcal{A}_i s_i$, while the perturbation forcing is proportional to $\mathcal{A}_i$. Given that the goal here is to have large enough response which has a higher signal to noise ratio, and a small enough perturbation forcing so that the perturbation is

still linear, we choose the amplitude of each forcing to be

$$\mathcal{A}_i = \frac{1}{\sqrt{s_i * s_1}}. \tag{B.4}$$

Once the new set of forcing $\vec{f_i} = \mathcal{A}_i \vec{v}_i$ is designed, we then follow the procedure described in Section 3.2.2 to construct the refined linear response functions. Fig (add reference) is showing the eigenvalues and their inverse of the linear response matrix constructed from layer by layer perturbations, while fig. (add reference) is showing those of the linear response matrix from SVD constructed forcing. The red dots are the eigenvalues and their inverse of the matrix, and the black dots are the eigenvalues and their inverse of the response matrices constructed from a subset period of the simulations by bootstrapping. The spread of the black dots represent the uncertainty of the eigenvalues and their inverse of the linear response matrix, and we can see that the linear response matrix constructed from the SVD forcing has much smaller uncertainties.

C

Analytical solutions of the convectively coupled instability with limiting parameters

In this Appendix, we are going to analyze the linear instability of the convectively coupled system described in Chapter 2, with some simplifications. The limiting case we are going to consider is when $\gamma = 0$, that is the convective mass flux being dominated by entraining parcels and the boundary

layer is in quasi-equilibrium with the second mode temperature. Kuang [2008a] found that this is the limiting scenario where the moist-stratiform instability lies.

In this case, the first mode is essentially decoupled from the system and can be ignored. The system is further simplified by setting $b_2 = 0$ to remove the influence of the second mode heating on the boundary layer moist static energy; ε is set to 0 so there is no damping of temperature; d_2 is set to 0 to remove the effect of second mode heating on the midtropospheric moisture q. We further tighten the quasi-equilibrium assumption to 'strict' quasi-equilibrium by enforcing $L = L_{eq}$.

Assuming $w_1 \sim J_1$, the moisture tendency equation, Eq.(3.7a) can be simplified to

$$(\frac{\partial}{\partial t} + \frac{\overline{v}}{r}\frac{\partial}{\partial \lambda})q = (a_1 - d_1)J_1 \tag{C.1}$$

With strict equilibrium between the boundary layer and the free-troposphere, $b_2 = 0$ and $\gamma = 0$, Eqs (3.13a) and (3.13b) leads to

$$J_1 = -\frac{F}{b_1}(\frac{\partial}{\partial t} + \frac{\overline{v}}{r}\frac{\partial}{\partial \lambda})T_2 \tag{C.2}$$

Therefore, the dynamic equations become

$$(\frac{\partial}{\partial t} + \frac{\overline{v}}{r}\frac{\partial}{\partial \lambda})u_2 - \overline{\xi}v_2 = \frac{\partial T_2}{\partial r} \tag{C.3a}$$

$$(\frac{\partial}{\partial t} + \frac{\overline{v}}{r}\frac{\partial}{\partial \lambda})v_2 + \overline{\eta}u_2 = \frac{1}{r}\frac{\partial T_2}{\partial \lambda} \tag{C.3b}$$

$$(\frac{\partial}{\partial t} + \frac{\overline{v}}{r}\frac{\partial}{\partial \lambda})T_2 - c_2^2(\frac{1}{r}\frac{\partial (ru_2)}{\partial r} + \frac{1}{r}\frac{\partial v_2}{\partial \lambda}) = J_2 = -L_0 r_q q \tag{C.3c}$$

$$(\frac{\partial}{\partial t} + \frac{\overline{v}}{r}\frac{\partial}{\partial \lambda})q = -(a_1 - d_1)\frac{F}{b_1}(\frac{\partial}{\partial t} + \frac{\overline{v}}{r}\frac{\partial}{\partial \lambda})T_2 \tag{C.3d}$$

First, we are going to focus on a vortex with solid body rotation, where $\overline{\Omega}(r) = \Omega_0$. In this case, $\overline{\xi} = \overline{\eta} = f + 2\Omega_0$. Through some manipulations, we will have

$$\begin{aligned}&(\overline{\xi}\overline{\eta} + (\frac{\partial}{\partial t} + \frac{\overline{v}}{r}\frac{\partial}{\partial \lambda})^2)(\frac{\partial}{\partial t} + \frac{\overline{v}}{r}\frac{\partial}{\partial \lambda})T_2 - c_2^2(\frac{\partial}{\partial t} + \frac{\overline{v}}{r}\frac{\partial}{\partial \lambda})(\frac{1}{r}\frac{\partial(r\frac{\partial T_2)}{\partial r}}{\partial r} + \frac{1}{r^2}\frac{\partial^2 T_2}{\partial \lambda^2}) \\ &= (\overline{\xi}\overline{\eta} + (\frac{\partial}{\partial t} + \frac{\overline{v}}{r}\frac{\partial}{\partial \lambda})^2)\mathcal{A}T_2,\end{aligned} \tag{C.4}$$

where $\mathcal{A} = L_0 r_q (a_1 - d_1)\frac{F}{b_1}$. Substituting the normal mode solution $T_2 = \tilde{T}_{n,2}(r)(\exp(i(n\lambda - \omega t)) + c.c)$, we obtain

$$\frac{\partial^2 \tilde{T}_{n,2}}{\partial r^2} + \frac{1}{r}\frac{\partial \tilde{T}_{n,2}}{\partial r} + ((\frac{\mathcal{A}(\overline{\xi}\overline{\eta} - \sigma^2)}{c_2^2(-i\sigma)} - \frac{\overline{\xi}\overline{\eta} - \sigma^2}{c_2^2}) - \frac{n^2}{r^2})\tilde{T}_{n,2} = 0, \tag{C.5}$$

where $\sigma = \omega - n\frac{\overline{v}}{r}$. This yields solutions of the normal modes of temperature,

$$T(r) = J_n(mr) \tag{C.6}$$

and the dispersion relationship

$$m^2 = \frac{\mathcal{A}(\overline{\xi}\overline{\eta} - \sigma^2)}{c_2^2(-i\sigma)} - \frac{\overline{\xi}\overline{\eta} - \sigma^2}{c_2^2}, \tag{C.7}$$

where m can be considered as a combination of radial and azimuthal wavenumber $m^2 \sim k_r^2 + n^2/r^2$. The dispersion relationship can be further derived into a 3-rd order polynomial equation in terms of

σ,

$$\sigma^3 - iA\sigma^2 - (\bar{\xi}\bar{\eta} + c_2^2 m^2)\sigma + i\bar{\xi}\bar{\eta}A = 0 \tag{C.8}$$

Given the scales of parameters we are interested in, the equation has the three following roots in approximation ,

$$\sigma_1 = i\frac{\bar{\xi}\bar{\eta}}{\bar{\xi}\bar{\eta} + c_2^2 m^2}A \tag{C.9a}$$

$$\sigma_{2,3} = \pm\sqrt{\bar{\xi}\bar{\eta} + c_2^2 m^2} + i\frac{c_2^2 m^2}{2(\bar{\xi}\bar{\eta} + c_2^2 m^2)}A \tag{C.9b}$$

The solution has three unstable modes, one stationary relative to the background rotation rate, and two two gravity waves propagating at a rotation rate of $\pm\sqrt{\bar{\xi}\bar{\eta} + c_2^2 m^2}$. At low wavenumber limit, $c_2^2 m^2 >> \bar{\xi}\bar{\eta}$, the instability of the stationary wave dominates, while at high wavenumber limit, the two gravity waves have stronger instabilities. The growth rate is proportional to $A = L_0 r_q(a_1 - d_1)\frac{F}{b_1}$, indicating that the larger the L_0, r_q and F are, the larger the growth rate, and the larger b_1 is, the smaller the growth rate is.

For more general vortex structure, if the wavelength of the perturbation is much smaller than the length scale of the changing background vortex, we could use the local vortex properties as an approximation. The solutions to the system are essentially similar to the solutions above, except that the stationary wave now has a retro retro-propagating speed of $\frac{n}{r}\beta_0/(\xi_0\eta_0/c_2^2 + m^2)$, which is consistent with the propagating speed of a vortex Rossby wave.

References

Abarca, S. F. & Montgomery, M. T. (2013). Essential dynamics of secondary eyewall formation. *Journal of the Atmospheric Sciences*, 70(10), 3216–3230.

Abdullah, A. J. (1966). The spiral bands of a hurricane: A possible dynamic explanation. *Journal of the Atmospheric Sciences*, 23(4), 367–375.

Andersen, J. A. & Kuang, Z. (2008). A Toy Model of the Instability in the Equatorially Trapped Convectively Coupled Waves on the Equatorial Beta Plane. *Journal of the Atmospheric Sciences*, 65, 3736–3757.

Barnes, G., Zipser, E., Jorgensen, D., & Marks Jr, F. (1983). Mesoscale and convective structure of a hurricane rainband. *Journal of the Atmospheric Sciences*, 40(9), 2125–2137.

Bender, M. A., Ross, R. J., Tuleya, R. E., & Kurihara, Y. (1993). Improvements in tropical cyclone track and intensity forecasts using the gfdl initialization system. *Monthly Weather Review*, 121(7), 2046–2061.

Bogner, P. B., Barnes, G. M., & Franklin, J. L. (2000). Conditional instability and shear for six hurricanes over the atlantic ocean. *Weather and forecasting*, 15(2), 192–207.

Charnock, H. (1955). Wind stress on a water surface. *Quarterly Journal of the Royal Meteorological Society*, 81(350), 639–640.

Chen, Y. & Yau, M. K. (2001). Spiral bands in a simulated hurricane. Part I: Vortex Rossby wave verification. *Journal of the Atmospheric Sciences*, 58(15), 2128–2145.

Chow, K. C., Chan, K. L., & Lau, A. K. H. (2002). Generation of moving spiral bands in tropical cyclones. *Journal of the Atmospheric Sciences*, 59(20), 2930–2950.

Corbosiero, K. L., Molinari, J., Aiyyer, A. R., & Black, M. L. (2006). The structure and evolution of Hurricane Elena (1985). Part II: Convective asymmetries and evidence for vortex Rossby waves. *Monthly weather review*, 134(11), 3073–3091.

CRED, EM-DAT, & UNISDR (2018). Economic losses, poverty and disasters 1998-2017.

Davis, C., Wang, W., Chen, S. S., Chen, Y., Corbosiero, K., DeMaria, M., Dudhia, J., Holland, G., Klemp, J., Michalakes, J., et al. (2008). Prediction of landfalling hurricanes with the advanced hurricane WRF model. *Monthly weather review*, 136(6), 1990–2005.

DeMaria, M., Knaff, J., & Sampson, C. (2007). Evaluation of long-term trends in tropical cyclone intensity forecasts. *Meteorology and Atmospheric Physics*, 97(1-4), 19–28.

DeMaria, M., Sampson, C. R., Knaff, J. A., & Musgrave, K. D. (2014). Is tropical cyclone intensity guidance improving? *Bulletin of the American Meteorological Society*, 95(3), 387–398.

Diercks, J. W. & Anthes, R. A. (1976). A study of spiral bands in a linear model of a cyclonic vortex. *Journal of the atmospheric sciences*, 33(9), 1714–1729.

Donelan, M., Haus, B., Reul, N., Plant, W., Stiassnie, M., Graber, H., Brown, O., & Saltzman, E. (2004). On the limiting aerodynamic roughness of the ocean in very strong winds. *Geophysical Research Letters*, 31(18).

Dudhia, J. (1989). Numerical study of convection observed during the winter monsoon experiment using a mesoscale two-dimensional model. *Journal of the atmospheric sciences*, 46(20), 3077–3107.

Dunion, J. P. & Marron, C. S. (2008). A reexamination of the jordan mean tropical sounding based on awareness of the saharan air layer: Results from 2002. *Journal of Climate*, 21(20), 5242–5253.

Eliassen, A. (1951). Slow thermally or frictionally controlled meridional circulation in a circular vortex. *Astrophysica Norvegica*, 5, 19.

Emanuel, K. (2003). Tropical cyclones. *Annual review of earth and planetary sciences*, 31(1), 75–104.

Emanuel, K. (2005). Increasing destructiveness of tropical cyclones over the past 30 years. *Nature*, 436(7051), 686.

Fjørtoft, R. (1950). *Application of integral theorems in deriving criteria of stability for laminar flows and for the baroclinic circular vortex*. Grøndahl & søns boktr., I kommisjon hos Cammermeyers boghandel.

Ford, R. (1993). *Gravity wave generation by vortical flows in a rotating frame*. PhD thesis, University of Cambridge.

Ford, R. (1994a). The instability of an axisymmetric vortex with monotonic potential vorticity in rotating shallow water. *Journal of Fluid Mechanics*, 280, 303–334.

Ford, R. (1994b). The response of a rotating ellipse of uniform potential vorticity to gravity wave radiation. *Physics of Fluids*, 6(11), 3694–3704.

Guinn, T. A. & Schubert, W. H. (1993). Hurricane spiral bands. *Journal of the atmospheric sciences*, 50(20), 3380–3403.

Hack, J. J. & Schubert, W. H. (1986). Nonlinear response of atmospheric vortices to heating by organized cumulus convection. *Journal of the atmospheric sciences*, 43(15), 1559–1573.

Haertel, P. T. & Kiladis, G. N. (2004). Dynamics of 2-day equatorial waves. *Journal of the Atmospheric Sciences*, 61(22), 2707–2721.

Hence, D. A. & Houze Jr, R. A. (2008). Kinematic structure of convective-scale elements in the rainbands of hurricanes katrina and rita (2005). *Journal of Geophysical Research: Atmospheres*, 113(D15).

Hendricks, E. A. & Schubert, W. H. (2010). Adiabatic rearrangement of hollow pv towers. *Journal of Advances in Modeling Earth Systems*, 2(4).

Hendricks, E. A., Schubert, W. H., Taft, R. K., Wang, H., & Kossin, J. P. (2009). Life cycles of hurricane-like vorticity rings. *Journal of the Atmospheric Sciences*, 66(3), 705–722.

Houze, R. A. (2010). Clouds in Tropical Cyclones. *Monthly Weather Review*, 138(2), 293–344.

Houze, R. A., Chen, S. S., Smull, B. F., Lee, W.-C., & Bell, M. M. (2007). Hurricane intensity and eyewall replacement. *science*, 315(5816), 1235–1239.

Huang, Y.-H., Montgomery, M. T., & Wu, C.-C. (2012). Concentric eyewall formation in typhoon sinlaku (2008). part ii: Axisymmetric dynamical processes. *Journal of the Atmospheric Sciences*, 69(2), 662–674.

Janjić, Z. I. (1996). The surface layer in the ncep eta model, preprints, 11th conference on numerical weather prediction. *Am. Meteorol. Soc., Norfolk, Va*, (pp. 354–355).

Janjić, Z. I. (2001). Nonsingular implementation of the mellor-yamada level 2.5 scheme in the ncep meso model. *NCEP Office Note 437*, (pp.61).

Jordan, C. L. (1958). Mean soundings for the west indies area. *Journal of Meteorology*, 15(1), 91–97.

Kain, J. S. (2004). The kain–fritsch convective parameterization: an update. *Journal of Applied Meteorology*, 43(1), 170–181.

Kepert, J. D. (2013). How does the boundary layer contribute to eyewall replacement cycles in axisymmetric tropical cyclones? *Journal of the Atmospheric Sciences*, 70(9), 2808–2830.

Kepert, J. D. & Nolan, D. S. (2014). Reply to "comments on 'how does the boundary layer contribute to eyewall replacement cycles in axisymmetric tropical cyclones'". *Journal of the Atmospheric Sciences*, 71(12), 4692–4704.

Khairoutdinov, M. F. & Randall, D. A. (2003). Cloud resolving modeling of the arm summer 1997 iop: Model formulation, results, uncertainties, and sensitivities. *Journal of the Atmospheric Sciences*, 60(4), 607–625.

Khouider, B. & Majda, A. J. (2006). A simple multicloud parameterization for convectively coupled tropical waves. part i: Linear analysis. *Journal of the atmospheric sciences*, 63(4), 1308–1323.

Kiladis, G. N., Wheeler, M. C., Haertel, P. T., Straub, K. H., & Roundy, P. E. (2009). Convectively coupled equatorial waves. *Reviews of Geophysics*, 47(2), 1–42.

Knutson, T. R., McBride, J. L., Chan, J., Emanuel, K., Holland, G., Landsea, C., Held, I., Kossin, J. P., Srivastava, A., & Sugi, M. (2010). Tropical cyclones and climate change. *Nature geoscience*, 3(3), 157.

Kossin, J. P., McNoldy, B. D., & Schubert, W. H. (2002). Vortical swirls in hurricane eye clouds. *Monthly Weather Review*, 130(12), 3144–3149.

Kossin, J. P. & Schubert, W. H. (2001). Mesovortices, polygonal flow patterns, and rapid pressure falls in hurricane-like vortices. *Journal of the atmospheric sciences*, 58(15), 2196–2209.

Kossin, J. P. & Schubert, W. H. (2004). Mesovortices in hurricane Isabel. *Bulletin of the American Meteorological Society*, 85(2), 151–153.

Kuang, Z. (2008a). A Moisture-Stratiform Instability for Convectively Coupled Waves. *Journal of the Atmospheric Sciences*, 65(3), 834–854.

Kuang, Z. (2008b). Modeling the interaction between cumulus convection and linear gravity waves using a limited-domain cloud system–resolving model. *Journal of the Atmospheric Sciences*, 65(2), 576–591.

Kuang, Z. (2010). Linear response functions of a cumulus ensemble to temperature and moisture perturbations and implications for the dynamics of convectively coupled waves. *Journal of the Atmospheric Sciences*, 67(4), 941–962.

Kuang, Z. (2012). Weakly forced mock walker cells. *Journal of the Atmospheric Sciences*, 69(9), 2759–2786.

Kuang, Z. (2018). Linear stability of moist convecting atmospheres. part i: From linear response functions to a simple model and applications to convectively coupled waves. *Journal of the Atmospheric Sciences*, 75(9), 2889–2907.

Kuo, H.-C., Chang, C.-P., Yang, Y.-T., & Jiang, H.-J. (2009). Western north pacific typhoons with concentric eyewalls. *Monthly Weather Review*, 137(11), 3758–3770.

Kuo, H.-C., Williams, R., & Chen, J.-H. (1999). A possible mechanism for the eye rotation of Typhoon Herb. *Journal of the atmospheric sciences*, 56(11), 1659–1673.

Kuo, H.-l. (1949). Dynamic instability of two-dimensional nondivergent flow in a barotropic atmosphere. *Journal of Meteorology*, 6(2), 105–122.

Kurihara, Y. (1976). On the development of spiral bands in a tropical cyclone. *Journal of the Atmospheric Sciences*, 33(6), 940–958.

Lahaye, N. & Zeitlin, V. (2016). Understanding instabilities of tropical cyclones and their evolution with a moist convective rotating shallow-water model. *Journal of the Atmospheric Sciences*, 73(2), 505–523.

Lamb, H. (1932). Hydrodynamics, § 156. *Aufl., Cambridge: Univ. Press1879–1932*.

Lighthill, M. J. (1952). On sound generated aerodynamically i. general theory. *Proceedings of the Royal Society of London. Series A. Mathematical and Physical Sciences*, 211(1107), 564–587.

Macdonald, N. J. (1968). The evidence for the existence of rossby-like waves in the hurricane vortex. *Tellus*, 20(1), 138–150.

Mapes, B. E. (2000). Convective inhibition, subgrid-scale triggering energy, and stratiform instability in a toy tropical wave model. *Journal of the Atmospheric Sciences*, 57(10), 1515–1535.

McAdie, C. J. & Lawrence, M. B. (2000). Improvements in tropical cyclone track forecasting in the atlantic basin, 1970–98. *Bulletin of the American Meteorological Society*, 81(5), 989–998.

Menelaou, K., Schecter, D. A., & Yau, M. (2016). On the relative contribution of inertia–gravity wave radiation to asymmetric instabilities in tropical cyclone–like vortices. *Journal of the Atmospheric Sciences*, 73(9), 3345–3370.

Menelaou, K., Yau, M., & Martinez, Y. (2014). Some aspects of the problem of secondary eyewall formation in idealized three-dimensional nonlinear simulations. *Journal of Advances in Modeling Earth Systems*.

Mlawer, E. J., Taubman, S. J., Brown, P. D., Iacono, M. J., & Clough, S. A. (1997). Radiative transfer for inhomogeneous atmospheres: Rrtm, a validated correlated-k model for the longwave. *Journal of Geophysical Research: Atmospheres*, 102(D14), 16663–16682.

Möller, J. D. & Montgomery, M. T. (2000). Tropical cyclone evolution via potential vorticity anomalies in a three-dimensional balance model. *Journal of the atmospheric sciences*, 57(20), 3366–3387.

Montgomery, M. T. & Kallenbach, R. J. (1997). A theory for vortex rossby-waves and its application to spiral bands and intensity changes in hurricanes. *Quarterly Journal of the Royal Meteorological Society*, 123(538), 435–465.

Montgomery, M. T. & Lu, C. (1997). Free waves on barotropic vortices. part i: Eigenmode structure. *Journal of the atmospheric sciences*, 54(14), 1868–1885.

Montgomery, M. T. & Shapiro, L. J. (1995). Generalized Charney–Stern and Fjortoft theorems for rapidly rotating vortices. *Journal of the atmospheric sciences*, 52(10), 1829–1833.

Moon, Y. & Nolan, D. S. (2010). The dynamic response of the hurricane wind field to spiral rainband heating. *Journal of the Atmospheric Sciences*, 67(6), 1779–1805.

Moon, Y. & Nolan, D. S. (2015). Spiral Rainbands in a Numerical Simulation of Hurricane Bill (2009). Part I: Structures and Comparisons to Observations. *Journal of the Atmospheric Sciences*, 72(1), 164–190.

Moore, B. (1981). Principal component analysis in linear systems: Controllability, observability, and model reduction. *IEEE transactions on automatic control*, 26(1), 17–32.

Naylor, J. & Schecter, D. A. (2014). Evaluation of the impact of moist convection on the development of asymmetric inner core instabilities in simulated tropical cyclones. *Journal of Advances in Modeling Earth Systems*, 6(4), 1027–1048.

NOAA, N. C. f. E. I. N. (2019). U.s. billion-dollar weather and climate disasters. https://www.ncdc.noaa.gov/billions/.

Nolan, D. S. & Montgomery, M. T. (2002). Nonhydrostatic, three-dimensional perturbations to balanced, hurricane-like vortices. Part I: Linearized formulation, stability, and evolution. *Journal of the atmospheric sciences*, 59(21), 2989–3020.

Nolan, D. S., Montgomery, M. T., & Grasso, L. D. (2001). The wavenumber-one instability and trochoidal motion of hurricane-like vortices. *Journal of the atmospheric sciences*, 58(21), 3243–3270.

Peduzzi, P., Chatenoux, B., Dao, H., De Bono, A., Herold, C., Kossin, J., Mouton, F., & Nordbeck, O. (2012). Global trends in tropical cyclone risk. *Nature climate change*, 2(4), 289.

Peng, M. S. & Williams, R. (1991). Stability analysis of barotropic vortices. *Geophysical & Astrophysical Fluid Dynamics*, 58(1-4), 263–283.

Powell, M. D. (1990a). Boundary layer structure and dynamics in outer hurricane rainbands. part i: Mesoscale rainfall and kinematic structure. *Monthly Weather Review*, 118(4), 891–917.

Powell, M. D. (1990b). Boundary layer structure and dynamics in outer hurricane rainbands. part ii: Downdraft modification and mixed layer recovery. *Monthly Weather Review*, 118(4), 918–938.

Rayleigh, L. (1880). On the stability, or instability, of certain fluid motions. *Proc. London Math. Soc.*, 9, 57–70.

Reasor, P. D., Montgomery, M. T., Marks Jr, F. D., & Gamache, J. F. (2000). Low-wavenumber structure and evolution of the hurricane inner core observed by airborne dual-Doppler radar. *Monthly Weather Review*, 128(6), 1653–1680.

Rotunno, R. & Emanuel, K. A. (1987). An air–sea interaction theory for tropical cyclones. part ii: Evolutionary study using a nonhydrostatic axisymmetric numerical model. *Journal of the Atmospheric Sciences*, 44(3), 542–561.

Rozoff, C. M., Nolan, D. S., Kossin, J. P., Zhang, F., & Fang, J. (2012). The roles of an expanding wind field and inertial stability in tropical cyclone secondary eyewall formation. *Journal of the Atmospheric Sciences*, 69(9), 2621–2643.

Safonov, M. G. & Chiang, R. (1989). A schur method for balanced-truncation model reduction. *IEEE Transactions on Automatic Control*, 34(7), 729–733.

Schecter, D. A. & Montgomery, M. T. (2004). Damping and pumping of a vortex Rossby wave in a monotonic cyclone: critical layer stirring versus inertia–buoyancy wave emission. *Physics of Fluids*, 16(5), 1334–1348.

Schecter, D. A. & Montgomery, M. T. (2007). Waves in a cloudy vortex. *Journal of the Atmospheric Sciences*, 64(2), 314–337.

Schubert, W. H. & Hack, J. J. (1982). Inertial stability and tropical cyclone development. *Journal of the Atmospheric Sciences*, 39(8), 1687–1697.

Schubert, W. H., Montgomery, M. T., Taft, R. K., Guinn, T. A., Fulton, S. R., Kossin, J. P., & Edwards, J. P. (1999). Polygonal eyewalls, asymmetric eye contraction, and potential vorticity mixing in hurricanes. *Journal of the atmospheric sciences*, 56(9), 1197–1223.

Shapiro, L. J. & Willoughby, H. E. (1982). The response of balanced hurricanes to local sources of heat and momentum. *Journal of the Atmospheric Sciences*, 39(2), 378–394.

Sitkowski, M., Kossin, J. P., & Rozoff, C. M. (2011). Intensity and structure changes during hurricane eyewall replacement cycles. *Monthly Weather Review*, 139(12), 3829–3847.

Smagorinsky, J. (1963). General circulation experiments with the primitive equations: I. the basic experiment. *Monthly weather review*, 91(3), 99–164.

Smith, R. K., Montgomery, M. T., & Van Sang, N. (2009). Tropical cyclone spin-up revisited. *Quarterly Journal of the Royal Meteorological Society*, 135(642), 1321–1335.

Smith, R. K., Montgomery, M. T., & Vogl, S. (2008). A critique of emanuel's hurricane model and potential intensity theory. *Quarterly Journal of the Royal Meteorological Society*, 134(632), 551–561.

Thompson, G., Field, P. R., Rasmussen, R. M., & Hall, W. D. (2008). Explicit forecasts of winter precipitation using an improved bulk microphysics scheme. part ii: Implementation of a new snow parameterization. *Monthly Weather Review*, 136(12), 5095–5115.

Thompson, G., Rasmussen, R. M., & Manning, K. (2004). Explicit forecasts of winter precipitation using an improved bulk microphysics scheme. part i: Description and sensitivity analysis. *Monthly Weather Review*, 132(2), 519–542.

Walsh, K. J., McBride, J. L., Klotzbach, P. J., Balachandran, S., Camargo, S. J., Holland, G., Knutson, T. R., Kossin, J. P., Lee, T.-c., Sobel, A., et al. (2016). Tropical cyclones and climate change. *Wiley Interdisciplinary Reviews: Climate Change*, 7(1), 65–89.

Wang, Y. (2001). An explicit simulation of tropical cyclones with a triply nested movable mesh primitive equation model: TCM3. Part I: Model description and control experiment. *Monthly weather review*, 129(6), 1370–1394.

Wang, Y. (2002). Vortex Rossby waves in a numerically simulated tropical cyclone. Part I: Overall structure, potential vorticity, and kinetic energy budgets. *Journal of the atmospheric sciences*, 59(7), 1213–1238.

Wang, Y. (2009). How do outer spiral rainbands affect tropical cyclone structure and intensity? *Journal of the Atmospheric Sciences*, 66(5), 1250–1273.

Wang, Y. & Wu, C.-C. (2004). Current understanding of tropical cyclone structure and intensity changes–a review. *Meteorology and Atmospheric Physics*, 87(4), 257–278.

Weber, H. C. & Smith, R. K. (1993). The stability of barotropic vortices: Implications for tropical cyclone motion. *Geophysical & Astrophysical Fluid Dynamics*, 70(1-4), 1–30.

Webster, P. J., Holland, G. J., Curry, J. A., & Chang, H.-R. (2005). Changes in tropical cyclone number, duration, and intensity in a warming environment. *Science*, 309(5742), 1844–1846.

Webster, P. J. & Lukas, R. (1992). Toga coare: The coupled ocean–atmosphere response experiment. *Bulletin of the American Meteorological Society*, 73(9), 1377–1416.

Willoughby, H. (1978). A possible mechanism for the formation of hurricane rainbands. *Journal of the Atmospheric Sciences*, 35(5), 838–848.

Willoughby, H., Clos, J., & Shoreibah, M. (1982). Concentric eye walls, secondary wind maxima, and the evolution of the hurricane vortex. *Journal of the Atmospheric Sciences*, 39(2), 395–411.

Willoughby, H. E., Marks Jr, F. D., & Feinberg, R. J. (1984). Stationary and moving convective bands in hurricanes. *Journal of the atmospheric sciences*, 41(22), 3189–3211.

Wood, V. T. & White, L. W. (2011). A new parametric model of vortex tangential-wind profiles: Development, testing, and verification. *Journal of the Atmospheric Sciences*, 68(5), 990–1006.

Zhong, W. & Zhang, D.-L. (2014). An eigenfrequency analysis of mixed rossby–gravity waves on barotropic vortices. *Journal of the Atmospheric Sciences*, 71(6), 2186–2203.

Zhong, W., Zhang, D.-L., & Lu, H.-C. (2009). A theory for mixed vortex rossby–gravity waves in tropical cyclones. *Journal of the Atmospheric Sciences*, 66(11), 3366–3381.

Zhu, Z. & Zhu, P. (2014). The role of outer rainband convection in governing the eyewall replacement cycle in numerical simulations of tropical cyclones. *Journal of Geophysical Research: Atmospheres*, 119(13), 8049–8072.